7. J. Kastelic, A. Galeski, and E. Baer, "The Multicomposite Structure of Tendon," Connective Tissue Research, 6 (1978) p. 11.

8. C. S. Smith, "A History of Metallography," The University of Chicago Press, Chicago, IL (1960) Chapter IV on "The Work of Henry Clifton Sorby," p. 169.

9. W. Klement, R. H. Willens, and P. E. Duwez, "Non-crystalline Structure in Solidified Gold-Silicon Alloys," Nature, 187 (1960) p. 869.

10. F. E. Luborsky, Proc. NATO Conf. on Glasses -- Current Issues, A. F. Wright and J. Dupuy, Eds., Martinus Nijhoff, The Hague (1985) p. 139.

11. A. Kasak, G. Steven, and T. A. Neumeyer, "High-Speed Tool Steels by Particle Metallurgy," Soc. of Automotive Engrs., SAE Paper No. 720182 (1972) p. 1.

12. P. R. Holiday, A. R. Cox, and R. J. Patterson, "Rapid Solidification Effects on Alloy Structures," Proc. First Intl. Conf. on Rapid Solidification Processing: Principles and Technologies, R. Mehrabian, B. H. Kear, and M. Cohen, Eds., Claitor's Publishing Division, Baton Rouge, LA (1977) p. 246.

13. C. M. Adam and R. E. Lewis, "High Performance Aluminum Alloys," Rapidly Solidified Crystalline Alloys, S. K. Das, B. H. Kear, and C. M. Adams, Eds., The Metallurgical Society of AIME, Warrendale, PA (1985) p. 157.

Section I: Strengthening

SECONDARY HARDENING ULTRAHIGH STRENGTH STEELS

G. R. SPEICH
Department of Metallurgical and Materials Engineering
Illinois Institute of Technology
Chicago, IL 60540

ABSTRACT

The metallurgical principles underlying the development of ultrahigh strength steels with good toughness are reviewed. These include the use of high nickel contents and low carbon contents to avoid brittle fracture, additions of carbide forming elements such as Cr and Mo to promote secondary hardening that results in the formation of a fine dispersion of alloy carbide, and, additions of Co to delay the recovery of the dislocation substructure and to produce a finer dispersion of dislocation-nucleated alloy carbide than otherwise possible. Illustrations of the use of these principles in the development of 10 Ni-8Co-2Cr-1Mo (HY-180) steels are given. Recent work on the effect of steel purity on toughness of HY-180 steels is also discussed.

INTRODUCTION

Secondary hardening steels are a class of quenched and tempered steels which contain sufficient amount of carbide-forming elements (Cr,W,Mo,V) so that upon tempering in the temperature range of 500-600C the coarse cementite particle dispersion is replaced by a fine dispersion of the more stable alloy carbide (Cr_7C_3,W_2C,Mo_2C,VC_x). The replacement of the coarse carbide dispersion with the fine alloy carbide dispersion results in a hardening effect in this tempering range, in contrast to the normal softening effect, leading to the term "secondary hardening." In the classical description of tempering, secondary

hardening corresponds to the fourth stage of tempering [1-3].

Secondary hardening steels have a number of important commercial applications especially in the area of tool steels where the thermal stability of the fine alloy carbide dispersion results in high hardnesses at elevated temperatures, so-called "red-hardness" [4]. Another important application of these steels is their use in high-strength structural applications because their exceptionally fine carbide dispersions lead to good toughness at high strength levels. Thus, many of the newer high-strength high-toughness steels such as HY180 and AF1410 are based on a secondary hardening steel matrix [5,6]. The chemical composition of HY180 [5] and AF1410 [6] are given in Table 1.

Table I

Chemical composition of HY-180 and AF1410

	C	Mn	P	S	Si
HY-180	0.11	0.18	0.001	0.004	0.065
AF1410	0.16	0.001	0.004	0.001	0.010

	Ni	Cr	Mo	Co
HY-180	10.2	2.00	1.0	8.0
AF1410	10.0	2.00	1.00	14.0

In addition to the strong carbide forming elements, such steels may also contain large amounts of nickel and cobalt because of their effect on matrix toughness or the tempering behavior [5].

In the present paper, the various aspects of the fourth stage of tempering will be reviewed, with particular emphasis on the tempering behavior of the newer high-strength high-toughness steels with a low-carbon high-nickel base and how other alloying elements affect the tempering reactions, strength, and toughness.

CARBIDE REACTIONS

Stability of Cementite

The relative stability of the various carbides compared to cementite can be quickly seen by a

comparison of the heat of formation of the various carbides, as shown in Fig. 1. In fact, based on the heat of formation, cementite is one of the weakest carbides.

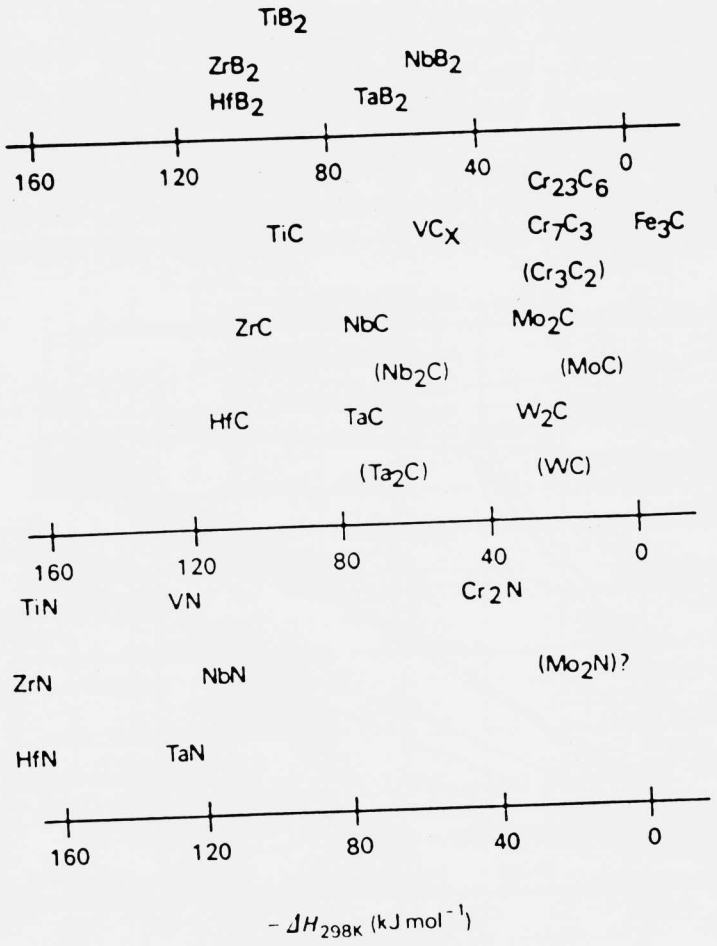

FIGURE 1. Enthalpy of Formation of Carbides, Nitrides, and Borides [7].

Of course, the replacement of Fe_3C by one of the alloy carbides in a simple Fe-C-X ternary system is

dependent on carbon and alloy content and can be represented by a ternary phase diagram. Information on many of these systems is available where X is Cr,W,Mo, or V. A typical example is the isothermal section at 700C of the Fe-Mo-C system shown in Figure 2 [8]. Cementite is stable until additions of molybdenum exceed 10.0 wt pct if the carbon content is 0.5 wt pct. At higher molybdenum contents, Mo_2C becomes the stable carbide phase. If the steel contains 0.2 C, then only 2.0 Mo is necessary to make the Mo_2C carbide phase more stable than the Fe_3C carbide at 700C. All chemical compositions are reported in weight percent and the weight percent designation will be dropped e.g. Fe-0.1 wt pct C-2 wt pct Mo becomes Fe-0.1C-2 Mo in this paper.

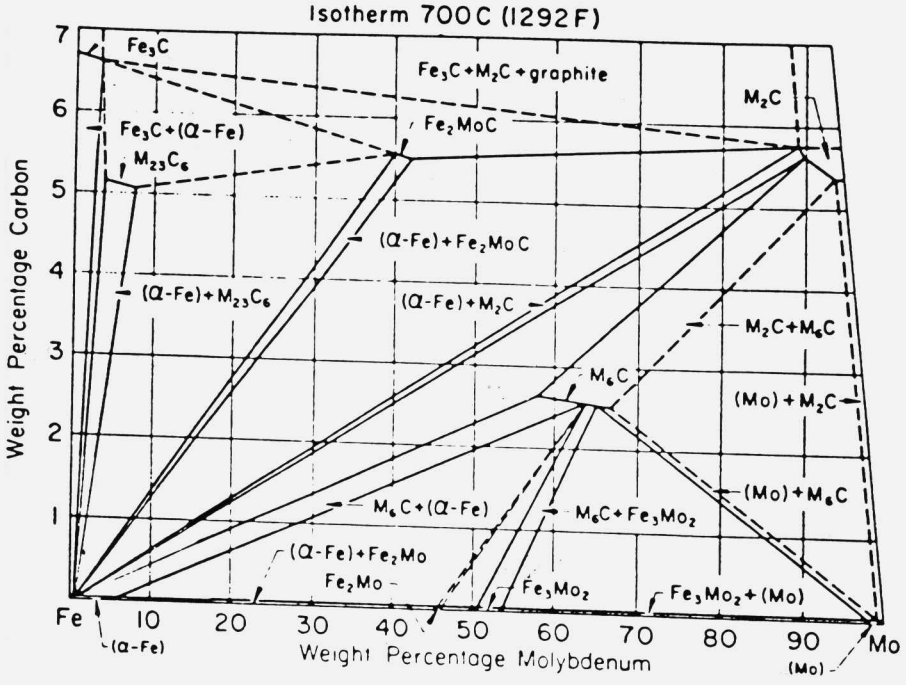

FIGURE 2. Isothermal Section of Fe-Mo-C Ternary Phase Diagram at 700C [8].

Hillert [9] and Uhrenius [10] have shown that by use of the pre-existing thermodynamic data bases and making reasonable assumptions about the variation of activity with chemical composition, it is possible to

make phase equilibria calculations on many Fe-C-X systems. These methods generally require computer techniques. Olson [11] has extended these types of calculations to secondary hardening steels in which more than one alloying element is present, as discussed in this conference.

Nucleation and Growth

Once the alloy content of the steel and the tempering temperature satisfy the thermodynamic condition that the alloy carbide is more stable than the cementite, the cementite particles will begin to dissolve and the alloy carbides will precipitate.

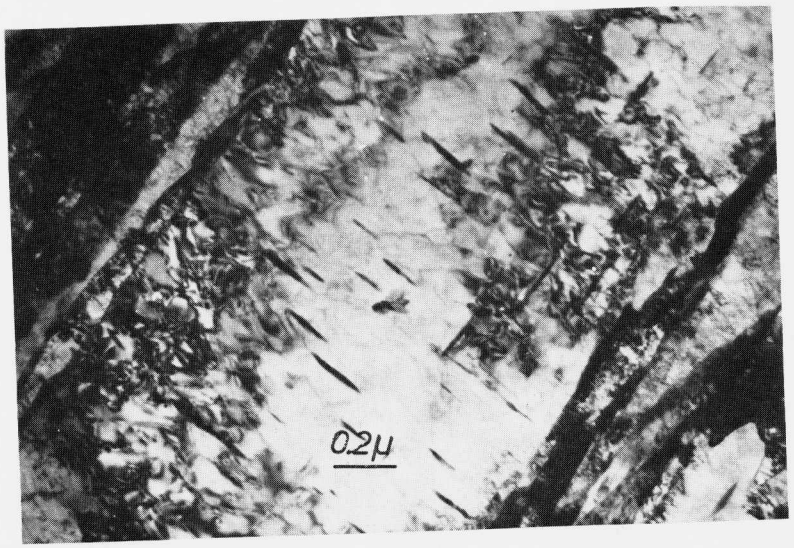

Note one dominant variant

FIGURE 3. Cementite Morphology in Fe-6W-0.2C Steel, After Tempering 1 Hr at 550C Just Prior to Beginning of Alloy Carbide Formation [12].

Figure 3 shows the morphology of the cementite phase just prior to formation of alloy carbide in Fe-6W-0.2C after tempering 1h at 550C [12].The dissolution of the cementite phase is generally considered to proceed by diffusion of carbon. The precipitation of the alloy carbide phase requires diffusion of both the substitutional alloying element as well as carbon. As the substitutional elements are the more slowly

diffusing species it is generally assumed that the growth of the alloy carbide is controlled by the diffusion of the substitutional element rather than by the fast interstitial diffusion of the carbon. The occurrence of secondary hardening at 500-600C coincides with that temperature where the mean diffusion distance of the slow diffusing substitutional elements reaches a value of 20-50 Å which is the size of the first detectable alloy carbide.

In general, the alloy carbides nucleate heterogeneously, either at cementite/ferrite interfaces or at grain boundaries, or at dislocation sites. In the latter case, one of the most important methods to control nucleation density of the alloy carbides is by controlling the dislocation density. A decrease in dislocation density is one of the normal microstructural changes accompanying tempering. This normally occurs by recovery but recrystallization may also occur if the carbide pinning density is very low [13]. To maintain a high dislocation density in the secondary hardening range and thus provide a high density of nucleation sites for the alloy carbide requires additions of large amounts of alloying elements to inhibit recovery processes as discussed in the next section.

Of course, many examples of dislocation nucleated precipitates exist in iron-base alloys for both carbides and nitrides [14]. Substitutional precipitates such as copper and gold [15] and Laves phases Fe_2Ti and Fe_2Nb [16] are also dislocation nucleated. The basic driving force for such precipitation is based on the lowering of the strain energy of the dislocation as described by Cahn [17]. According to Cahn larger the volume difference between the precipitate and the matrix, the greater is the likelihood of dislocation nucleation rather than matrix nucleation. Such considerations also apply to precipitation of alloy carbides. An example of dislocation nucleation of Mo_2C in Fe-4Mo-0.2C after aging 20h at 550C is shown in Fig.4.

FIGURE 4. Dislocation Nucleation of Mo_2C in Fe-4Mo-0.2C Steel After Tempering 20H at 550C [15].

Although it is generally believed that the growth of the alloy carbide is controlled by diffusion of the substitutional element as discussed earlier, diffusion of the substitutional atoms along dislocation sites rather than through the lattice may also play an important role. Also, once the alloy carbide has nucleated Ostwald ripening of the alloy carbide may occur concomitantly with growth. Because of the small size of the carbides the Ostwald ripening process may occur rapidly. In addition, a change in morphology may occur during growth to achieve a stable equilibrium shape. Growth of W_2C and Ostwald ripening of the carbide after tempering Fe-6W-0.2C and Fe-4W-0.2C 6h at 600C and 15h at 700C, respectively, are shown in Figures 5 and 6.

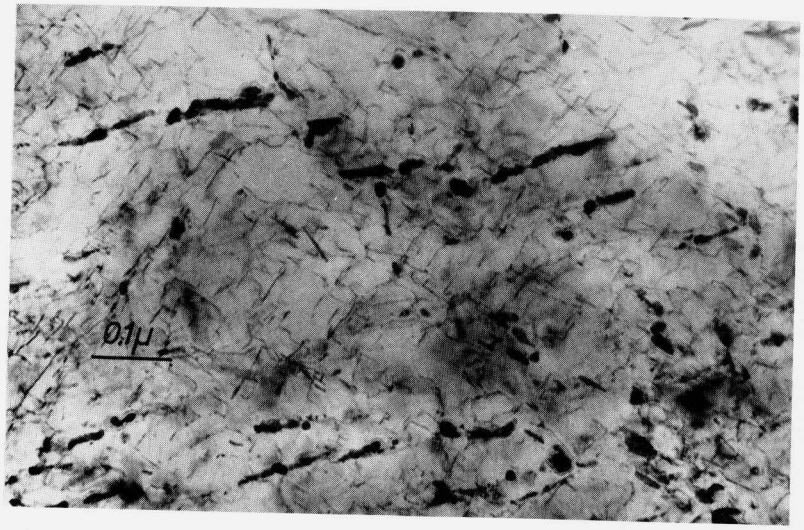

FIGURE 5. Dislocation Nucleation of Alloy Carbide and Early Stages of Growth in Fe-6W-0.2C Steel After Tempering 6H at 600C [12].

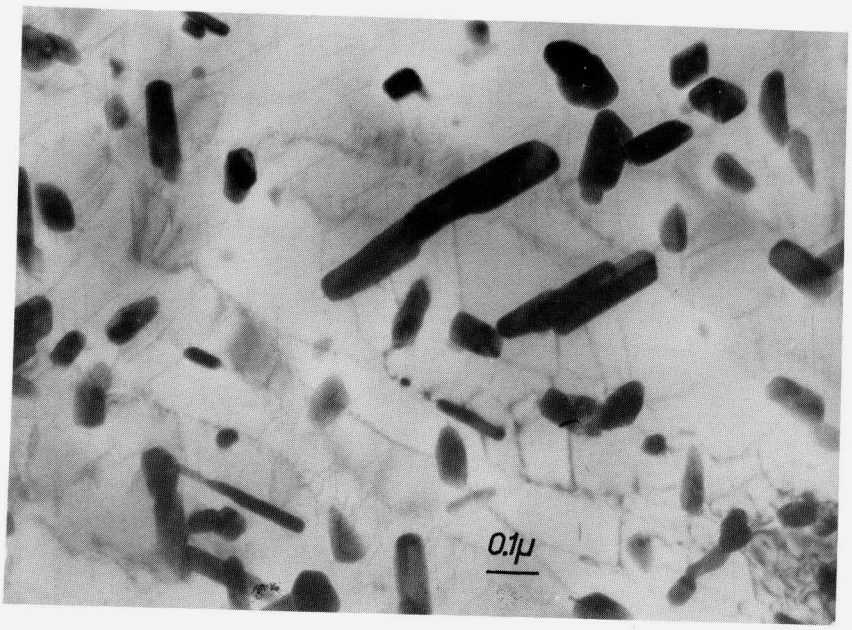

FIGURE 6. Growth and Ostwald Ripening of Alloy Carbide in Fe-4W-0.2C Steel After Tempering 1 H at 700C [12].

RECOVERY OF DISLOCATION SUBSTRUCTURE

Concomitant with the precipitation of cementite and its eventual dissolution as the alloy carbide forms at the secondary hardening temperatures, is the recovery and annihilation of the dislocation substructure of the martensite. The replacement of the course cementite dispersion by the fine alloy carbide dispersion is of course a strengthening reaction whereas the annihalation of the dislocation substructure of the martensite is a softening reaction. The net effect of these two reactions is a secondary hardening peak because of the dominance of the strengthening effect of the alloy carbide dispersion [5].

As discussed in the previous section, since the alloy carbide in many cases may be nucleated at dislocation sites, it is generally advantageous to delay the recovery of the dislocation substructure to increase the nucleation rate of the alloy carbide and thus form a finer dispersion of the alloy carbide.

Normally the recovery of the dislocation substructure during annealing of cold worked metals is controlled by the self-diffusion of iron because dislocation climb is the predominant recovery mechanism, although annihilation of dislocations may also occur by other means such as dislocation glide. Activation energies for recovery processes are generally similar to those for self-diffusion of iron.

Thus, alloying elements such as cobalt which inhibit the recovery process because it results in short or long range ordering [11] that lowers the self diffusion coefficient of iron. The cobalt effect is illustrated in Fig. 7 showing that for simple Fe-10-Ni-0.12 steels increasing cobalt additions result in higher hardnesses because of retention of dislocation substructure to higher temperatures [5]. Direct transmission electron microscope studies of the dislocation substructure also support this argument [5].

Of course other alloying elements may inhibit dislocation recovery because they exert a drag effect on the dislocation because their atomic diameters are

different than iron. Elements like nickel, chromium and molydenum also lead to higher hardnesses after tempering, because these elements may retard the growth of the carbide. It is not clear how to separate their effect on dislocation recovery from their effect on delaying the growth of the carbide phase. Cobalt effects are simpler to interpret since they are not expected to have a strong effect on the growth of the carbide phase.

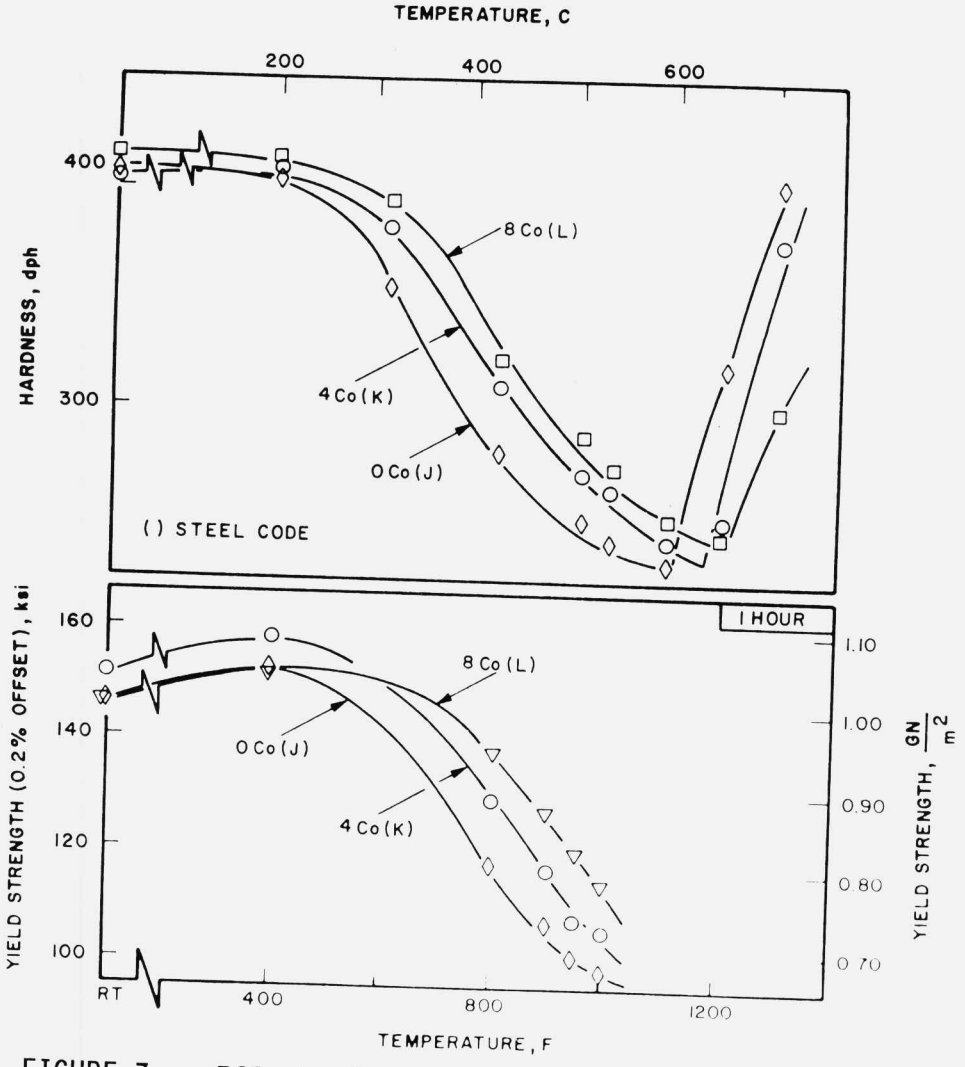

FIGURE 7. Effect of Cobalt Content and Tempering Temperature on the Hardness and Yield Strength of 10-Ni-0.12C Steel [5].

FORMATION OF AUSTENITE

In high nickel alloys containing about 10 percent nickel at temperatures of 500C or higher austenite begins to form [5]. This generally appears as intralath films between the martensite laths. This austenite is enriched in both nickel and carbon and may be stable on cooling to room temperature. When austenite begins to be formed the hardness and yield strength of the alloy decreases sharply. Eventually, at higher temperatures a minimum hardness is achieved and the hardness increases because the austenite begins to transform to fresh martensite upon cooling.

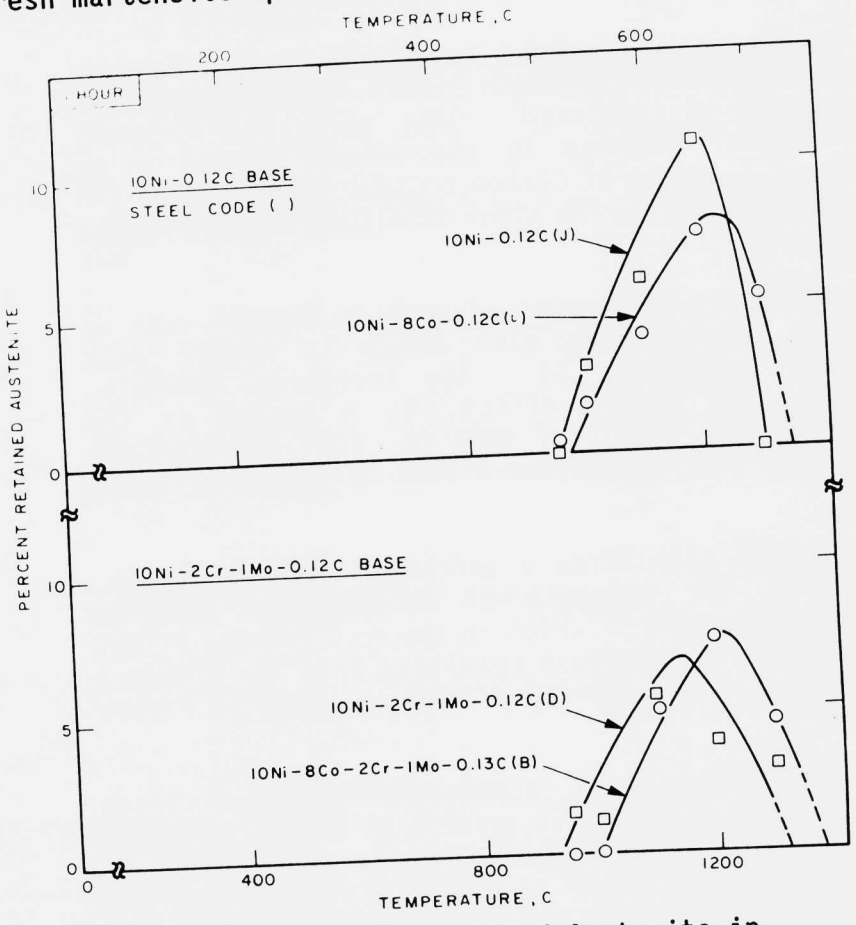

FIGURE 8. Formation of Retained Austenite in 10Ni-0.12C,10Ni-8Co-0.12C,10Ni-2Cr-1Mo-0.12C and 10Ni-8Co-2Cr-1Mo-0.13C Steels at Different Tempering Temperatures [5].

An example of the amount of retained austenite in 10Ni-0.12C and 10Ni-8Co-0.12C alloys is shown in Figure 8. Amounts as high as 10 percent are obtained in 10 Ni steels at 650C. At 650C where stable austenite is formed the hardness of the steel decreases. Above 650C where austenite begins to transform upon cooling because of lower nickel and carbon content, the hardness begins to increase. The formation of austenite overlaps the later stages of Ostwald ripening of the alloy carbide.

ALLOYING ELEMENTS AND STRENGTH

As the carbon content is increased in secondary hardening, ultrahigh strength steels, the peak hardness and strength is increased. This effect is directly related to an increase in the amount of the alloy carbide. The effect of carbon content between 0.09 and 0.19 in a 10Ni-8Co-2Cr-Mo steel is illustrated in Figure 9. [5].

Increasing the amount of carbide formers such as molybdenum or chromium also leads to higher peak hardness or strength [5]. The increased strength, similar to the carbon effect, is a result of the increase in the amount of Mo_2C in 10Ni-1Mo-8Co-1Mo-0.12C steel. The molybdenum effect is shown in Figure 10 [5].

Chromium also forms a secondary hardening peak. However, in the presence of molybdenum, chromium apparently goes into solution in the Mo_2C and its effect is to increase the hardness resulting from the presence of molybdenum in HY-180 and AF1410 as shown in Figure 11 [5].

A common addition to secondary hardening ultrahigh strength steels is cobalt in amounts up to 8%. Although cobalt does not form an alloy carbide it still increases the strength of the steel as shown in Figure 12. The effect is believed to result from an inhibition of the recovery of the dislocation substructure because of the reduced self diffusion rate of iron caused by ordering effects associated with the cobalt as discussed earlier, and the formation of a finer dispersion of the

dislocation-nucleated Mo_2C.

Nickel increases the strength primarily by increasing the hardenability of the steel so that a lath martensite microstructure is formed. The martensite substructure has a strengthening effect because of the increased dislocation density.

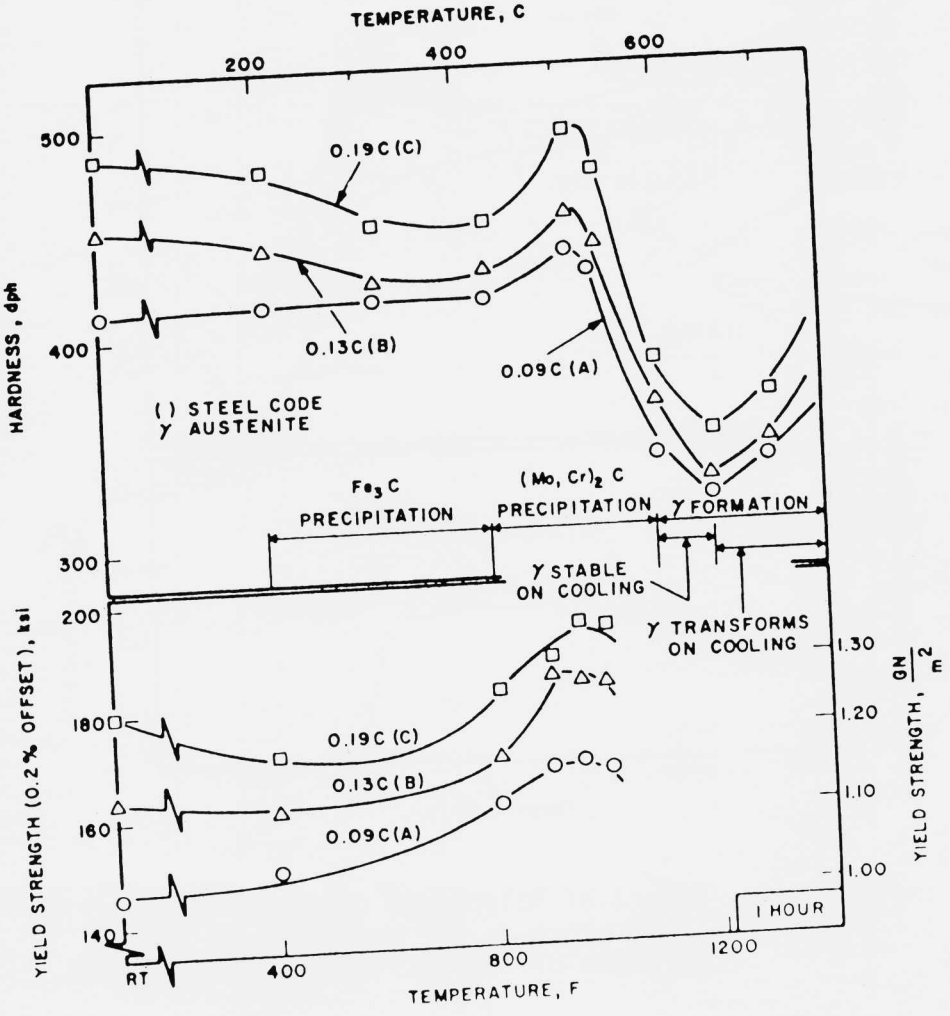

FIGURE 9. Effect of Carbon Content and Tempering Temperature on the Hardness and Yield Strength of 10Ni-2Cr-1Mo-8Co-0.12C Steel [5].

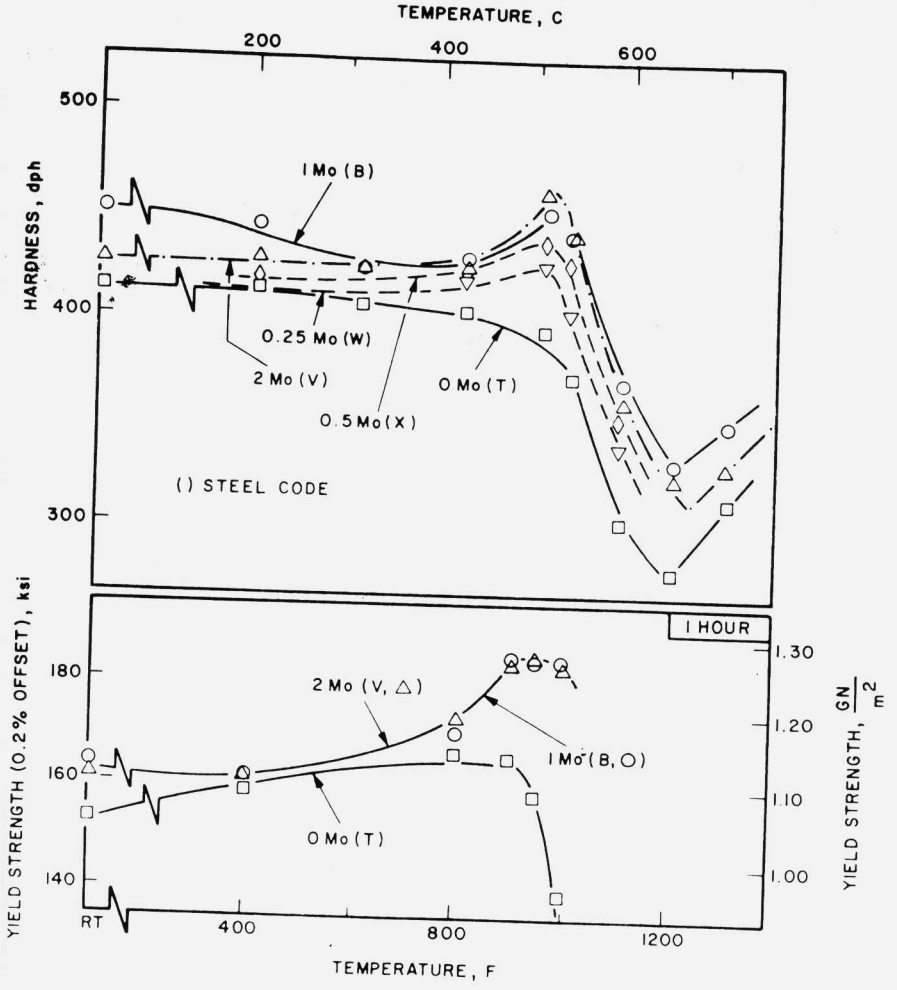

FIGURE 10. Effect of Molybdenum Content and Tempering Temperature on the Hardness and Yield Strength of 10Ni-2Cr-8Co-0.12C Steel [5].

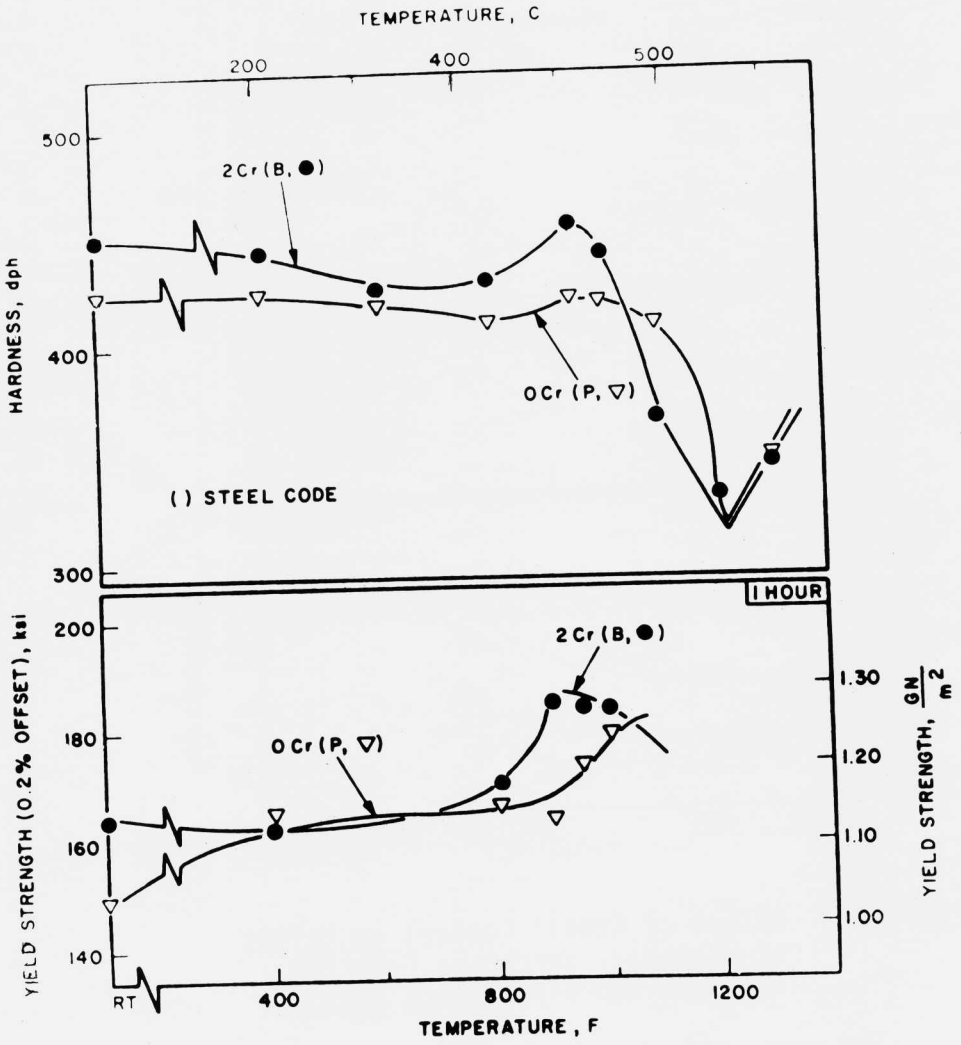

FIGURE 11. Effect of Chromium Content and Tempering Temperature on Hardness and Yield Strength of 10Ni-1Mo-8Co-0.12C Steel [5].

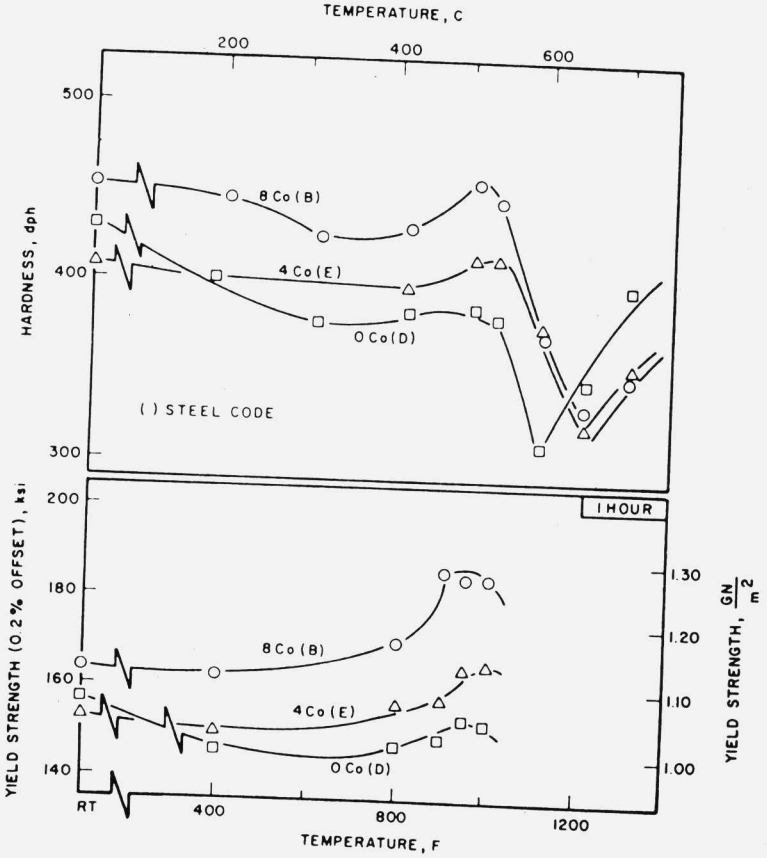

Figure 12. Effect of Cobalt Content on Height of Secondary Hardening Peak in 10Ni-2Cr-1Mo-0.12 Steels [5].

The net effect of sequentially adding these alloying elements is illustrated in Figure 13 for a 10Ni-8Co-2Cr-1Mo-0.12C steel. Each element increases the strength of the steel because of the reasons previously discussed. To achieve the final strength in this steel it can be seen from Figure 13 that all the added alloying elements are required.

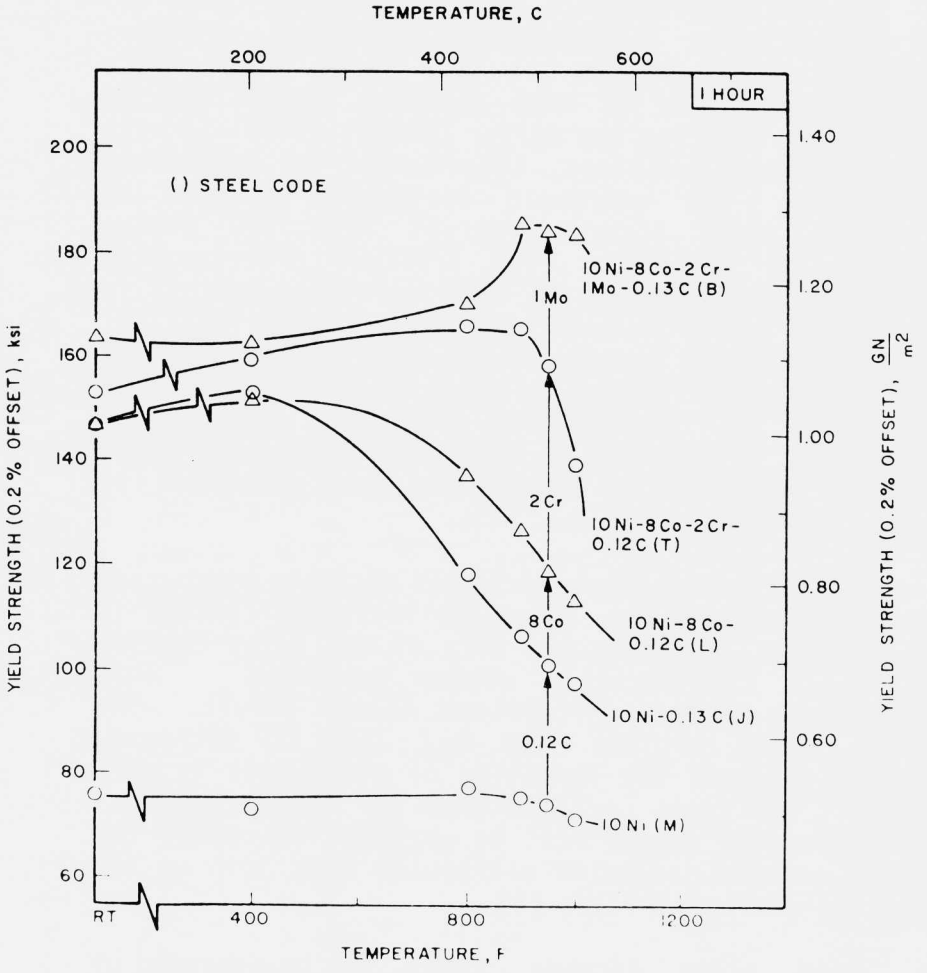

Figure 13. Effect of Individual Alloying Elements on the Yield Strength and Hardness of 10Ni Steel After Tempering at Various Temperatures [5].

TOUGHNESS

As in other ultrahigh strength steels toughness is dependent on strength, decreasing as the strength level is increased. However, for a given strength level the toughness is also dependent on the many factors that affect microvoid coalescence since this is the dominant fracture mechanism.

Microvoid coalescence occurs by decohesion at two sets of particles, inclusions and the alloy carbides. Decohesion first occurs at the large inclusions. Although inclusions in high strength steels can be minimized by lowering the sulfur content (0.001 S) with desulfurization practices, they cannot be completely eliminated. The microvoid coalesence process at inclusions still occurs even at very low volume fractions of sulfides. The fracture process also appears to be dependent on the inclusion spacing in addition to inclusion size at a given volume fraction. When the inclusion spacing of $MnS.Al_2O_3$ is increased at constant volume fraction by changing the size of the inclusions, the toughness is enhanced. Also, when additions of Ti are made to form Ti_2CS inclusions which are more resistent to decohesion, the toughness is further increased [18].

The second set of particles to nucleate microvoids are the alloy carbides. When the inclusion content is kept constant, refining the size of the alloy carbide results in significantly higher toughness. This principle is used in HY-180 and AF1410 steels. The smaller alloy carbides like Mo_2C lead to increased toughness because the formation of microvoids is more difficult for small carbides than for large carbides. Therefore, more energy must be expended to create the smaller carbide nucleated microvoids that join up the inclusion nucleated voids [5].

Fine alloy carbide sizes can be achieved by delaying the recovery of the dislocation substructure with cobalt additions by nucleating the Mo_2C particles on dislocations, as shown in Figure 14 [5]. Generally it is best to create the fine particle size just at the temperature where cementite dissolves. Higher temperatures lead to Ostwald ripening and coarser particles. Control of the tempering time at 480 to 510C can result in greater toughness if the time is chosen to be sure that all the large cementite particles are dissolved. This is clearly illustrated in Figure 15 [5], where a C curve of impact energy is developed at each temperature resulting from the dissolution of the cementite at longer times. By proper choice of the

tempering time to be sure that the cementite is dissolved, the Charpy V-notch energy can be doubled, as shown in Figure 15. This is result of the easier nucleation of microvoids at large cementite particles compared to the smaller Mo_2C particles.

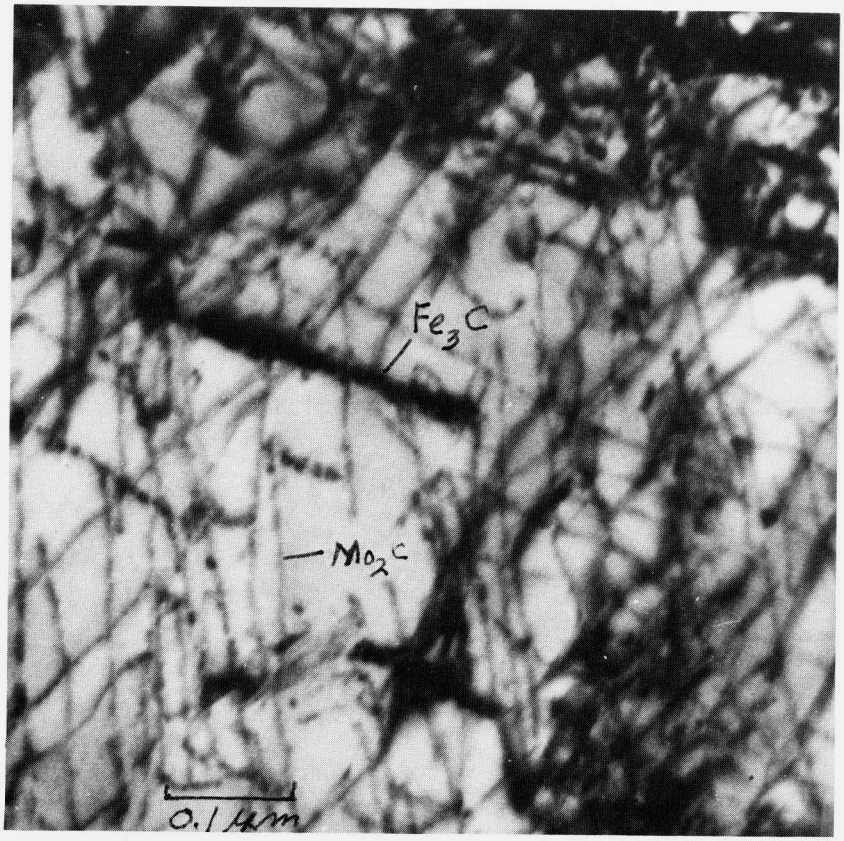

Figure 14. Nucleation of Mo_2C Particles at Dislocations and Dissolution of Cementite in 10Ni-8Co-2Cr-2Cr-0.12C Steel Tempered 30h at 480C [5].

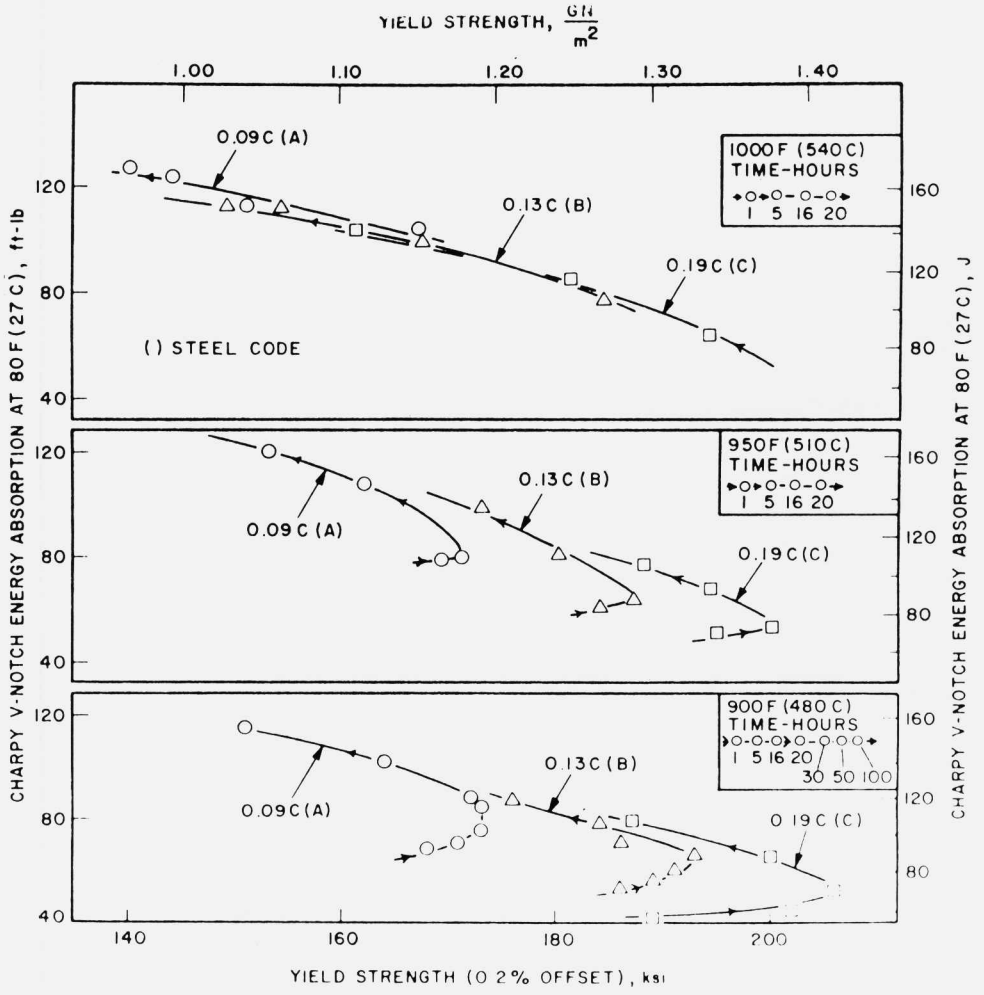

Figure 15. Effect of Time and Tempering Temperature on Charpy V-Notch Energy in 10Ni-2Cr-1Mo-8Co Steels Containing 0.09 to 0.14%C [5].

The addition of 10Ni in HY180 and AF1410 is required to be sure that only microvoid coalesence occurs and no cleavage takes place.

SUMMARY

Secondary hardening of high-nickel low-carbon ultrahigh strength steels HY-180 or AF1410 involves a number of metallurgical reactions. Dissolution of a coarse dispersion of cementite particles and their replacement by a fine dispersion of alloy carbides results in a secondary hardening peak. In the case of HY-180 and AF1410 steels the alloy carbide is Mo_2C and the carbide forming elements are molydenum and chromium. This carbide is nucleated at dislocations followed by growth of the alloy carbide at a rate controlled by diffusion of the substitutional elements. The growth is followed by Ostwald ripening of the alloy carbide.

Recovery of the dislocation substructure occurs concomitantly with the formation of the alloy carbide. Additions of cobalt result in retention of the dislocation substructure to higher temperatures than in steels without cobalt because cobalt lowers the self diffusion rate of iron as a result of ordering. The retention of the dislocation substructure to higher temperatures results in formation of a finer dispersion of the alloy carbide since it is nucleated at dislocation sites.

In high nickel steels, formation of austenite during tempering above 500C may occur as interlath films. At low temperatures large amounts of this austenite is enriched in both nickel and carbon and is stable upon cooling to room temperature. At higher temperatures the nickel and carbon content is lowered and the austenite transforms to fresh martensite. In HY-180 retained austenite contents of 8-10% may be formed.

Fracture of HY-180 and AF1410 occurs by ductile microvoid coalescence. Microvoids form at two sets of particles - large inclusions and fine Mo_2C particles. To control toughness the density of inclusions should be kept as low as possible by lowering the sulfur content. Additives such as Ti are also effective in increasing toughness by replacing $MnS.Al_2O_3$ inclusions

that decohere easily with Ti_2CS inclusions that are more resistant to decohesion. However, for a constant volume fraction of inclusions, the optimum toughness is determined by microvoid coalescence at the Mo_2C particles. Since the formation of microvoids at the Mo_2C particles is more difficult for small particles than for large particles, optimum toughness is obtained by delaying the recovery of the dislocation substructure to increase the nucleation rate of the alloy carbide. Also, for optimum times at the tempering temperatures, higher toughness is obtained when all the cementite has dissolved and only Mo_2C is present. Nickel is added to these steels to prevent brittle fracture and cleavage.

REFERENCES

1. F. B. Pickering, Physical Metallurgy and Design of Steels, Elsevier Science Publishing Co., New York, 1983, pp 133-140.

2. R. K. Honeycombe, Steel: Microstructure and Properties, ASM, 1982, pp 152-165.

3. G. Krauss, "Tempering in Martensite", in Phase Transformations in Ferrous Alloys, Metallurgical Society of AIME, 1984, pp 101-123.

4. G. A. Roberts and R. A. Cary, Tool Steels. ASM, 1980.

5. G. R. Speich, D. S. Dabkowski, and L. F. Porter, "Strength and Toughness of Fe-Ni Alloy Containing C,Co, Mo, and Cr, Metallurgical Transactions, Vol 4, 1973, 303.

6. K. J. Henderman, W. M. Garrison and N. R. Moody, "A Comparison of the Fracture Behavior of Two Heats of the Secondary Hardening Steel AF1410", Metallurgical Transactions, Vol 20A, 1989, p. 105.

7. C. Schick, Thermodynamics of Certain Refractory Compounds, Academic Press, New York, 1966.

8. Metals Handbook, V8, ASM, 1973, p. 409.

9. M. Hillert, "Prediction of Iron-Based Phase Diagrams", In Hardenability Concepts With Applications to Steel, Met Soc AIME, 1978. pp. 5-27.

10. B. Uhrenius, "A Compendium of Ternary Iron-Base Phase Diagrams",ibid, pp. 28-81.

11. G. B. Olson, This conference.

12. A. T. Davenport, private communication 1973, Crucible Steel.

13. G. R. Speich, and W. C. Leslie, "Tempering of Steel", Transactions Met Soc AIME, Vol 224, 1962,pp 850-858.

14. A. S. Keh, W. C. Leslie, and G. R. Speich, Precipitation on Substructure in Iron-Base Alloys, AISI, New York, 1963.

15. E. Hornbogen, "The Role of Strain Energy in the Precipitation of Copper and Gold from Alpha Iron", ACTA Met, vol 10, 1962, p 525.

16. G. R. Speich, "Precipitation of Laves Phases in Iron Fe-Nb and Fe-Ti Alloys", Trans AIME, vol 224, 1962, p 850.

17. J. W. Cahn, "Nucleation on Dislocation", ACTA MET, vol 5, 1956, p. 169.

18. W. Garrison and J. Mahoney, private communication, Carnegie-Mellon University, Pittsburgh, PA, 1989.

ALLOY DESIGN FOR > 3 GPa STEELS

ERHARD HORNBOGEN
Institut für Werkstoffe, Ruhr-Universität Bochum,
D-4630 Bochum, F.R.G.

ABSTRACT

The principles have been reviewed by which ultra high yield stress can be obtained in alloys of iron. Fine scale and coarse microstructures have to be distinguished. In general, both the dislocation theory and a composite approach are required to explain bulk yield strength.

An ultra high yield strength is due to a combination of several elementary hardening mechanisms. The required microstructures may be obtained by suitable thermo-mechanical treatments. The concept of the T-t-t-diagram has been extended to include all types of solid state reactions which occur in thermo-mechanically treated maraging steels (T-t-r-diagram). It is shown which treatments lead to >3 GPa yield strength in two particular maraging steels. Finally, interstitial and substitutional alloys of iron are compared. It is discussed what the perspectives are for future improvements.

INTRODUCTION - ORIGIN OF HARDENING

This paper deals with the ways to analyse and obtain ultra-high strength in iron-base alloys. The term strength is often vaguely defined. Here yield strength is meant and it is implied that it is associated with a considerable amount of plastic deformability and therefore fracture toughness (1,2).

If the origin of the yield strength is to be analysed the structural levels of "phase" and "microstructure" have to be distinguished (1).

Phases are the solid solutions and compounds of iron. The bonds between the atoms determine the values of the elastic constants, crystal symmetry their anisotropy (Table 1). Further on, metastability of a phase and the possibility of stress induced martensitic phase transformation can be of relevance for yield stress and work hardening ability of these materials.

In the level of microstructure the zero- to three-dimensional discontinuities of the phase structure are defined as

TABLE 1

Anisotropy of elastic moduli.

	$\bar{E}$ [GPa]	E_{max} [GPa]	E_{min} [GPa]	|+%| by anisotropy
Al	72	77	64	7
Cu	120	194	68	62
α-Fe	210	290	120	38

TABLE 2

Elementary hardening mechanism of crystalline phases.

No	symbol	obstacles	hardening mechanism
1	σ_o	lattice friction, order	order hardening
2	$\Delta\sigma_s$	solute atoms, vacancies	solid solution hardening
3	$\Delta\sigma_d$	dislocations	work hardening
4	$\Delta\sigma_b$	grain- or phase boundaries	grain boundary hardening
5	$\Delta\sigma_p$	particles	precipitation hardening
6	$\Delta\sigma_{ac}$	crystal anisotropy	texture hardening
7	$\Delta\sigma_{am}$	microstructural anisotropy	fibre hardening
8	$\Delta\sigma_m$	crystal metastability	pre-martensitic softening, transformation hardening

the source of elementary hardening mechanism (Fig. 1, Table 2). The interaction of dislocations with such obstacles forms the base for an understanding of some aspects of the yield stress of alloys. This is especially true for the maraging steels. Nevertheless, the dislocation theory alone is not able to interpret the yield strength of common alloys such as ferrite-pearlite steels, precipitation hardened alloys with particle-free zones at grain boundary, and dual-phase steels (3). In this context it is appropriate to distinguish between "coarse" and "fine" microstructures (Fig. 2). The term "fine microstructure" is used if anomalies like precipitation hardening are found. They must be explained by dislocation theory. Consequently, the scale which defines "fineness" depends on the bulk property (i.e. yield stress) which is of interest. "Coarse" in our context are for example dispersed particles with $S_p < b > 10^3$, where S_p is the particle spacing and b the atomic distance (Fig. 2, right), (Table 3), (4).

For the discussion of the mechanical properties of "coarse microstructures" it is necessary to apply just those aspects of micro-mechanics which have been developed for composite materials (5). It uses methods of continuum mechanics such as finite elements, but also structure and properties of phases and interfaces as micromechanical elements (6). In principle, a three stage process is required to derive the strength of most engineering alloys:

phase structure + fine microstructure + coarse microstructure → bulk property.

For complete understanding each stage requires a subtle knowledge of the previous one.

If hardening $\Delta\sigma$ is based on minimum curvature of dislocations it depends on the phase properties G and b (G shear modulus, b atomic spacing), as well as on the fineness of microstructure (spacing of obstacles S) (Fig. 1):

$$\Delta\sigma \approx \frac{Gb}{S} \qquad (1a)$$

The composite approach for the "coarse" microstructural level requires a knowledge of volume fraction, morphology, and

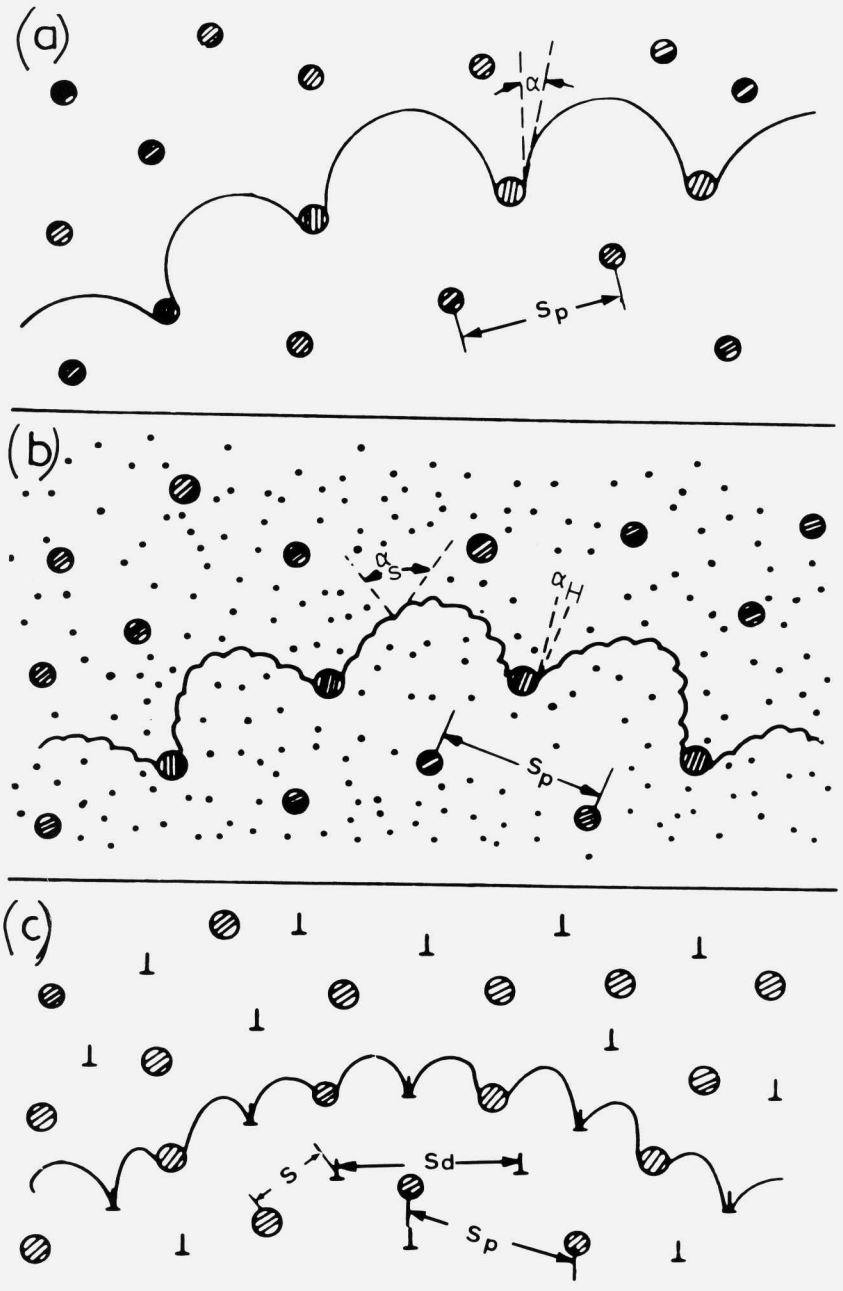

FIGURE 1. Hardening of crystalline phases, schematic.
a)hard particles, enforced semicircular shape of dislocation
b)mixture of soft and hard obstacles, for example solute atoms plus particles
c)mixture of two types of hard obstacles: dislocations and particles obtained by thermo-mechanical treatment

TABLE 3

Critical particle diameters d_c (transition shearing → by-passing) for particles dispersed in α-Fe.

disp. phase	crystal structure	shear modulus [MPa·10³]	APB energy [mJm⁻²]	coherency	critical diameter [nm]
C	diamond	1200	-	-	1
TiC	NaCl	210	-	-	3
Cu	fcc	46	-	-	14
Fe_3Al	bcc	-	100	+	> 100

TABLE 4

Comparison of characteristic volume fractions and critical particle diameters in microalloyed, classical tempered, and maraging steels.

	volume fractions, V_β	critical diameter, d_c
HSLA	10^{-3}	3
Cu, Fe_3C	10^{-2}	15
Marage	10^{-1}	100

properties of the phases, (or "fine" microstructural components such as tempered martensite) the latter have to be obtained by dislocation theory. Then "rule of mixture"-type equations can be obtained which contain just these properties; partial properties p_i, together with volume fractions v_i, and microstructural morphology, M. The bulk property p is obtained:

$$p = f\ (p_i,\ v_i,\ M) \tag{2a}$$

A rather simple example is a uniaxial structure of brittle fibers β in a ductile matrix α. The bulk fracture stress σ_f is limited by that of the fibers $\sigma_{f\beta}$. σ^*_α is the stress in the matrix, as elongation at fracture of the fibers is reached (Fig. 3).

$$\sigma_f = \sigma_{f\beta}\ V_\beta + \sigma^*_\alpha\ V_\alpha \tag{2b}$$

The equation is valid if the strain in matrix and fiber is equal: $\epsilon_\alpha = \epsilon_\beta$. This, in turn, implies perfect bonding of the $\alpha\beta$-interfaces. The structure and properties of interfaces are therefore of great importance for the strength of coarse microstructures.

COMBINATION OF HARDENING MECHANISMS

The yield stress of the present maraging steels is based on the introduction of a variety of obstacles to dislocation motion into the lattice of α-iron. Equation 1 provides an estimate for what spacing is required to reach a yield stress of $\sigma_y \geq 3$ GPa:

$$5\ \text{nm} \approx S \leq Gb\ \sigma_y^{-1} \tag{1b}$$

The result is $S \leq 30$ b, which implies a rather high density of obstacles: solution atoms, dislocation, particles, in a fine polycrystal.

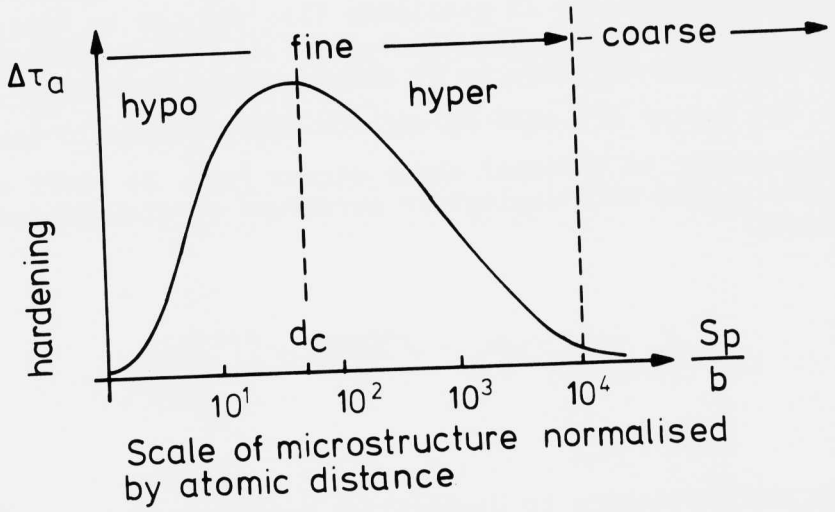

FIGURE 2. Definition of "coarse" and "fine" microstructure, using normalized obstacle spacing.
Hypo- and hyper-fine should be distinguished depending on whether particles are sheared or by-passed below and above a critical particle size (Table 3,4).

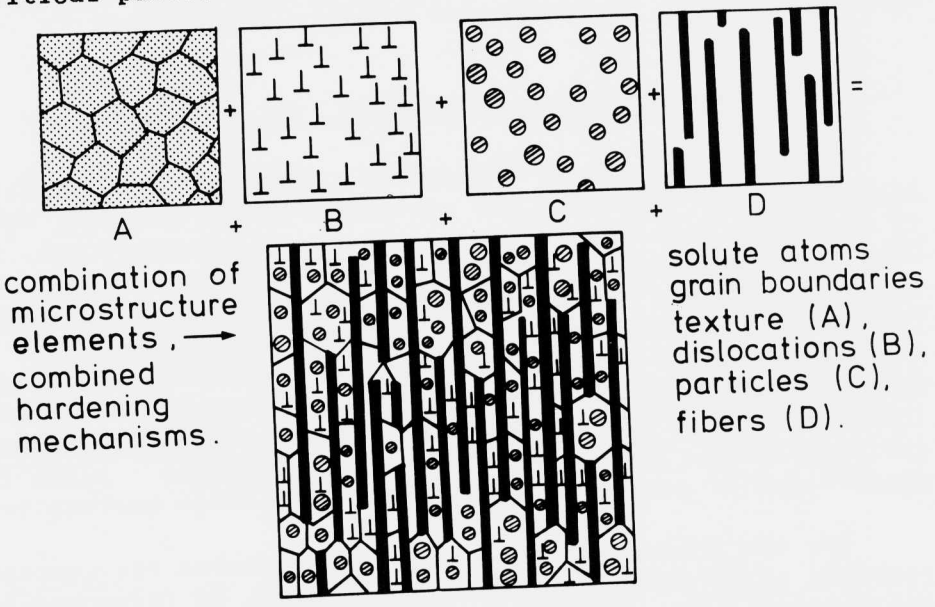

FIGURE 3. Combination of microstructural elements in high strength alloys, schematic.

A simple analytical treatment of such a combination of hardening mechanisms is available (7), and can be applied to the hardening of maraging steel (Fig. 4). The contributions of soft obstacles $\Delta\sigma_S$ have to be distinguished from "hard" ones $\Delta\sigma_H$. The latter are able to enforce dislocations to form semi-circles under an external shear stress (equ. 1). Soft obstacles are passed with negligible curvature of dislocations (Fig. 1 and 2):

$$\sigma_y = \sigma_o + \Delta\sigma_S + \sqrt{\Sigma\Delta\sigma_H^2} + \frac{0<k<k_{max}}{S_b^{1/2}} \qquad (3)$$

σ_o is the resistance to dislocation motion in the pure matrix lattice (α), and the final term considers the effect of grain size (S_b). Its additivity with the other hardening mechanisms is expressed by the values of k. It is controlled by details of dislocation/grain boundary interaction: $0 < k < k_{max}$. For precipitation hardened maraging steel k will approach zero. Nevertheless a fine grain structure is essential in connection with slip localization, grain boundary fracture and consequently for work hardening and fracture toughness.

THERMO-MECHANICAL TREATMENTS, T-t-r-DIAGRMAS

Alloying and thermo-mechanical treatments are the established ways to introduce the obstacles (Table 2 and 3, equ. 3) in a density required for the desired yield stress (equ. 1b). Plastic deformation, martensitic transformation, and precipitation treatments can be used as suitable measures to produce "hard" microstructures. It may be noted that martensitic transformation is not an elementary hardening mechanism, it rather contributes to several of them: dislocations by lattice invarient shear, grain boundaries, and a highly supersaturated solid solution. Tempering treatments can produce ultra-fine dispersions of particles in either austenite or martensite.

For the production of such microstructures the concept of combined solid state reactions can be used. In thermo-mechanically treated maraging steels all types of solid state reactions may take place: re-arrangement of defects (recrystallization), local change in chemical composition (precipitation),

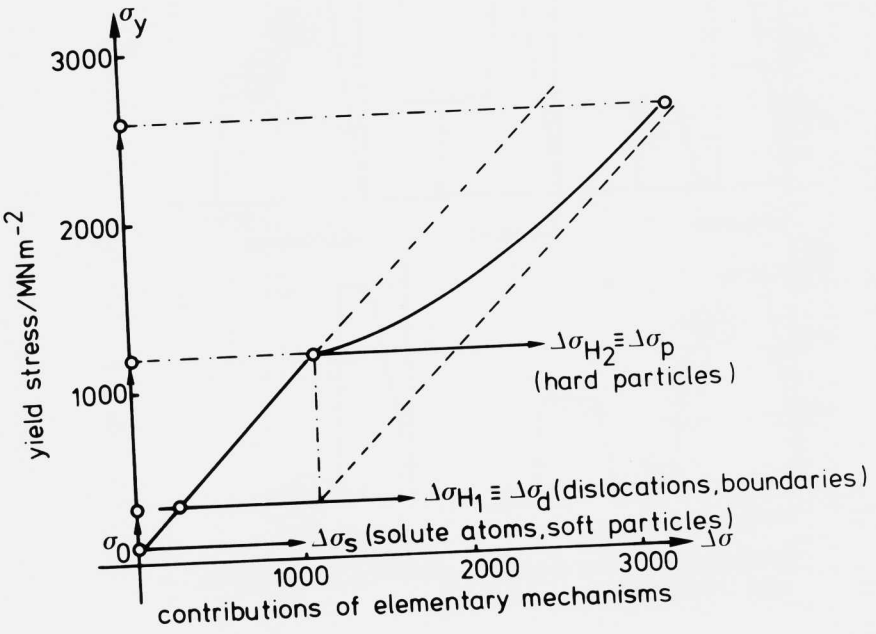

FIGURE 4. Contribution of elementary hardening mechanisms to yield strength of maraging steel.

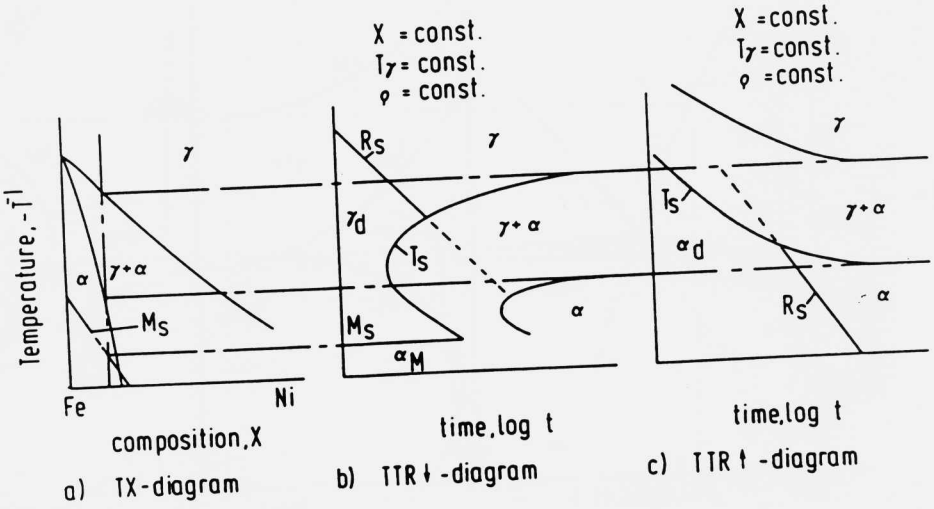

FIGURE 5. Schematic TTR-diagram for hot deformation (austenite) and cold deformation (martensite) of a Fe-5% Ni alloy.

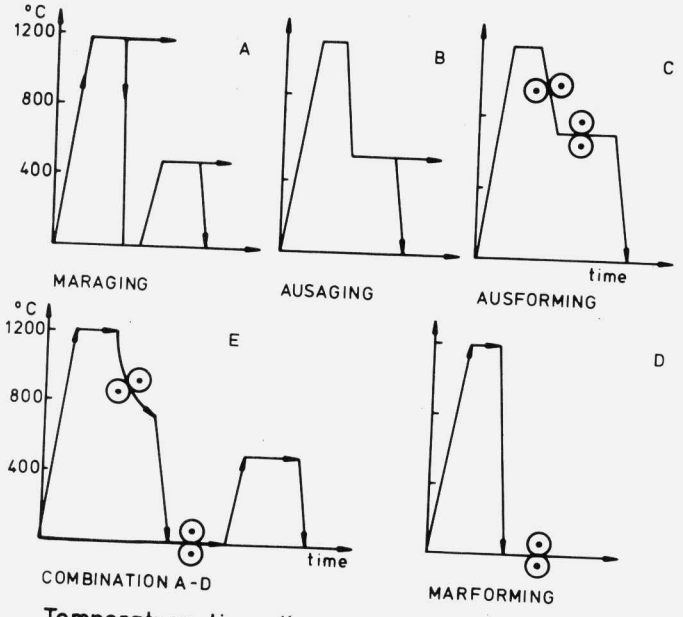

Temperature-time diagrams showing treatments and their combinations (E)

FIGURE 6. Thermo-mechanical treatments by which ultra-high strength (Fig. 8) was obtained.

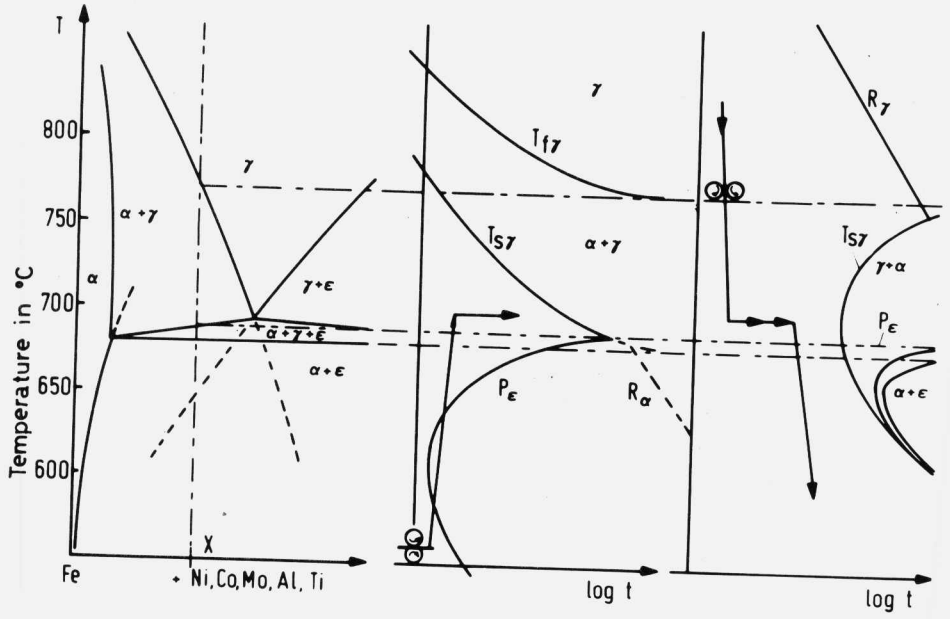

FIGURE 7. Characteristic section of phase diagrams of maragi steels and TTR-diagrams for marforming and ausforming (compa Fig. 5).

change in phase structure (martensitic transformation). These reactions lead to the desired microstructures if they take place in the right sequence and combination. Desired are reactions by which a fine grain size is preserved, thermal rearrangement of dislocations is restricted to reduction of internal stresses (pile-ups), and particles form at and between the dislocations to reduce further the average spacing of the obstacles.

The well-known concept of the time-temperature transformation (Ttt-) diagram has been extended to include recrystallization and transformation reactions (T-t-r-diagram, Fig. 5, 6). Because the situation is somewhat complex for maraging steels a simple Fe-Ni-alloy shall be discussed first (8). There are two types of T-t-r-diagrams depending on whether the high temperature phase γ or martensite α is subjected to plastic deformation, and the alloy is subsequently heated $\uparrow$ or cooled $\downarrow$. Combined reaction must take place in the particular temperature ranges in which a defect and metastable phase exist. A "hard microstructure" originates if recrystallization is inhibited by a fine dispersion of the newly nucleated phase (9)

Fig. 6 summarizes the thermo-mechanical treatments for a maraging steel. The difference (to Fe-Ni, Fig. 5) in phase-diagram and T-t-r-diagram is due to additional alloying elements which provide for precipitation of intermetallic compound from martensite (Fig. 7). There is no principle difference to a quenched and tempered steel which contains interstitial elements and precipitates carbides or nitrides. Only the critical particle sizes may be less as compared to coherent intermetallic compounds (Table 3). The latter precipitate however at a much finer scale and at higher volume fractions (Table 4). Examples for tensile properties which were obtained with a maraging steel by various thermo-mechanical treatments have been summarized in Fig. 8.

PERSPECTIVES

It can be estimated that further sophistication of the discussed thermo-mechanical treatment will probably provide for up to 10 % improvement of yield strength without drastic loss of ductility and toughness. Thus a value of 3.5 GPa seems to represent an upper limit for yield strength of steels. It is essential to introduce particles with a small critical particel size (Table 3) evenly distributed at spacings of less

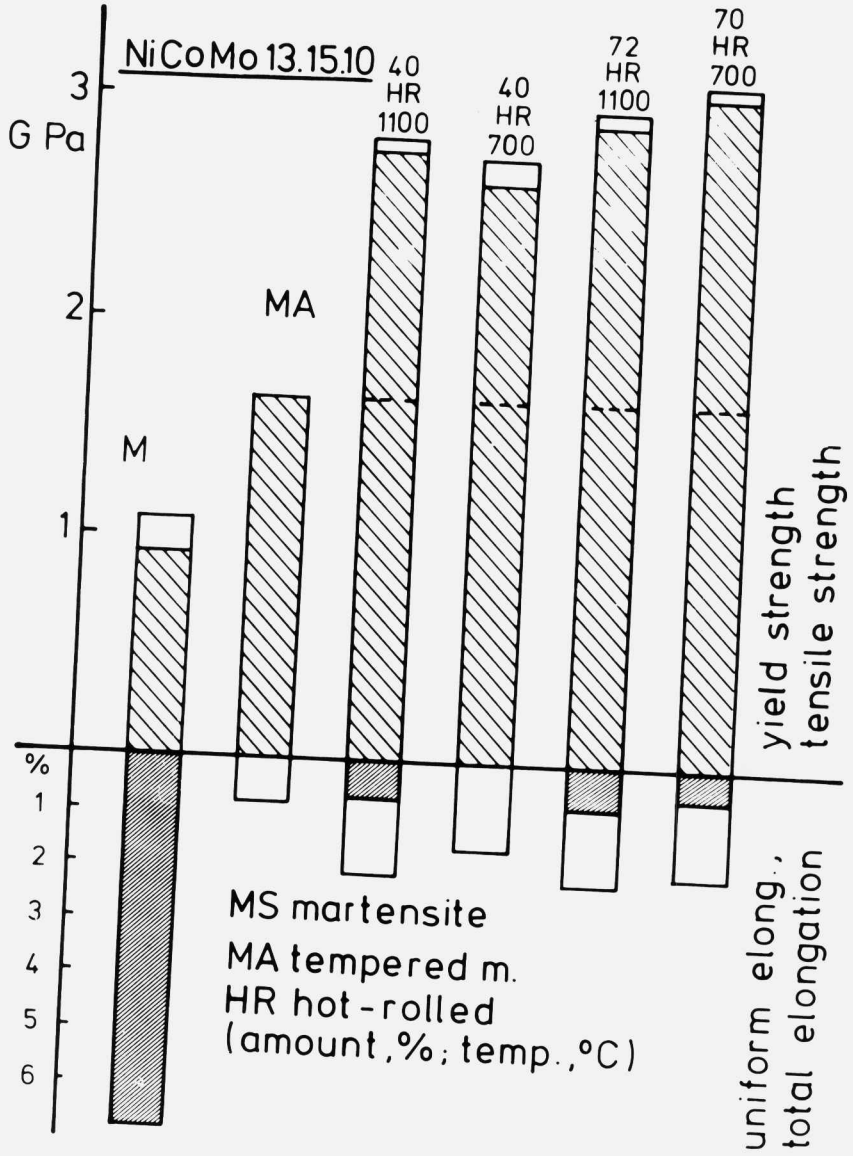

FIGURE 8. Results of tensile tests of a maraging steel after different thermal and thermo-mechanical treatments. In homogeneous martensite, maraging at 480 °C, the number indicates the amount of rolling and the temperatures of austenitization (γ) or intercritical ($\gamma + \alpha$) heat treatments.

than 3 nm (equ. 1). The question arises whether there exist other concepts to overcome these barriers. Two approaches to consider:

A. On the level of phase the strength of bonding and consequently the elastic constants could be raised. This is now well known for Al-Li alloy. For α-iron alloying elements like W, Ta, Nb may have this effect but they favour embrittlement and a higher specific weight if added in larger amounts. An additional effect could be due to utilization of crystal anisotropy. A pronounced $\langle 111 \rangle_\alpha$-texture will provide an improvement which is limited by the range of anisotropy of the elastic moduli (Table 1).
An admixture of metastable austenite to the microstructure by no means has an increasing effect on bulk yield stress. It may however be useful for increasing work hardening ability, resistance to fatigue crack growth and decreasing the tendency for localization of strain in tension.

B. The composite approach seems to show even more promising perspectives. Attempts to develop maraging steels with a duplex or dual phase microstructure (i.e., coarse microstructures) have failed by far to reach high yield strengths. A better way seems to use the fully hardened maraging steel as matrix of a fiber composite (Fig. 3). The production of such a microstructure requires a different procedure. Thermo-mechanical treatments alone are no more sufficient (Fig. 7). Suitable fibers could be Al_2O_3 or even organic materials such as l.c. polymers. For carbon, as well as carbides and nitrides, compatibility problems are expected in the interface with the steel matrix.
Co-extrusion of powders seems to be one way for the production of such composites. A strength limit of about 5 GPa may be estimated for such materials. Simultaneously a low specific weight of the fibers would lower the density of the bulk material.

References

1. A. Kelly, Strong solids, Clarendon, Oxford 1966.

2. K. Friedrich, E. Hornbogen, A. Sandt, Ultra-High Strenght Materials, Fortschr. Ber. VDI-Z. 5, 82, 1984.

3. J. Becker, E. Hornbogen, P. Stratmann, Dual-Phasengefüge, Z. Metallkde. 71 (1980) 27-31.

4. . E. Hornbogen, Fine, coarse and fractal microstructures, Pract. Met. 23 (1986) 258-267.

5. D. Hull, An introduction to composite materials, Cambridge University Press, Cambridge U. K., 1981.

6. R. J. Diefendorf, Fibers and matrices for high performance composites, U. S. Air Force, Report No. 729 667, 1972.

7. E. Hornbogen, The yield stress of alloys with complex microstructure, Proc. ICSMA 5, Vol. 2, Pergamon, Oxford 1980, 1337-1342.

8. E. Hornbogen, K. Kishida, TTR-diagrams for thermo-mechanical treatments of steel, Arch. Eisenhüttenw. 55 (1984) 21-24, 63-68, 281-283.

9. E. Hornbogen, K. Rittner, Development of thermo-mechanical treatments of a maraging steel for yield strength above 3 GPa, steel research 58 (1987) 172-177.

STABILITY AND COARSENING RESISTANCE OF M_2C CARBIDES IN SECONDARY HARDENING STEELS

HYUCK MO LEE*, SAMUEL M. ALLEN, MICA GRUJICIC
Department of Materials Science and Engineering
Massachusetts Institute of Technology
Cambridge, Massachusetts 02139

INTRODUCTION

The development of very high strength levels in many alloy steels is achieved by a secondary hardening process, which is a type of precipitation-hardening reaction. This reaction takes place at relatively high tempering temperatures and involves the precipitation of very fine alloy carbides. However, this reaction is preceded by the formation of metastable cementite precipitates. These precipitates are quite coarse and therefore limit the fracture toughness of many ultra-high strength martensitic steels. A prolonged tempering treatment is then required to dissolve the cementite. In order to maintain the desired strength levels after such prolonged tempering, the thermodynamic stability and ability of the fine alloy carbides to resist coarsening ("Ostwald ripening") is a major issue in alloy design.

In high Co-Ni steels containing the strong carbide-forming elements Mo, Cr and W, secondary hardening is accomplished by precipitation of fine scale M_2C alloy carbides. Thermodynamic stability and coarsening resistance of the M_2C precipitates depends on the alloy content of these elements and in general there should be an addition of these elements which is optimal with respect of these properties.

In this paper, a model is introduced for the coarsening resistance of multicomponent carbides. While the model treats the coarsening of shape-preserving particles, it is applicable to a non-spherical, in particular, rod-like particles. The model is used to study the effect of additions of Mo, Cr, and W on the coarsening kinetics of M_2C (M = Mo,Cr,W) carbides in Fe-14Co-10Ni-0.25C-Mo-Cr-W alloys. Necessary information pertaining to the equilibrium in these steels was obtained using the

THERMO-CALC software and database developed at the Royal Institute of Technology, Stockholm, Sweden (1). Experimental studies of coarsening behavior of the carbides in model alloys were made by extraction replica studies using TEM, and the results are compared with theoretical predictions.

MATERIALS AND EXPERIMENTAL PROCEDURES

The chemical compositions in weight percent of the alloys (supplied by Carpenter Technology Corp., Reading, PA) are given in Table 1. All samples were homogenized at 1200°C for 8 hr, then furnace cooled. AF1410 samples were austenized at 843°C for 1 hr, water quenched, then tempered at 510°C for 8, 16, 48, 100 and 196 hrs, and oil quenched. SRG1L samples were austenized at 1200°C for 1 hr, oil quenched, then tempered under the same conditions as AF1410. All the samples were furnace treated after being sealed in silica capsules under an Ar atmosphere, in order to prevent decarburization and oxidation.

TABLE 1

Chemical Composition of AF1410 and SRG1L (wt%)

steel	Fe	Co	Ni	Cr	Mo	C
AF1410	balance	14	10	2	1	0.16
SRG1L	balance	14	10	0	4	0.23

To produce extraction replicas, specimens were mounted, polished conventionally and etched with 5% nital. After coating with carbon, replicas were extracted in 10% nital. Photomicrographs were taken using Philips 300 and 400 transmission electron microscopes, and the carbide size distributions were obtained through the use of a Magiscan II Image Analysis System.

RESULTS

Carbide Phase Stability

The efficiency in the hardening of the steel being designed will rely on its microstructural stability. It is important to recognize that M_2C is generally not the most stable carbide phase in this type of alloy as is seen in Figure 1. This figure shows the effect of an addition of up to 0.2 wt% C on the phase diagram of Fe-14Co-10Ni-2Cr-1Mo system. Stable carbide phases are calculated to be $M_{23}C_6$ and M_7C_3 in this system. The alloy AF1410 has the composition of 0.16 wt% C on the X-axis in Figure 1. In AF1410, austenite is the stable phase above 790°C. Below this temperature, the following combinations of phases are stable: austenite + ferrite, 700 - 790°C; austenite + ferrite + $M_{23}C_6$, 595 - 700°C; austenite + ferrite + $M_{23}C_6$ + M_7C_3, below 595°C. Therefore, stable carbides in AF1410 at 510°C are $M_{23}C_6$ and M_7C_3. This calculation is one example of the use of THERMO-CALC for the calculation of phase equilibria in multicomponent systems. Phase boundaries, like those shown in Figure 1, are commonly somewhat dependent on the database used for calculations.

M_2C is not the most stable carbide phase at the tempering temperature of 510°C, but it is the phase with the highest driving force for precipitation from ferrite (martensite) (2). To maximize the amount of M_2C phase per combined additions of M and C, it is necessary to comply with the balanced composition requirement, which for M_2C is

$$X_{Mo} + X_{Cr} + X_W = 2\ X_C \qquad [1]$$

where X_i is mole fraction of element i in the steel. This requirement ensures that the amount of carbide-forming element is adjusted so that all the carbon can react to form M_2C. AF1410 is a commercial alloy and SRG1L is derived from this alloy under the following constraints of raised carbon level of 0.25 wt% and the balanced composition.

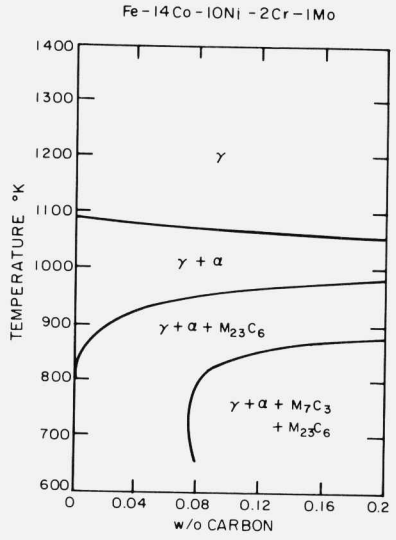

FIGURE 1. Calculated phase equilibria of Fe-14Co-10Ni-2Cr-1Mo-C system.

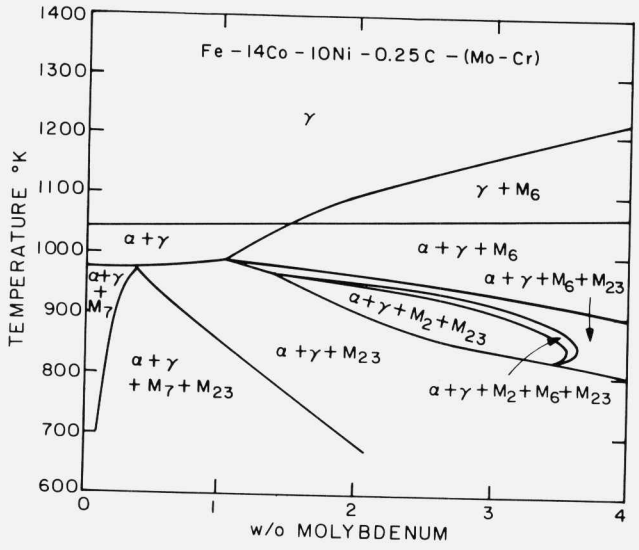

FIGURE 2. Calculated phase equilibria of Fe-14Co-10Ni-0.25C-Mo-Cr system with balanced alloy additions of Mo and Cr. M_2, M_6, M_7 and M_{23} mean M_2C, M_6C, M_7C_3, $M_{23}C_6$ carbides, respectively.

The effect of the balanced addition of Mo and Cr on the phase diagram of Fe-14Co-10Ni-0.25C system is shown in Figure 2. The left side has no Mo but Cr is added in the balanced ratio, and the composition on the right side has no Cr but Mo is only added in the balanced ratio. SRG1L has the composition of the right side of the plot. As the amount of Mo is increased, the M_6C phase becomes stable. Still, the stable carbide phase of SRG1L at the tempering temperature of 510°C is $M_{23}C_6$, although the stability of the M_6C phase is increased at high temperatures.

To optimize the ratio of Mo:Cr:W in terms of stability, many thermodynamic properties were calculated (2). Among them are the driving force for precipitation of M_2C from ferrite, the mole fraction of M_2C to precipitate from ferrite, the driving force for precipitation of more stable carbides from the metastable equilibrium mixture of ferrite + M_2C, and the driving force for precipitating carbide phases from ferrite at 510°C with balanced alloy additions of Mo, Cr and W. These results showed that Mo alone was favored as the alloy addition.

Coarsening Resistance of M_2C carbides

An additional factor to be considered is the stability of the M_2C dispersion with respect to Ostwald ripening. This coarsening resistance is necessary so that the required strength level can be maintained after the prolonged tempering that is necessary to dissolve completely deleterious cementite particles. It is quite difficult to quantify the effect of alloying elements on the coarsening resistance of the M_2C phase, since it involves the diffusion of several alloying elements. The rod shape of the M_2C phase is an additional complication. However, it is possible to define a criterion for the coarsening of M_2C carbides by combining two approachs: that of Björklund et al. (3), who considered the coarsening of multicomponent cementite particles; and that of Speich et al. (4), who considered the effects of precipitate shape anisotropy on the coarsening of rod-type copper precipitate particles in a ferrite-iron matrix.

According to the LSW coarsening theory originally developed for binary alloys (5,6) the rate equation has the following form:

$$\frac{dr}{dt} = K \frac{1}{r} \left(\frac{1}{\bar{r}} - \frac{1}{r} \right) \qquad [2]$$

$$\bar{r}^3 - \bar{r}_o^3 = \frac{4}{9} K (t - t_o) \qquad [3]$$

where dr/dt is the coarsening rate of a particle of radius r, $\bar{r}$ is the average particle radius at time t, r_o is the average particle radius at time t_o when coarsening has set in and K is the rate constant. The rate constant is a function of a number of parameters, among them are particle/matrix interfacial energy σ, molar volume of the particle phase V_m^{β}, alloy composition, diffusivity of the rate-controlling species and temperature T. The exact form of the rate constant function is dependent on the kind of assumptions made while deriving equation [2], as well as on the nature of the coarsening phase (binary, ternary, or multicomponent).

For the case of the multicomponent M_2C phase considered here, the rate constant for the coarsening of the radius of the rod-type particles is derived as follows. For both phases of α(ferrite) and $\beta(M_2C)$ Gibbs-Duhem equation is applied:

$$X_{Fe}^{\alpha} d\ln a_{Fe} + \sum_M X_M^{\alpha} d\ln a_M + X_C^{\alpha} d\ln a_C = 0 \qquad [4\text{-}1]$$

$$X_{Fe}^{\beta} d\ln a_{Fe} + \sum_M X_M^{\beta} d\ln a_M + X_C^{\beta} d\ln a_C = V_m^{\beta} dP^{\beta}/RT \qquad [4\text{-}2]$$

where,

X_i^{α} = molar fraction of element i in ferrite
X_i^{β} = molar fraction of element i in M_2C phase
a_i = activity of element i at equilibrium
R = gas constant

P^{β} = pressure due to curvature in M_2C phase. By eliminating a_{Fe} and assuming the same carbon activity due to rapid diffusion of carbon, the following relationship is obtained:

$$\sum_M (X_M^{\beta} X_{Fe}^{\alpha} - X_M^{\alpha} X_{Fe}^{\beta}) d\ln a_M = X_{Fe}^{\alpha} V_m^{\beta} dP^{\beta}/RT \qquad [5]$$

For low alloy contents a_M is proportional to X_M^{α}, which yields $d\ln a_M = dX_M^{\alpha}/X_M^{\alpha}$ and P^{β} is equal to $2\sigma_s/r$ when the equilibrium prolate spheroid shape of length l and radius r is maintained. By introducing a partitioning coefficient k_i defined as X_i^{β}/X_i^{α}, equation [5] becomes:

$$\sum_M (k_M - k_{Fe}) dX_M^{\alpha} = V_m^{\beta} d(2\sigma_s/r)/RT \qquad [6]$$

Assuming that k_M, k_{Fe} and σ_s do not change significantly with r, equation [6] has the following form:

$$\sum_M (k_M - k_{Fe})(\bar{X}_M^{\alpha} - X_M^{\alpha}) = \frac{2V_m^{\beta}\sigma_s}{RT}\left(\frac{1}{\bar{r}} - \frac{1}{r}\right) \qquad [7]$$

The term of $\bar{X}_M^{\alpha} - X_M^{\alpha}$ can be eliminated by introducing the flux to a particle shaped like a prolate spheroid (4). The flux to such a particle is given by:

$$\frac{dn}{dt} = \frac{2\pi l D}{V_m^{\alpha} \ln(l/r)} (\bar{X}_M^{\alpha} - X_M^{\alpha}) \qquad [8]$$

$$\frac{dn}{dt} = \left(\frac{X_M^{\beta}}{V_m^{\beta}} - \frac{X_M^{\alpha}}{V_m^{\alpha}}\right)\frac{dV}{dt} \qquad [9]$$

The volume and the rate of volume change of a prolate spheroid is expressed by:

$$V = \frac{4}{3}\pi r^3 \left(\frac{1}{2r}\right) \qquad [10]$$

$$\frac{dV}{dt} = 4\pi r^2 \left(\frac{1}{2r}\right)\frac{dr}{dt} \qquad [11]$$

Combining equations [7-11] and assuming that V_m^{α} is approximately equal to V_m^{β}, which is quite reasonable in this coarsening environment, the rate equation becomes exactly the same as equation [2]. For the case of the multicomponent M_2C phase considered here, the rate constant of the radius of the rod-type particles, expressed in units of $2\sigma_s V_m^{\beta}/RTln(l/r)$, is found to have the following form:

$$K = \left[\sum_M (k_M - k_{Fe})\,(k_M - 1)\,\frac{X_M^{\alpha}}{D_M^{\alpha}} \right]^{-1} \qquad [12]$$

where,

σ_s = interfacial energy of the side direction normal to the edge direction
l = dimension of the major (long) axis
r = dimension of the minor (short) axis of the rod-type M_2C carbides and therefore l/r is $2A_s$ where A_s is the aspect ratio
k_M = partitioning coefficient of element M (M = Mo, Cr and W) defined by X_M^{β}/X_M^{α}
k_{Fe} = partitioning coefficient of element Fe defined by $X_{Fe}^{\beta}/X_{Fe}^{\alpha}$
β = M_2C phase
α = ferrite matrix
X_i^{β} = molar fraction of element i in M_2C phase
X_i^{α} = molar fraction of element i in ferrite
D_M^{α} = diffusivity of element M in ferrite.

To be strictly correct, X_M^{α} in equation [12] is a concentration of alloying element M at the surface of a rod of cylindrical curvature r and therefore not a constant. However, after long time of coarsening, the effect of curvature on X_M^{α} is quite small and X_M^{α} is approximated as $X_M^{\alpha}(r=\infty)$. The rate constant of the length of the rod-type M_2C is obtained by multiplying the rate constant for the radius by $8A_s^3$.

The inverse form of a rate constant in equation [12], which is analogous to an electrical resistance, is given by the following form, where M represents Mo, Cr and W:

$$\frac{1}{K} = \frac{1}{K_{tot}} = \sum_M \frac{1}{K_M}$$

$$= \frac{1}{K_{Mo}} + \frac{1}{K_{Cr}} + \frac{1}{K_W} \qquad [13]$$

where, $$K_M = \frac{D_M^{\alpha}}{(k_M - k_{Fe})(k_M - 1)X_M^{\alpha}}.$$

A close look at this inverse form reveals that the coarsening occurs through the series-type diffusion and that the slowest moving element controls the coarsening process.

Figure 3 shows the variation of the rate constant defined by equation [12] with balanced alloy additions of Mo, Cr and W. Corners of the triangle correspond to the balanced addition of Mo, Cr and W, expressed in wt%. Each point inside the triangle also complies with the balanced composition criterion. Diffusivity data used in the computation of the rate constants are presented in Table 2. Preferred low values of rate constants are situated in the W-rich corner. There is approximately one order of magnitude difference between the W-rich side and Mo-rich side. Low values of the rate constant in the W-rich corner come from the low

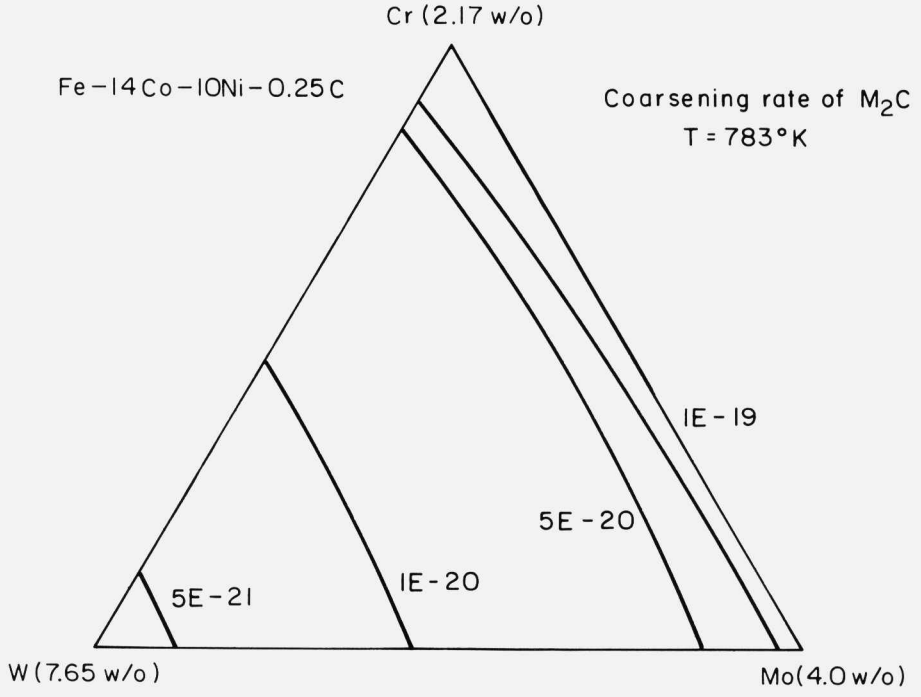

FIGURE 3. Variation of the rate constant defined by Eq. [12] for M_2C particle coarsening kinetics at 783°K with balanced alloy additions of Mo, Cr and W. Contour values shown in cm^2/sec.

diffusivity of element W. In the family of AF1410 steels, no W additions are made. In that case, an optimum combination of Mo and Cr addition is sought. That composition is still near the Mo-rich side. It is the composition of SRG1L alloy.

TABLE 2

Diffusion Coefficient Data used in Calculation of Rate Constant defined by Equation [12]

	Diffusivity, cm^2/sec	Reference
Cr	8.52 exp (-250,620/RT)	(7)
Mo	0.44 exp (-238,000/RT)	(8)
W	25 exp (-298,000/RT)	(8)

The compositions and expected carbide coarsening rates in alloys AF1410 and SRG1L will now be compared. Both alloys have the same matrix composition of Fe-14Co-10Ni. But the compositions of alloying elements and carbon are different. AF1410 has 2Cr-1Mo-0.16C while SRG1L has 4Mo-0.23C. Accordingly there should be a difference in the coarsening rate constants between these two alloys. Coarsening rate constants (cm^2/sec) defined by equation [12] are calculated to be $1.71X10^{-18}$ and $3.469X10^{-19}$ respectively in AF1410 and SRG1L. However these values must be multiplied by $2\sigma_s V_m^{\beta}/RT\ln(1/r)$. The interfacial energy of the side direction, σ_s, is not known, but we assume a value of 700 erg/cm^2, typical of an incoherent interface. The aspect ratios of M_2C carbides are taken as the measured values, 2.8 in AF1410 and 8.5 in SRG1L (see below). The molar volume of M_2C carbide is measured as 7.3853 cm^3 (9). When these values are multiplied by the rate constant defined in equation [12], the values of the coarsening rate constants (cm^3/sec) for the length and diameter of M_2C carbides in these alloys are as presented in Table 3.

TABLE 3

Calculated Coarsening Rate Constants (cm^3/sec) of Length and Diameter of rod-type M_2C Carbide in AF1410 and SRG1L tempered at 510°C

[cm^3/sec]	LENGTH	DIAMETER
AF1410	$1.23X10^{-23}$	$5.605X10^{-25}$
SRG1L	$4.24X10^{-23}$	$6.910X10^{-26}$

Experimental Results

Electron micrographs of typical carbide particles from the two alloys are given in Figure 4. The particles were rod shaped, as seen in Figure 4(a)-(b), and the aspect ratio observed in the SRG1L alloy was, on average, much greater than that in AF1410 alloy.

The average particle size versus aging time was obtained from the micrographs with the aid of image analysis system and is shown in Table 4. The numbers of particles examined for each heat treatment were several hundreds.

The particle size data obtained in the present study, given in Table 4, are plotted in Figure 5(a)-(d), as the cube of the precipitate length and diameter versus time. The data of SRG1L alloy tempered at 510°C for 196 hr is omitted from the plot because the data is far off from the general trend of SRG1L specimen. It will be discussed later. These four plots demonstrate that the cube law is an adequate description of the kinetics for bulk-diffusion controlled coarsening. Coarsening rate constants obtained from Figure 5(a)-(d) are given in Table 5. It is shown that the coarsening kinetics of M_2C carbides in SRG1L is slower than that of AF1410. The systematic downward curvature of the plot in Figure 5(a)-(d) implies that the coarsening kinetics slows down a little with time.

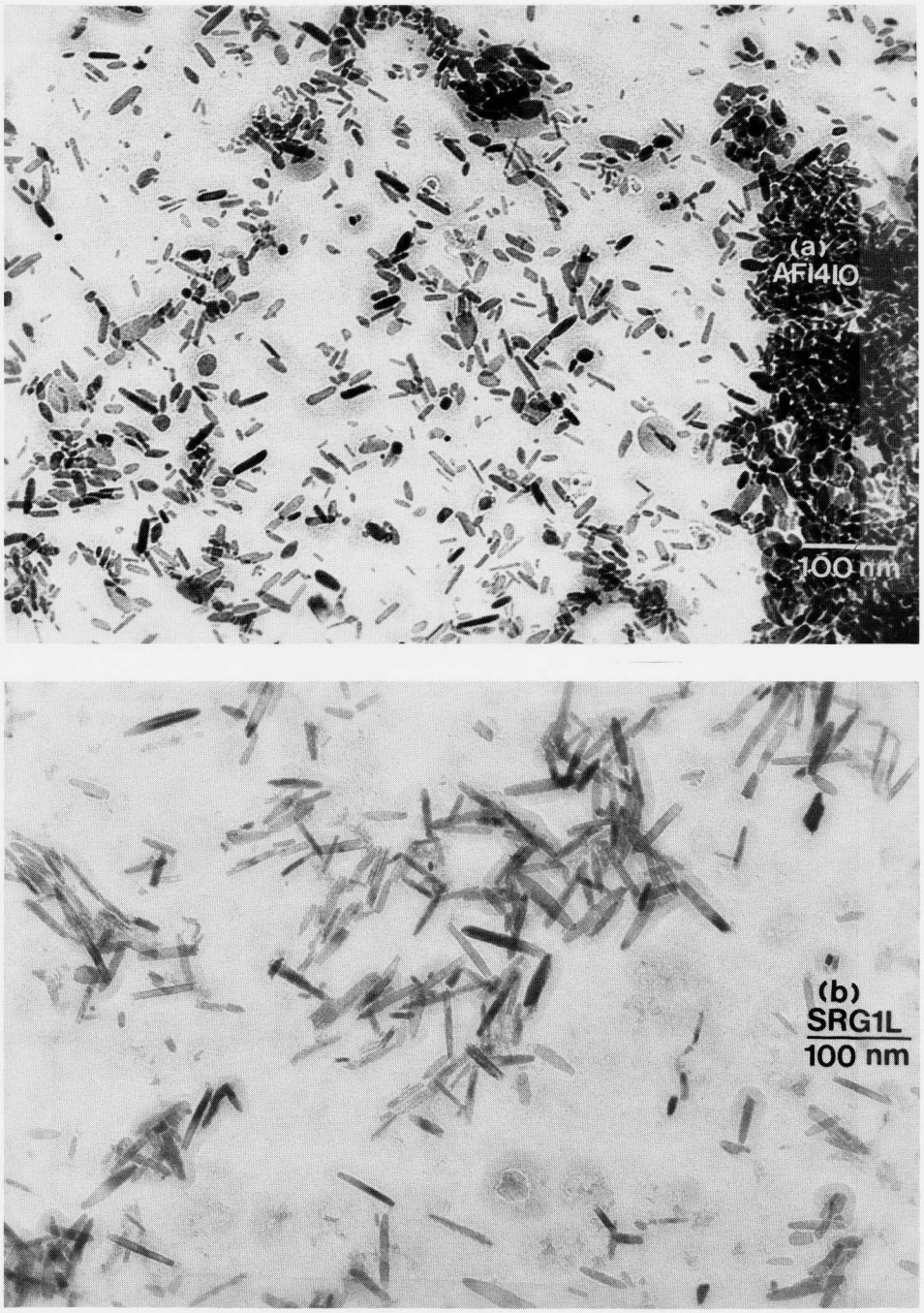

FIGURE 4. TEM micrographs showing rod-shaped M_2C carbides of (a)AF1410 and (b)SRG1L, tempered at 783°K for 196 hr.

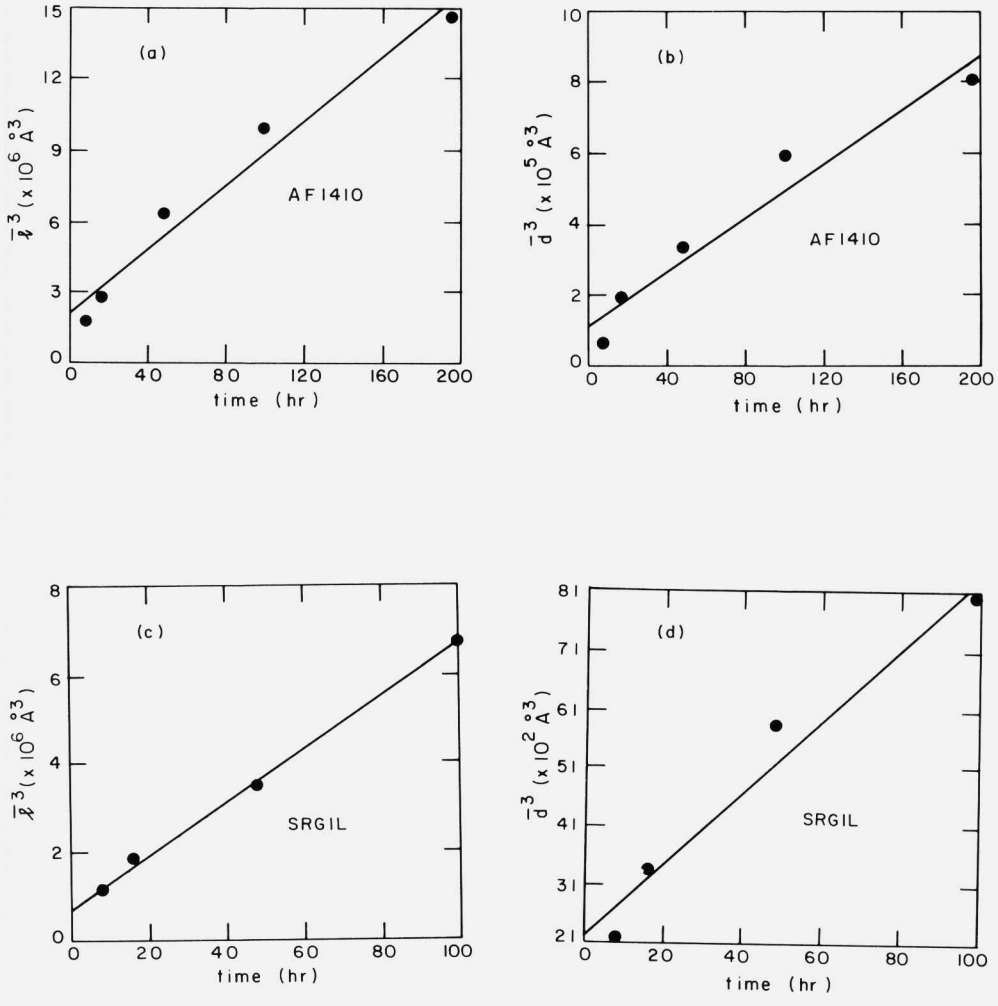

FIGURE 5. Variation of the cubed average particle size, length (l) and diameter (d), as a function of time for M_2C carbides of (a)-(b) AF1410 and (c)-(d) SRG1L tempered at 783°K.

TABLE 4

M_2C Carbide Particle Size (nm) and Aspect Ratio of AF1410 and SRG1L alloy tempered at 510°C

	AF1410			SRG1L		
Time(hr)	$\bar{l}$	$\bar{d}$	A_s	$\bar{l}$	$\bar{d}$	A_s
8	11.9	3.8	3.1	10.3	1.3	8.0
16	13.9	5.7	2.4	12.3	1.5	8.2
48	18.6	6.9	2.7	15.1	1.8	8.4
100	21.5	8.4	2.8	18.9	2.0	9.4
196	24.4	9.3	3.0	49.4	11.0	5.5

TABLE 5

Measured Coarsening Rate Constants (cm^3/sec) of Length and Diameter of rod-type M_2C Carbide in AF1410 and SRG1L tempered at 510°C

[cm^3/sec]	LENGTH	DIAMETER
AF1410	$1.867X10^{-23}$	$1.061X10^{-24}$
SRG1L	$1.666X10^{-23}$	$1.685X10^{-26}$

The size distributions of length and diameter of M_2C carbides were also obtained from Magiscan II Image Analysis System. For each histogram, several hundred particles were analyzed. They are shown in

Figure 6(a)-(d), the states tempered longest, 196 hr.

DISCUSSION

The shape of the rod-type M_2C carbides is closely approximated by a cylinder of radius r with two nearly hemispherical caps of the same radius. According as how the rods are inclined to the projected two-dimensional screen, a number of possible figures are seen on the micrographs of Figure 4(a) and 4(b). Therefore it is very difficul to measure the true dimension of the length, major axis, of the M_2C carbides, and the size distributio of the length, too. The precipitates seem to lose their original orientation when extracted from the matrix, making it hard to get a preferred orientation where the maximum dimension of the length could be measured. However, the radius of th cylinder can be obtained by measuring the maximum dimension of the minor axis regardless of the way the rod is orientated (4). Therefore it is more reliable to use the radius dimension for the analysis than the length dimension.

From the measured coarsening rates of radius, unknown parameters of the aspect ratio and the interfacial energy could be obtained. If the data o radius and length are both correct, then the aspect ratio and the interfacial energy are obtained directly from the two known rate constants. If this is true, the aspect ratio of the M_2C carbides in AF1410 and SRG1L should be 2.6 and 9.9, respectively. When these values are adopted, the calculated interfacial energy of AF1410 is 3293.6 and 1266.8 erg/cm^2, edge (major axis) and side (minor axis) direction, respectively. The interfacial energy of SRG1L is 1795.3 and 180.1 erg/cm^2, edge and side direction. From these values it would be expected that M_2C carbides in AF1410 ar incoherent in both directions and those of SRG1L maintain a kind of semi-coherency in the side direction. The numerical value of interfacial energ is changing a little when adopting a different aspect ratio. The measured average aspect ratio of M_2C carbides (average of five or four measured aspect ratios) is 2.8 in AF1410 and 8.5 in SRG1L.

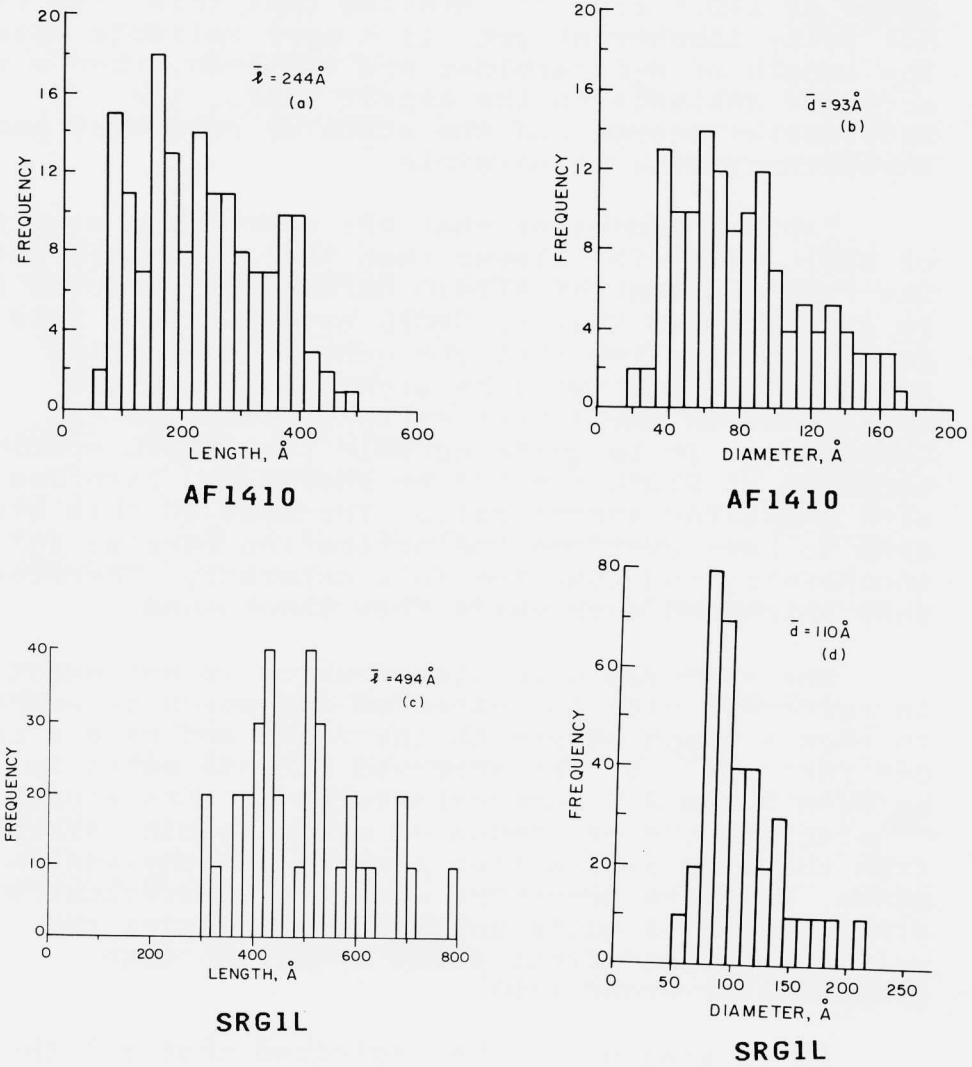

FIGURE 6. Histograms of M_2C carbide particle size, length (l) and diameter (d), of (a)-(b) AF1410 and (c)-(d) SRG1L tempered at 783°K for 196 hr.

Still the value of the interfacial energy of M_2C carbides in AF1410 are high enough for M_2C carbides to maintain incoherency. The interfacial energy of M_2C carbides to the side direction in SRG1L has a value of 170.5 erg/cm^2, hinting that this side is not fully incoherent yet. If a more reliable data on the length of M_2C carbides are achieved, then a more accurate analysis on the aspect ratio, the interfacial energy and the state of coherency and incoherency will be possible.

Table 5 indicates that the coarsening kinetics of SRG1L alloy is slower than that of AF1410 alloy. The rate constant of AF1410 defined by equation [12] is greater than that of SRG1L by 4.9 times. This fact alone implies that the general coarsening kinetics of SRG1L will be slower although the difference in the aspect ratio complicates the comparison. It is quite notable that SRG1L specimen tempered at 510°C for 196 hr showed M_2C carbides with a smaller aspect ratio. The rods at this stage seem to have overcome the activation barrier for incoherency and lost the full coherency. Therefore they thickened much while they lengthened.

The measured size distribution is not exactly in agreement with the expected one which is supposed to show a graph skewed to the right and have a cut-off ratio of 1.5. The observed cut-off ratio is between 2 and 2.5, approximately, in this study. Considering the existence of other stable carbides from the ring diffraction pattern and the austenite phase, complete agreement with the theoretical size distribution is quite unexpected. Moreover the volume fraction effect alone makes the size distribution broad (10).

It is also not to be neglected that all the carbides are not extracted properly and there may be an error coming from the different contrast used in the image analysis system. In the calculation of the coarsening rate constants, some uncertainties still exist. The value of molar volume of M_2C carbide and diffusivities of alloying elements in ferrite are not clearly known. Mole fractions and the partitioning coefficients adopted were all calculated, which is dependent on the kind of thermodynamic database.

It is suggested that this theory is presented as a guide for alloy development, with the expectation that it may not be quantitatively accurate for all purposes. However it will become clear when the research on the coarsening kinetics of M_2C carbides in new alloys is made. The compositions in weight percent of these alloys are based on Fe-16Co-5Ni-(Cr+Mo)-0.25C, which were chosen after a series of thermodynamic and kinetic calculations.

ACKNOWLEDGEMENT

This research has been supported by National Science Foundation Grant #DMR-8418718. Alloys used in this study were graciously provided by Carpenter Technology Corp., Reading, PA.

REFERENCES

1. B.Sundman, B.Jansson and J.O.Andersson. Calphad, 9, 1985, pp. 153-190.

2. M.Grujicic, H.M.Lee and S.M.Allen. Proceedings of an International Conference on User Applications of Alloy Phase Diagrams edited by Larry Kaufman, ASM, 1986, pp. 195-201.

3. S.Björklund, L.F.Donaghey and M.Hillert. Acta Metall., 20, 1972, pp. 867-874.

4. G.R.Speich and R.A.Oriani. Trans. AIME, 233, 1965, pp. 623-631.

5. I.M.Lifshitz and V.V.Slyozov. J. Phys. Chem. Solids, 19, 1961, pp. 35-50.

6. C.Wagner. Z. Elektrochem., 65, 1961, pp. 581-591.

7. A.W.Bowen and G.M.Leak. Metall. Trans., 1, 1970, pp. 1695-1970.

8. J.Arkill and V.K.Wöhlbier as cited in A.T.Davenport and R.W.K.Honeycombe. Metal Science, 9, 1975, p. 207.

9. H.Morikawa, H.Komatsu and M.Tanino. J. of Elect. Micro., 22, 1973, pp. 99-101.

10. P.W.Voorhees. J. of Stat. Phys., 38, 1985, pp. 231-252.

KINEMATICS OF M_2C CARBIDE PRECIPITATION

J.S. MONTGOMERY*[1,2], G.B. OLSON[2,1]
(1)Metals Research Branch, Army Materials Technology Laboratory, Watertown, MA 02172; (2)Department of Materials Science and Engineering, Northwestern University, Evanston, IL 60208

INTRODUCTION

Research by Speich et al. (1) has elucidated steel compositions with a unique combination of strength and toughness. These steels contain 10 wt.% nickel to lower the transition temperature to well below room temperature, and to ensure high hardenability. Molybdenum additions increase hardenability, retard temper embrittlement, and, in combination with carbon, promote secondary hardening reactions in which alloy carbides are formed (2). Chromium is generally added to increase hardenability and to enhance the secondary hardening response. The role of cobalt is least clearly understood, but it is thought (1) to (a) retard the recovery of the dislocation substructure, (b) provide a finer dispersion, and (c) provide a small amount of solid-solution strengthening. The finer precipitate may arise because (a) heterogeneous nucleation on dislocations accelerates nucleation at low temperatures in an unrecovered matrix, and (b) since cobalt raises the activity of carbon in ferrite, decreasing the solid solubility of the alloy carbide (3), this increases the supersaturation and nucleation rate (4,5,6). Equivalent to

raising the activity of carbon, Goldschmidt (7) proposes that cementite dissolves cobalt but is rendered progressively less stable, Co_3C being an entirely unstable carbide. The toughness of these alloys is primarily due to the fineness of the carbides, the low impurity level, and the slightly overaged structure which eliminates the embrittling cementite phase.

The goal of modification of these steels is improved strength with minimal loss of toughness. Control of precipitation processes is essential to achieving higher strength while maintaining the microstructural basis of high toughness. Atom-Probe/ Field-Ion Microscopy (AP/FIM) has been used to study precipitation of M_2C in AF1410 (8,9), giving carbide compositions as a function of tempering time at 510°C, as well as rough sizes and shapes of the carbides. However, crystallographic parameters and interfacial features cannot be readily obtained with this technique, and carbide coherency loss has to be inferred from a morphology change. Determining the coherency loss mechanism(s) for these carbides is important, since, as coherency decreases, the interfacial energy increases, increasing the coarsening rate and thus decreasing the strength and toughness of the steel. Coherency loss should therefore be delayed at least until precipitation is complete and all cementite is dissolved.

The purpose of this study is to determine the carbide state of coherency at the earliest possible tempering time, and the mechanism(s) of coherency loss as the carbide grows/ coarsens in Co-Ni secondary hardening steels using Transmission Electron Microscopy (TEM). This paper reports progress in this study.

Background: Precipitation Kinematics

A general approach to the crystallography and kinematics of phase transformations has been recently put forward by Olson and Cohen (10). In any theory of crystalline interfacial structure for a coherent particle, it is necessary to establish a lattice correspondence which relates the identity of lattice planes and directions in the two crystal structures which meet at the interface. This correspondence then defines a lattice deformation which is an affine transformation describing the homogeneous distortion of a unit cell of one structure to that of the other. In matrix notation, a lattice deformation $\tilde{S}$ can be factored into a pure strain $\tilde{B}$ and a rigid-body rotation $\tilde{R}$;

$$\tilde{S} = \tilde{R}\tilde{B}. \qquad [1]$$

When one or both of the crystal structures involves a basis, additional inhomogeneous atom displacements termed shuffles may occur within the unit cell which, as such, do not contribute to the distortion of lattice vectors.

Once the lattice deformation has produced the correct structure of the transformation product, any further deformation must be lattice invariant, which produces a change of shape without altering the lattice. A particle can then reduce its coherency by a lattice-invariant deformation $\tilde{P}$. This can occur by any of the usual mechanisms of conventional plastic deformation in crystals, such as the glide and climb of crystal lattice dislocations or mechanical twinning, and

will be subject to the usual constraints of crystal plasticity. Macroscopic (long-range) cancellation of a component of the homogeneous lattice deformation is most effectively accomplished by a uniform periodic array of lattice dislocations or twins (10). The result of all these deformations is the particle's macroscopic shape change $\tilde{E}$, expressed by

$$\tilde{E} = \tilde{R}\tilde{B}\tilde{P}, \qquad [2]$$

where $\tilde{E}$ is the macroscopic shape change, $\tilde{R}$ is the rigid-body rotation, $\tilde{B}$ is the lattice deformation, and $\tilde{P}$ is the inhomogeneous lattice-invariant deformation.

A lattice deformation can be visualized by considering how a general distortion deforms a sphere of unit radius. The general pure strain $\tilde{B}$ distorts the sphere into an ellipsoid with three unequal semi-axes. When at least one of the semi-axes is greater than unity and at least one other is less than unity, the sphere and the ellipsoid intersect, defining a right elliptic "Bain" cone with its apex at the origin. The total lattice deformation RB can then be an invariant-line strain (ILS) which leaves a particular direction undistorted and unrotated. Combining the lattice deformation with an appropriate $\tilde{P}$ in the form of of a simple shear can then make $\tilde{E}$ an invariant-plane strain (IPS) which is a deformation leaving a particular plane macroscopically undistorted and unrotated. Adopting this plane as the habit of a plate-shaped semicoherent particle minimizes its strain energy. Several mathematical procedures have been developed to analyze the crystallography of semicoherent IPS transformations (11,12,13).

In generalizing these concepts, Olson and Cohen (10) have discussed three principles governing the orientation relations and morphology of transformation products:

Principle 1: The rigid-body rotation accompanying the transformation of an enclosed particle will minimize rotations of directions of maximum dimension.

Principle 2: A transformed particle which minimizes strain energy will maximize its dimensions in directions of minimum distortion.

Principle 3: A particle which minimizes surface energy will adopt a morphology which maximizes the coincidence of lattice sites in its interface.

In a study of aging phenomena in ferrous martensites, Taylor (14) observed the precipitation of orthorhombic ϵ'-carbide as plates via high resolution TEM. This carbide has the same crystal structure as Mo_2C, but different lattice parameters. These plates exhibited an orientation relationship with the matrix analogous to that proposed by Jack (15) for hexagonal ϵ-carbide, namely,

$$(001)_{\epsilon'} \;//\; (011)_f$$
$$[100]_{\epsilon'} \;//\; [100]_f$$

These carbides exhibit extensive faulting on their "basal" plane that appears to be an internal accomodation mechanism necessary to achieve an IPS which minimizes the total strain energy. The transformation strain of the semicoherent precipitate was analyzed as an IPS with inhomogeneous shear $\tilde{P}$ on $\{011\}_f$ (the type of plane from which the carbide basal plane

is derived). A BCC → orthorhombic lattice deformation was adopted, and a computerized version of the procedure developed by Bowles and MacKenzie (11) (originally to analyze the crystallography of the martensite transformation in steels) was used. Figure 1 (14) shows a cubic [100] stereogram depicting the Bain cone for the BCC → ε'-carbide lattice deformation in Fe-25Ni-0.4C. The intersection of the internal shear plane and the cone defines two posible invariant lines (x_i). The predicted habit plane normal corresponding to the $[3\bar{1}1]$ invariant line (and $[2\bar{1}\bar{1}]$ invariant normal) is designated by "$P_1(x_2, n_2)$," and is close to the observed (102) habit. The predicted orientation relationship was also consistent with electron diffraction patterns.

The lattice correspondence used by Taylor can be stated formally by the matrix expression

$$\vec{b} = [bCo]\ \vec{o}, \qquad [3]$$

where $\vec{b}$ is a vector in the parent BCC lattice, $\vec{o}$ is a vector of the product orthorhombic lattice, and [bCo] is a 3X3 matrix which describes the lattice correspondence, namely,

$$[bCo] = \begin{bmatrix} 100 \\ 0\bar{1}1 \\ 0\bar{1}1 \end{bmatrix}.$$

The crystal structure of hexagonal carbides is shown in Figure 2 (16). This structure can be seen to be an HCP structure of

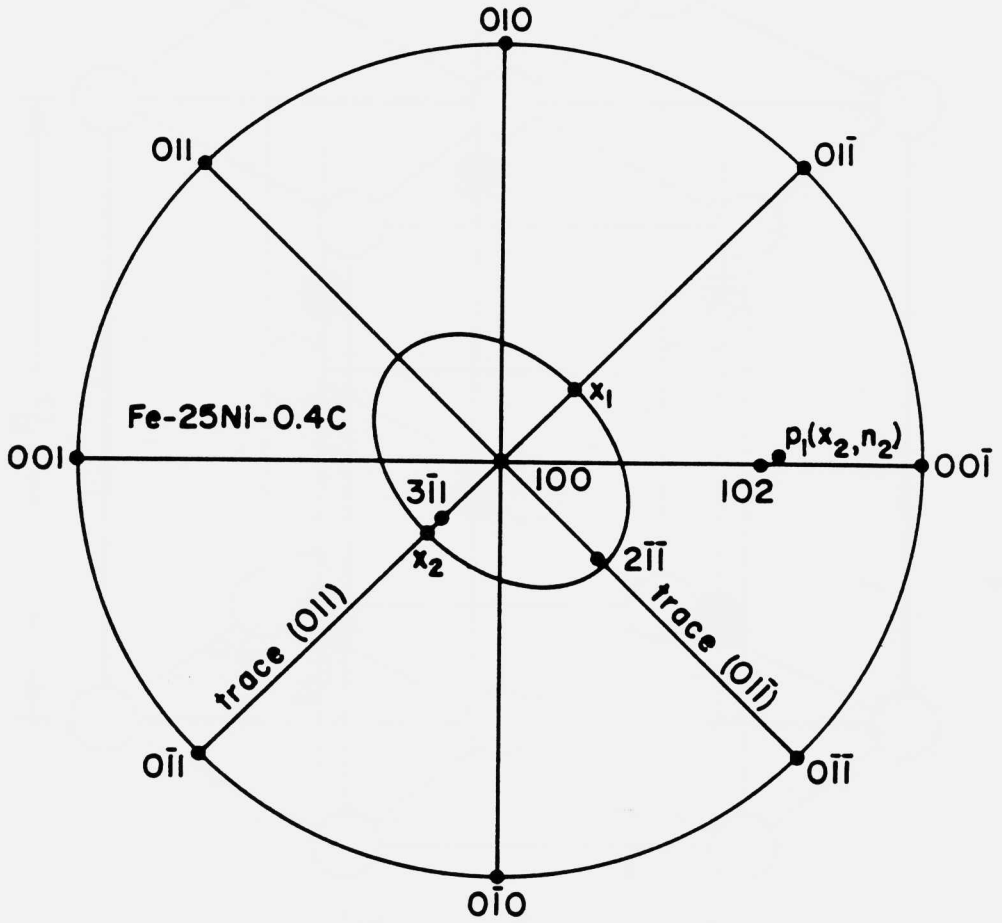

Figure 1: Cubic [100] stereogram depicting the Bain cone for the BCC → ε'-carbide lattice deformation in Fe-25Ni-0.4C. (After reference 14.)

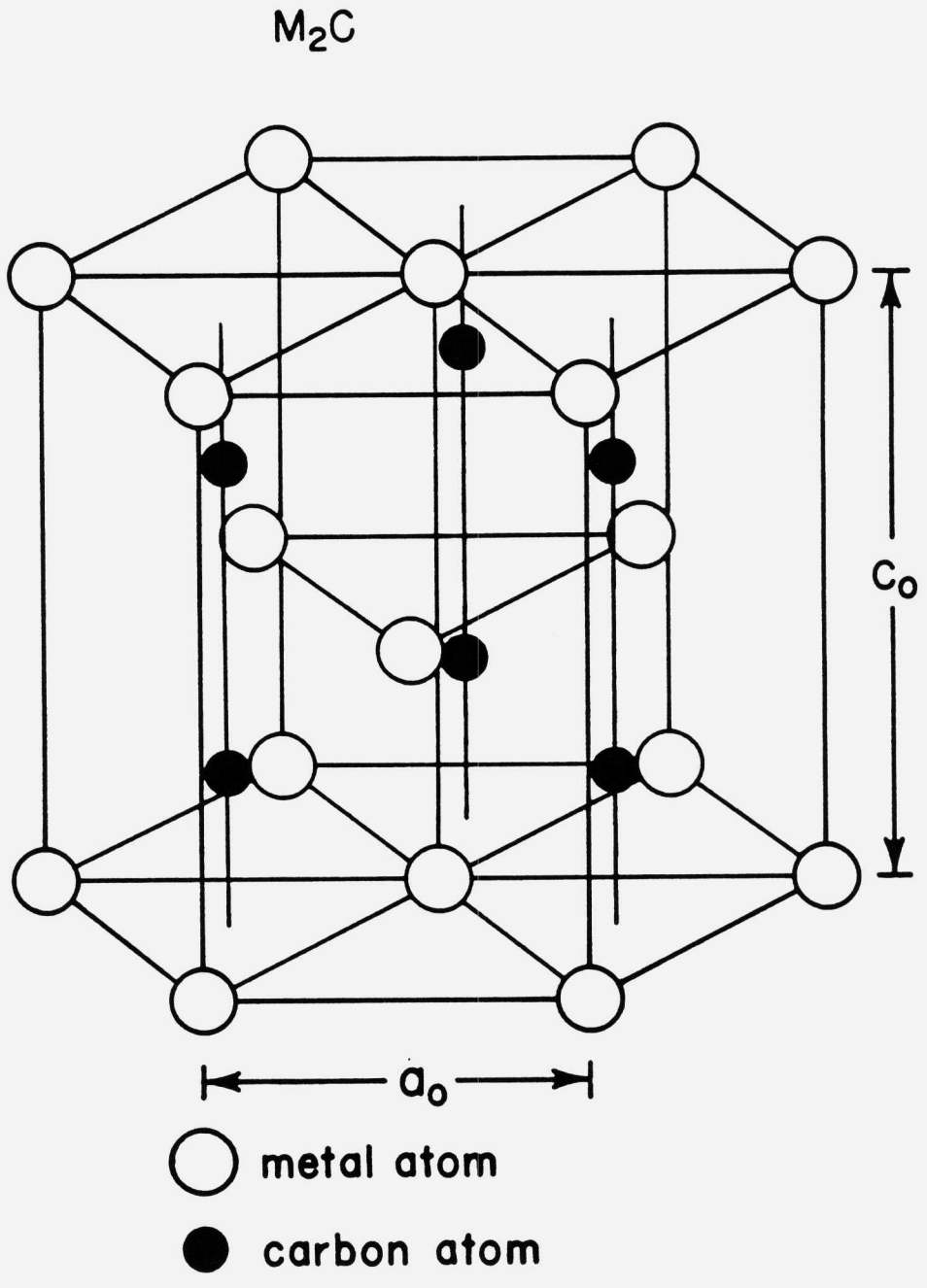

Figure 2: Crystal structure of M_2C hexagonal carbides. (After reference 16.)

metal atoms with carbon atoms in octahedral interstices. One-third to one-half of the octahedral sites are occupied by carbon atoms, depending on the chemical composition. For example, the composition of ε-carbide varies from Fe_3C to Fe_2C. In general, when carbon atoms take on an ordered arrangement in M_2C, a small orthorhombic distortion results, so that the "general" M_2C can be considered orthorhombic with b_c/a_c possibly deviating from the hexagonal value ($\sqrt{3}$). In order to compare the principal strains of the coherent lattice deformation, all possible M_2C carbides were taken from the literature (primarily from the JCPDS card file (17)) and converted to a common orthorhombic unit cell, Table 1. Principal strains defined by

$$\epsilon_{11} = [a_c/a_f] - 1$$

$$\epsilon_{22} = [\sqrt{3}a_c/\sqrt{2}a_f] - 1$$

$$\epsilon_{33} = [c_c/\sqrt{2}a_f] - 1 \qquad [4]$$

were then evaluated using $a_f = 2.870\text{Å}$ for the alloys of interest here.

TABLE 1

M_2C LATTICE PARAMETERS AND TRANSFORMATION STRAINS

Carbide	a_c (Å)	b_c (Å)	c_c (Å)	ϵ_{11}	ϵ_{22}	ϵ_{33}
ϵ-Fe_2C	2.754	4.770	4.349	-0.040	0.175	0.072
Cr_2C	2.826	4.895	4.465	-0.015	0.206	0.100
$(Cr,V)_2C$	2.868	5.008	4.530	-0.001	0.232	0.116
V_2C	2.871	5.037	4.577	0.000	0.241	0.128
$(Cr,Mo)_2C$	2.890	5.007	4.560	0.007	0.233	0.124
W_2C	2.997	5.191	4.728	0.044	0.279	0.165
$Mo_2C_{.9}$	3.002	5.200	4.725	0.046	0.281	0.164
Mo_2C	3.012	5.218	4.735	0.050	0.286	0.167

Starting with Mo_2C, one can see that the carbide can reduce its transformation strains by becoming carbon-deficient (adding vacancies), and by substitution by other metals; "mixed" M_2C carbides exhibit lattice parameters between those of their pure components. For Fe_2C and Cr_2C, ϵ_{11} actually becomes negative, satisfying the condition for an invariant line strain.

Using the previous data, the effect of coherency on the carbide composition (through strain energy) was calculated for AF1410 at 510°C using a modified Thermocalc™ program by Grujičić (18). The lattice parameters of the carbide were then back-calculated from the principal strains found in that work, Table 2.

TABLE 2

LATTICE PARAMETER CALCULATIONS

Equilibrium	Composition of M_2C Phase	a_c (Å)	b_c (Å)	c_c (Å)
coh. nucleation	$(Cr_{.49}Mo_{.39}Fe_{.12})_2C_{.79}$	2.83	4.92	4.53
coherent	$(Cr_{.63}Mo_{.32}Fe_{.05})_2C_{.82}$	2.82	4.90	4.52
incoherent	$(Cr_{.64}Mo_{.36}Fe_{.00})_2C_{1.0}$	2.86	4.96	4.54

Because of the assumptions and approximations of that work, what is important here is not the absolute values of the parameters, but the relative change between them. One can combine the orthorhombic a_c- and b_c-parameters into one equivalent hexagonal a_c'-parameter using equal basal plane areas:

$$a_c' = [a_c b_c/\sqrt{3}]^{1/2} \qquad [4]$$

One then obtains a change in a_c' of 0.03Å between the coherent and incoherent equilibria.

When Mo_2C precipitates in a ferritic matrix it assumes the morphology of rods or needles (19,20). Using Transmission Electron Microscopy (TEM), the orientation relationship and habit direction of Mo_2C in ferrite was determined in 1966 by Dyson et al. (21). Referring the carbide to an HCP lattice, they found the orientation relationship is best represented as:

$$(0001)_c \;//\; (011)_f$$
$$[2\bar{1}\bar{1}0]_c \;//\; [100]_f,$$

which is identical to that postulated by Pitsch and Schrader (22) for ε-carbide in ferrite, and analogous to the Jack orientation relationship. With respect to the coherent lattice deformation, this relationship corresponds to nonrotation of the principal axes. A stereographic projection for this relationship is shown in Figure 3. Dyson et al. also found that the habit direction of the Mo_2C needles is perpendicular to $(2\bar{1}\bar{1}0)_c$, which is parallel to one of the cubic cell edges of ferrite, viz., $[100]_f$. This direction coincides with the principal axis of smallest strain (ϵ_{11}) of the coherent BCC → orthorhombic lattice deformation. Tanino et al. (23) also reported the Pitsch and Schrader orientation relationship, as well as the $[100]_f$ habit direction. A figure for the arrangement of Mo and Fe atoms on the $(0001)_c$ // $(011)_f$ plane is shown in Figure 4 (24), illustrating the relatively good matching along $[2\bar{1}\bar{1}0]_c$ // $[100]_f$, corresponding to ϵ_{11}. In addition, Tanino et al. interpreted features within overaged Mo_2C needles with an average spacing of 30Å as Moiré fringes. This spacing is in good agreement with the value calculated from the difference in the interplanar spacings of $(2\bar{1}\bar{1}0)_c$ and $(002)_f$. They also showed a TEM micrograph of a 7.3Mo-0.17C steel that exhibited diffraction contrast due to the coherency strain around under-aged Mo_2C precipitates.

However, Davenport (25), in a study of secondary-hardening steels, interpreted similar features with 60Å spacing within both overaged Mo_2C and W_2C carbides not as Moiré fringes, but as interfacial dislocations. This was because

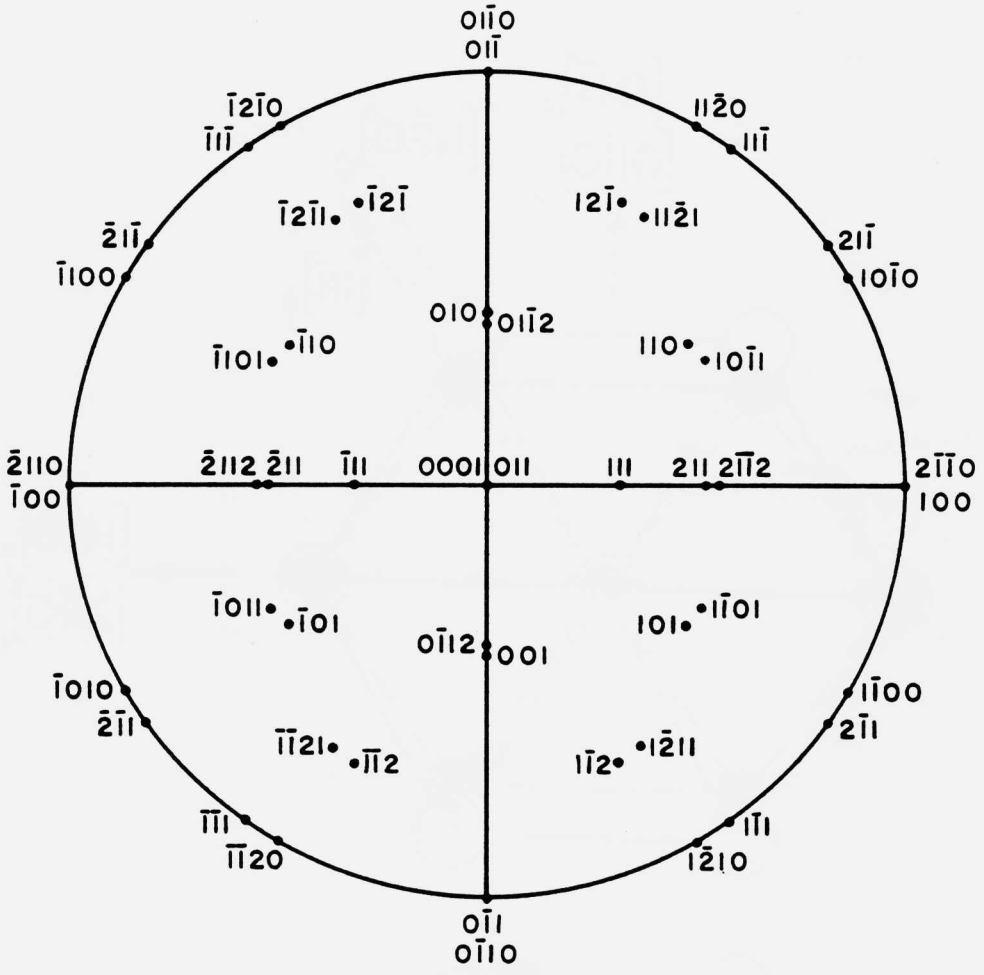

Figure 3: Stereographic projection of M_2C in ferrite based on the Pitsch-Schrader orientation relationship. (After reference 21.)

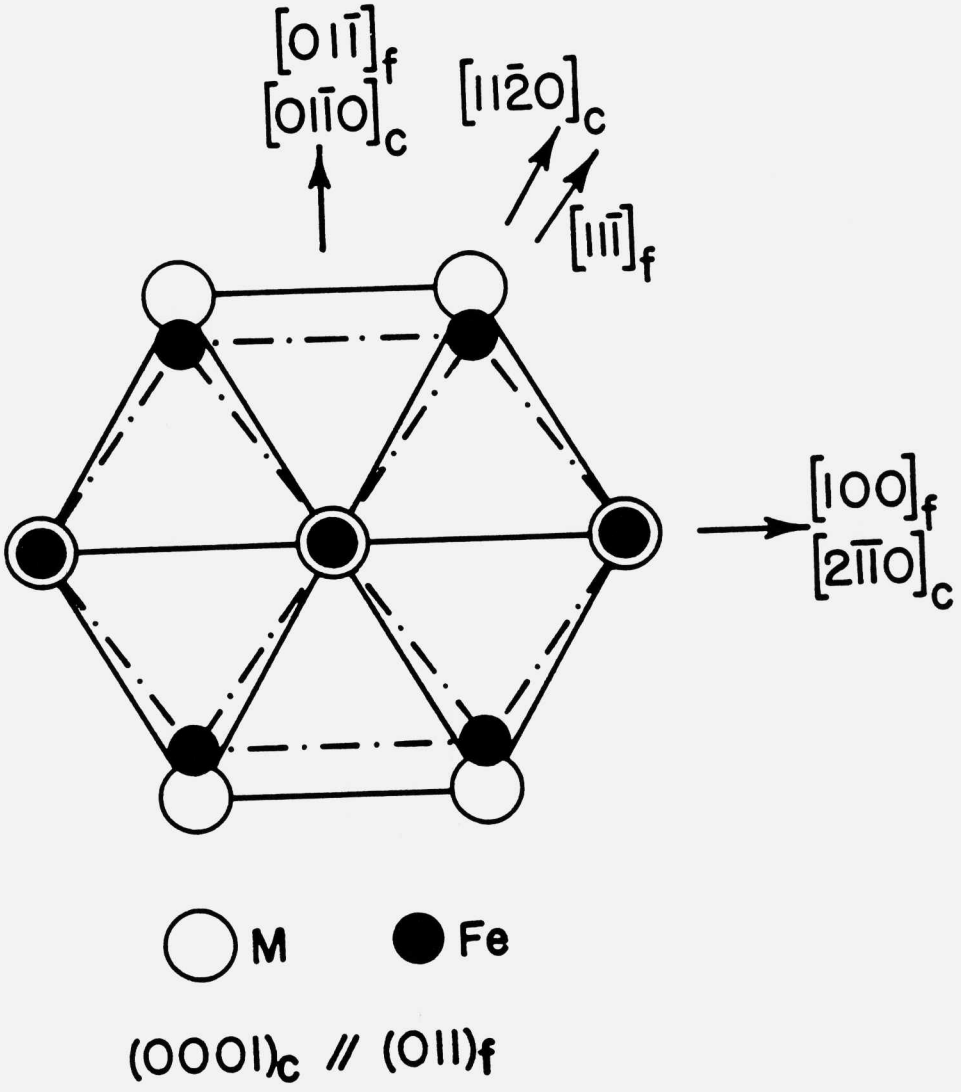

Figure 4: Orientation relationship between M_2C precipitates and ferrite matrix. (After reference 24.)

the fringes were resolved in dark field micrographs taken from the carbide reflections only. Davenport also tried to duplicate the result of Tanino et al. of coherent under-aged Mo_2C precipitates without success in his 3.45Mo-0.22C steel, so an 8.20Mo-0.22C steel was made. On quenching this steel from 1300°C, up to ~30% δ-ferrite was observed in the martensite. Due to preferential electropolishing, the apparent density of this phase was increased in thin foils to such a degree that the martensite structure was only occasionally observed. The δ-ferrite was relatively defect-free and after tempering for a short time, e.g. 3 minutes at 700°C, a fine dispersion of Mo_2C needles lying along the cube directions was resolved. These needles were seen to exhibit extensive streaking in diffraction patterns. It was concluded that the results of Tanino et al. concerning the nature of the Mo_2C-ferrite interface were drawn from observations on δ-ferrite.

Taylor found in his analysis (14) that as ϵ_{11} approaches 0, the invariant line (Figure 1) moves closer to [100], shrinking the Bain cone, and moving the habit plane towards (001). For the case where $\epsilon_{11} \geq 0$, an IPS solution based on a single lattice-invariant shear is no longer possible. This corresponds to the case of Mo_2C with the Pitsch-Schrader orientation relationship. However, an invariant-line strain (ILS) or near-invariant line strain may still be realizable, dependent upon the operation of an appropriate inhomogeneous lattice-invariant deformation $\tilde{P}$, which would result in the observed rod-shaped particles along [100]. The expected behavior is illustrated in Figure 5. Figure 5a shows a fully coherent ellipsoidal particle, edge-on to the basal plane $(0001)_c$ // $(011)_f$, along with the macroscopic shape change ellipse. Figure 5b shows an ILS semicoherent particle in the

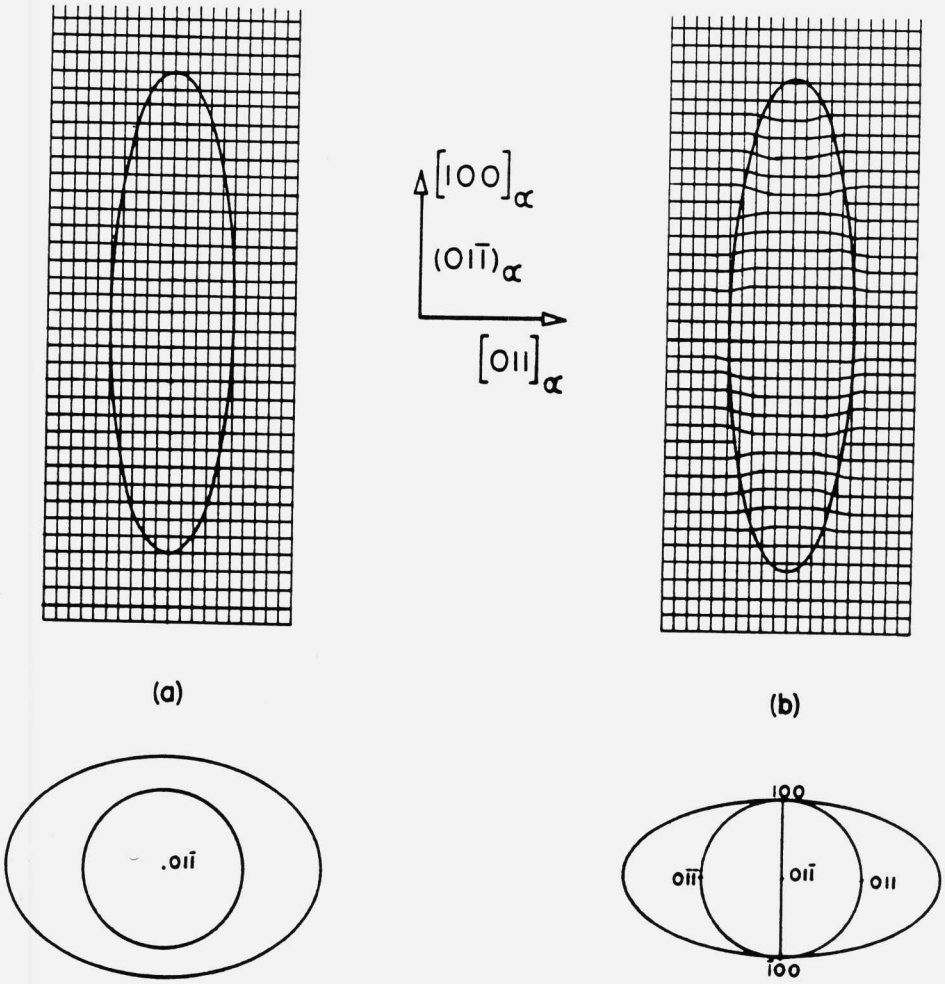

Figure 5: Ellipsoidal carbide particles edge-on to the basal plane, with associated deformation ellipses (schematic). (a) Fully coherent case, (b) semicoherent ILS case.

same orientation. For the fully coherent case, the interfacial energy is a minimum, and because there is a minimum misfit along $[100]_f$, the particle maximizes its dimension in this direction (Principal 2). Here the macroscopic shape change ellipse does not intersect the unit sphere. For the ILS case, because of the coherency loss associated with the internal accomodation deformations pictured, the ellipse just touches the unit sphere at two points, defining a line (and so an ILS) along $[100]_f$.

MATERIALS AND METHODS

Materials

Commercial AF1410 steel was supplied by Carpenter Technology Corporation as 1/2-inch square bar, austenitized (830°C/1.5h), oil quenched, and deep-freeze-treated (-75°C/1h). The experimental alloy "1410-4Mo" was also examined. This Cr-free composition has a Mo content balanced to the C content in the stoichiometric ratio of M_2C and provides a dispersion of the simpler Mo_2C carbide in the same 14Co-10Ni matrix as AF1410. This alloy was also supplied by Carpenter as 3/4-inch square hot-rolled bar, that was subsequently austenitized (1250°C/8h), and oil quenched. The composition of these alloys is shown in Table 3. Samples of the alloys were tempered at 510°C for 1 to 200h.

TABLE 3

ALLOY COMPOSITIONS (wt.%)

Alloy	C	Co	Ni	Cr	Mo	Fe
AF1410	0.163	14.24	10.21	2.10	1.03	bal.
1410-4Mo	0.230	14.17	10.24	0.06	3.96	bal.

Methods

A Philips EM400T Transmission Electron Microscope was used primarily, with some of the work performed on a JEOL 200CX. 3mm discs were punched out of pre-thinned sheet, finish-ground, and electropolished with 5% perchloric acid in methanol at -50°C (±5°C), 25V. Chromic-acetic acid solutions were tried without success.

It was found that an oxide film would rapidly form on the surface of thinned foils that only sometimes could be removed by ion milling. This film gave Moiré fringe contrast starting at carbides, then proceeding to patches in the matrix, and finally covering the entire surface with fringes. To permit easier viewing of more carbides as well as measurement of their lattice parameters, carbon extraction replicas were used. Between 10 and 20 carbides were measured for each tempering treatment. The sizes and shapes of the carbides were cross-checked between the two techniques.

For most of this work, samples were mounted in bakelite, ground through 600 grit, given a chemical polish (8% H_2O_2, 15% H_2O, 5% HF), and a thin layer of carbon evaporated onto the

surface. This carbon layer was stripped with 5% bromine in methanol at -20°C (±10°C), given successive washes in methanol and collected on 400 mesh copper grids. For lattice parameter work, 50-100Å of reagent grade aluminum was evaporated onto the replica to provide an internal calibration which resulted in reducing the error in the d-spacings to ±0.01Å. It was found that using a separate (external) standard gave inaccurate results, even with extreme care.

RESULTS

Thin Foils of AF1410

Figure 6 shows four TEM dark-field micrographs of AF1410, using carbide reflections, for samples tempered for 1, 5, 16, and 100h at 510°C. In the 1h condition, the carbides are just barely observable as 20-60Å particles, seen primarily on dislocations. The dislocation density is extremely high. After 5h, the carbides are more easily observed as 150Å ellipsoids. The dislocation density is still very high, but consists of more regularly-spaced networks. After 16h, the carbides have not coarsened appreciably and are still about 200Å long. There are patches of dislocation-free areas. In the 100h condition, the carbides have coarsened to about 300Å in length, and the matrix appears fully recovered.

The orientation relationship of the carbides with the matrix was not systematically determined, but the observed diffraction patterns were consistent with the Pitsch-Schrader orientation (Figure 3).

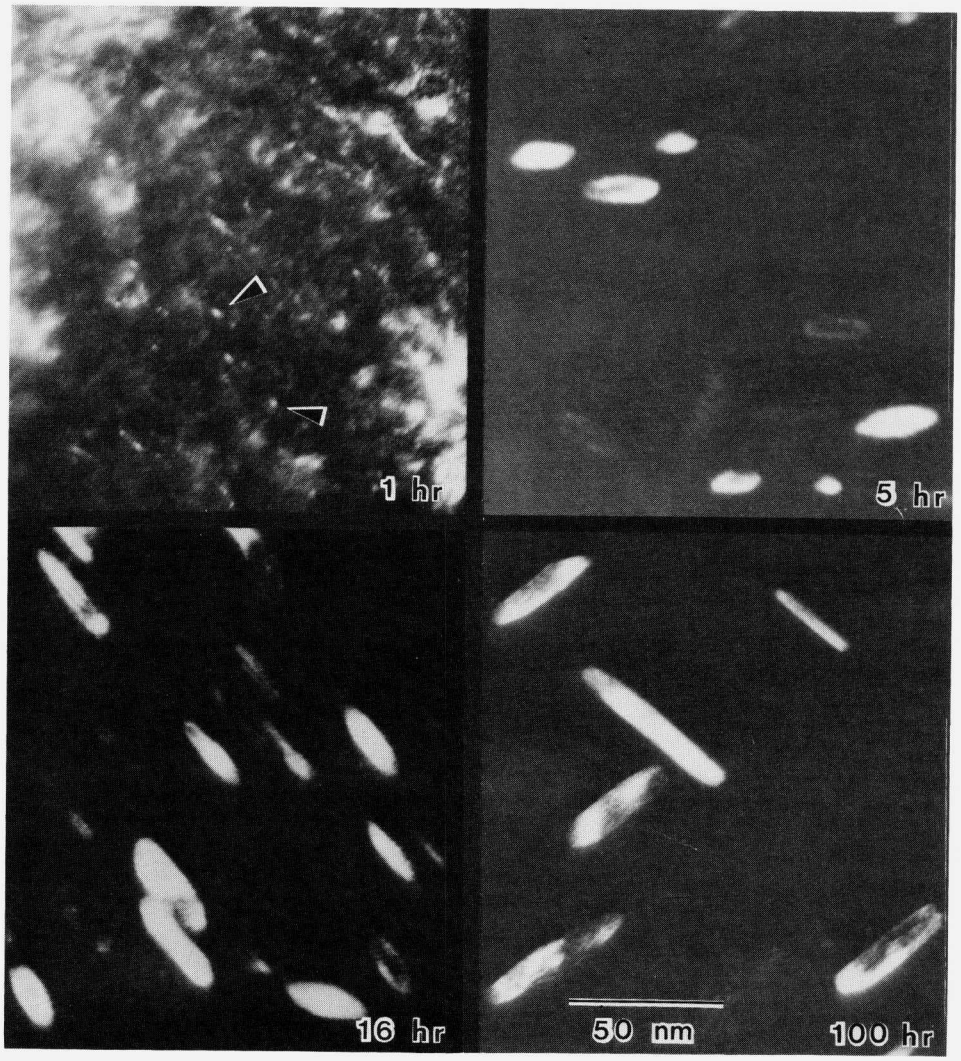

Figure 6: Dark field TEM micrographs of M_2C precipitates in AF1410, using carbide reflections. Steel tempered at 510°C for the times shown.

The width-wise type of fringes in the carbides reported by Tanino et al. (23) and Davenport (25) were not observed in the AF1410 M_2C carbides. Other fringes attributed to an oxide surface layer were, however, observed. The presence of this tenacious oxide film was one reason for the move to the use of carbon extraction replicas.

Carbon Extraction Replicas

Figure 7 shows the length of the M_2C carbides as a function of tempering time at 510°C for AF1410. The triangles are data from a preliminary FIM investigation by Liddle et al. (9), and the connecting line is dashed because of problems with local magnification at these sizes. The circles are from the present extraction replica results. The data overlap nicely in the 3-16h region. At the far right-hand side (>100h) is a reference slope of 1/3 from LSW coarsening theory (26,27).

Figure 8 shows some preliminary results for the 1410-4Mo steel: at 1h, the carbides are about the same length as those of AF1410, but they are narrower (aspect ratio β larger), and therefore, smaller overall. Again, at long times (>100h) there is a reference slope of 1/3.

Individual carbides from both steels with various tempering conditions were carefully examined for signs of internal faulting. In no case was such faulting observed, within the resolution of the technique used.

The M_2C carbide lattice parameters are shown in Table 4 for AF1410 and 1410-4Mo, tempered at 510°C for 1 to 196h. The

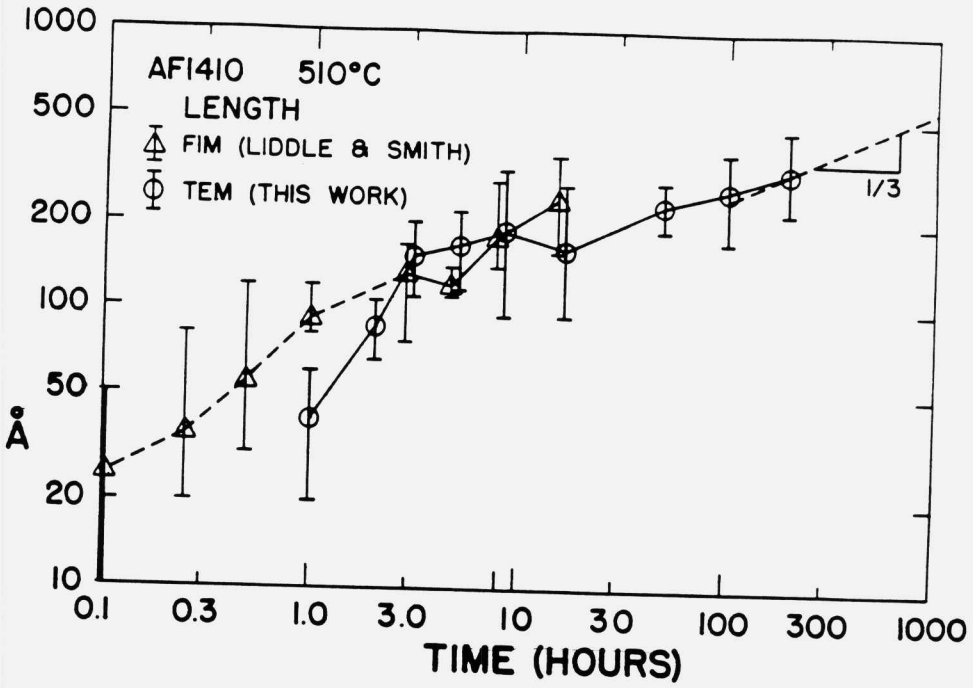

Figure 7: Length of M_2C carbides extracted from AF1410 as a function of tempering time at 510°C.

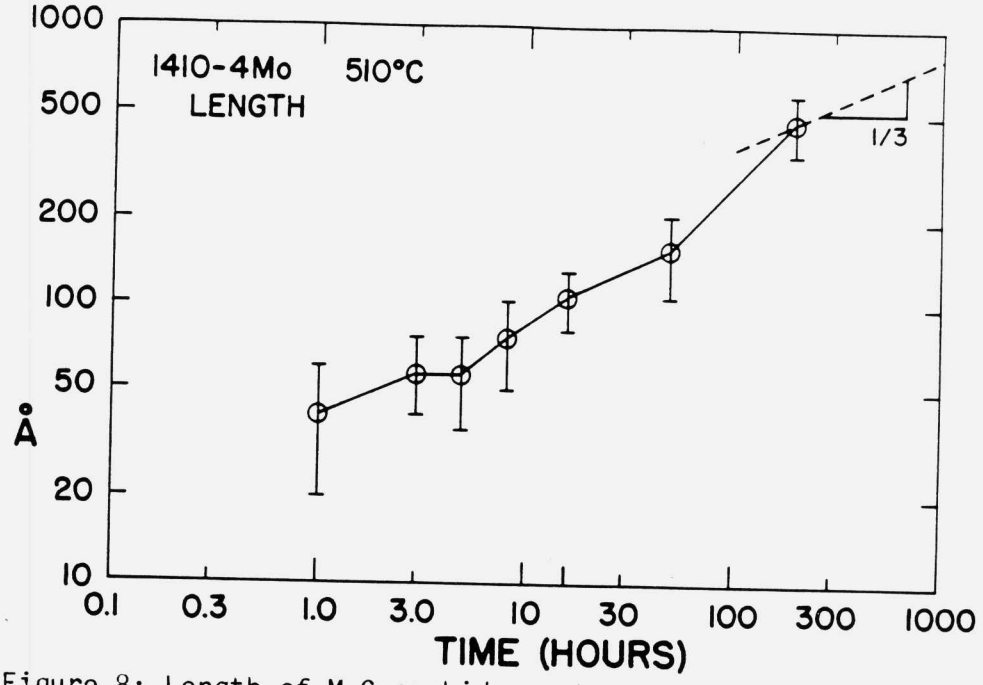

Figure 8: Length of M_2C carbides extracted from the 1410-4Mo steel as a function of tempering time at 510°C.

a_c' parameter here is the a-parameter of the carbides assuming an hexagonal crystal structure with no orthorhombic distortion.

TABLE 4

CARBIDE LATTICE PARAMETERS (Å)

	1h	3h	5h	8h	16h	48h	100h	196h
AF1410								
a_c'	----	2.88	2.88	2.88	2.89		2.90	2.90
c_c	----	4.52	4.52	4.52	4.54		4.55	4.55
1410-4Mo								
a_c'	2.97	2.99	2.99	2.99	3.00	3.00	3.00	3.00
c_c	4.68	4.73	4.73	4.73	4.74	4.74	4.74	4.74

The AF1410/1h carbide lattice parameters could not be determined because of diffuseness of the rings, probably due to a composition range of the carbides, giving a range of lattice parameters. For AF1410, a_c' is constant at 2.88Å until 16h, where there is an upward shift. At 100h and beyond a_c' is constant at 2.90Å. For 1410-4Mo, 1h carbides have a_c' of 2.97Å, then there is an upward shift, and 16h and beyond they show an a_c' of 3.00Å. It is proposed that these shifts of 0.02Å and 0.03Å respectively correspond to the carbide composition shifts associated with loss of coherency of the carbides.

Figure 9 is a composite figure showing the M_2C carbide

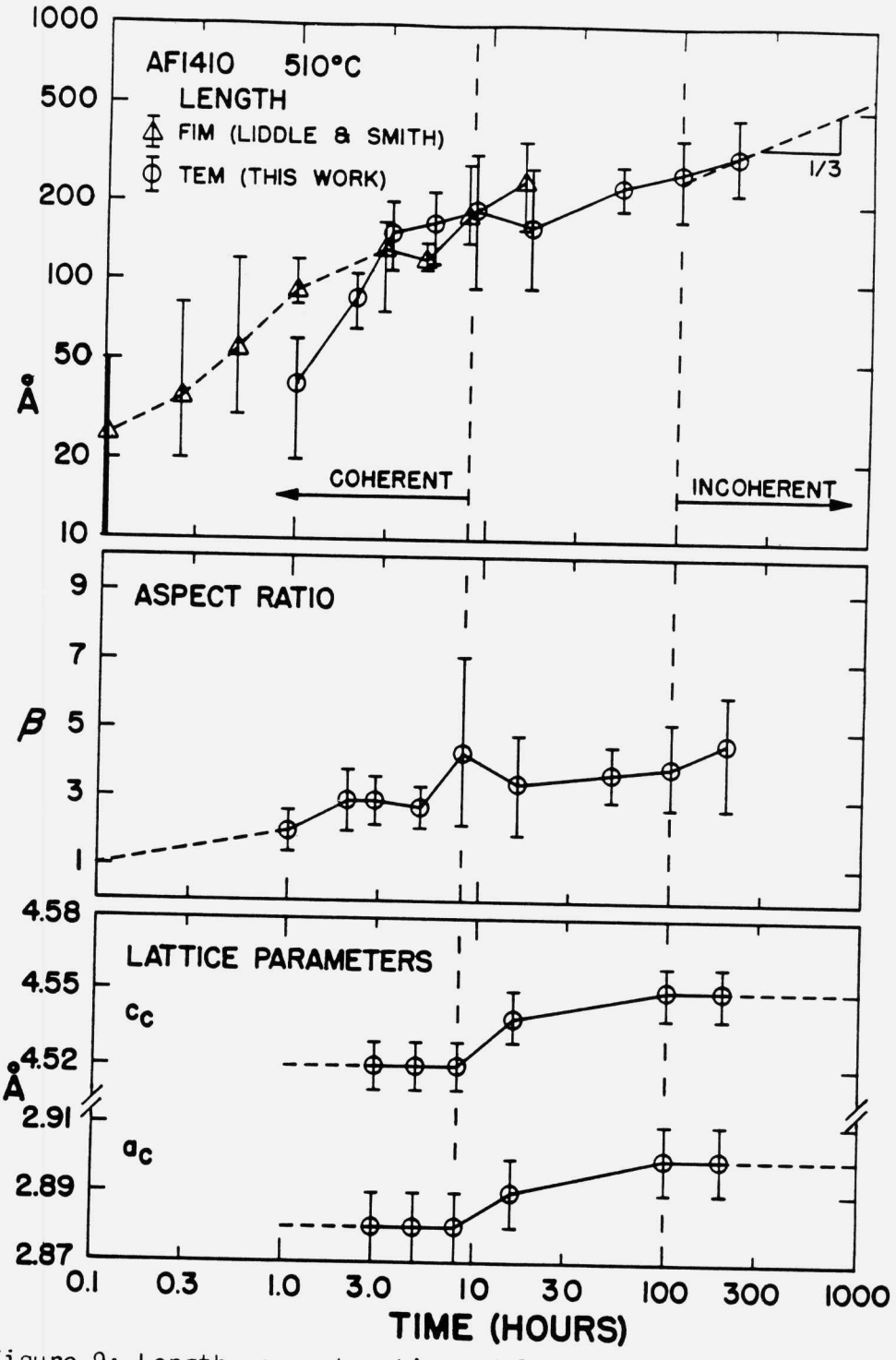

Figure 9: Length, aspect ratio and lattice parameters of M_2C carbides extracted from AF1410 as a function of tempering time at 510°C.

length, aspect ratio β and lattice parameters as a function of tempering time at 510°C. From FIM observations (9), it is believed that the aspect ratio starts off at about 1, which is reasonable for a particle minimizing its interfacial area, and there seems to be an upward trend in aspect ratio. The 0.02Å shift in the a_c' lattice parameter is shown graphically at the bottom of the figure, and if we call the lower end coherent and the upper end incoherent, with some kind of transition region in between, this corresponds to a loss of coherency at a carbide length of about 200Å (top of figure).

Figure 10 is the analogous figure for the 1410-4Mo steel. Here the aspect ratio is expected to start at about 1, and, from other work (28), increases to large values at long tempering times. The generally higher aspect ratios compared to AF1410 is consistent with the larger transformation strains for the Mo_2C carbide (Table 1)--the particles are maximizing their dimension in the direction of minimum principal strain, i.e., along $[100]_f$. Compared to AF1410, the shift in the a_c' parameter (0.03Å for these carbides) is translated to shorter tempering times by a factor of about 8, and corresponds to a coherency loss at a carbide length of about 100Å. This is a factor of 2 smaller than that for AF1410, consistent with the larger principal transformation strains for this carbide.

DISCUSSION

Nucleation

At the earliest times investigated (1h), the precipitates were observed on dislocations. However, because the disloca-

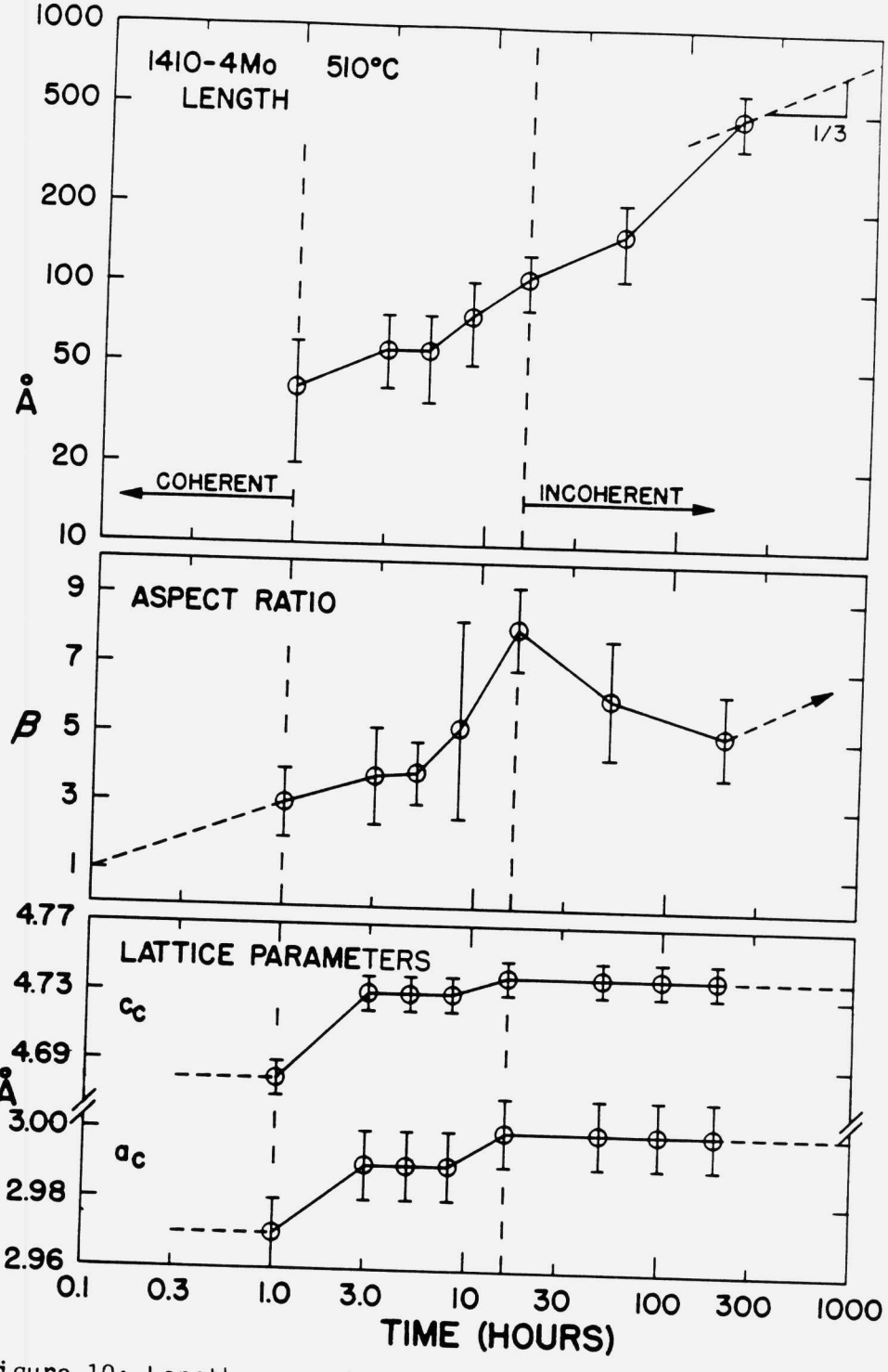

Figure 10: Length, aspect ratio and lattice parameters of M_2C carbides extracted from the 1410-4Mo steel as a function of tempering time at 510°C.

tions have some mobility at the tempering temperature (510°C), they could have moved the short distance required to associate themselves with the precipitates. This distance is given by

$$s = 1/2(1/N_V)^{1/3}, \qquad [5]$$

where N_V is the number of particles per unit volume. If we use the maximum value of N_V, found after tempering 15min by Liddle et al. (9), of $2 \times 10^{18}/cm^3$, s is about 40Å.

It is more probable that the carbides are heterogeneously nucleated on dislocations. The carbides have an average interparticle spacing given by

$$\lambda = (1/N_V)^{1/3}. \qquad [6]$$

If all the carbides are heterogeneously nucleated, the number of particles per unit dislocation line length N_L, is given by

$$N_L = N_V/L_V \qquad [7]$$

where L_V is the dislocation line length per unit volume. Letting

$$N_L = 1/\lambda \qquad [8]$$

gives the required dislocation density for this precipitate density

$$L_V = N_V^{2/3}. \qquad [9]$$

Again using $N_V = 2 \times 10^{18}/cm^3$ gives $L_V \approx 2 \times 10^{12}/cm^2$. This corresponds to a very highly cold-worked structure, and the as-quenched lath martensite matrix of AF1410 may have this kind of dislocation density.

Between the lattice parameter calculations and measurements, it is apparent that, although the carbides may nucleate heterogeneously, they nucleate coherently. Additional circumstantial evidence for this follows from the observation by Tanino et al. (23) of double lobe contrast (indicating a coherent precipitate) from Mo_2C carbides in what Davenport (24) claims to be a predominantly δ-ferritic steel. Davenport did not observe double lobe contrast from Mo_2C carbides in his martensitic 0.22C-3.45Mo steel, and concluded from this that they are not coherent. However, because the strain field of the dislocations probably overlap with that of the precipitate, double-lobe contrast may not be observable for a coherent precipitate in this case. Because of the interaction energy between the strain fields of the carbide and dislocation, it seems even more likely that carbides in a matrix with a high dislocation density (martensitic) would be coherent, compared to the same carbides in δ-ferrite. Coherent carbides will have a stronger interaction with the dislocations.

We know from Tanino et al. (23) and Davenport (24) that

Mo_2C carbides precipitating in δ-ferrite are coherent. For steels of the carbon contents investigated, the tetragonality of the martensite is negligible, so there is no difference in the crystallography and kinematics of Mo_2C carbide precipitation between these two phases. The carbides precipitating in AF1410 are "mixed" M_2C carbides which have substantially lower transformation strains (Table 1) and so are even more likely to be coherent. Further support for coherency of the carbides is provided by the agreement between AP/FIM measurements of the carbide compositions (29) and the predictions based on coherent equilibrium (18), consistent with the magnitude of lattice parameter shift observed here.

Coherency Loss

Because of the magnitude of the transformation strains, it is expected that the carbides lose their coherency at some point within the 1-200h time frame investigated. From FIM observations, Liddle et al. (9) used an apparent change in the carbides' morphology (aspect ratio) to signify a loss of coherency. In the present work, no such abrupt change in particle morphology was observed, nor was any carbide internal faulting. The carbides generally had a wide range of aspect ratios in any particular heat treatment, and there was a general upward trend as tempering times increased. Because of the large ranges of β, and the sample size examined, any discontinuities in β in Figure 9 do not appear significant.

In this work, the time frame for coherency loss of M_2C carbides in AF1410 is most clearly expressed by lattice parameter shifts with good agreement between model calculations (Table 2) and measurements (Table 4). This occurs over

the range of 16-100h, and corresponds to a carbide length of ~200Å. Compared to the behavior of the $(Cr,Mo)_2C$ carbides in AF1410, the Mo_2C carbides in 1410-4Mo indicate an earlier coherency loss at a lenth of ~100Å consistent with a larger transformation strain. Further research will be directed at the coherency loss mechanisms in these materials.

SUMMARY

(1) M_2C alloy carbides precipitating from an iron-base matrix tend to have all positive transformation strains.

(2) Precipitation of M_2C in AF1410 and 1410-4Mo is coherent as rods with axis along the minimum principal strain direction.

(3) The change in lattice parameter ($\Delta a_c'$) indicates a coherency loss at a length of ~200Å for AF1410 carbides and ~100Å for 1410-4Mo carbides consistent with the greater transformation strains in the 1410-4Mo carbides.

(4) The sign and magnitude of $\Delta a_c'$ is consistent with the predicted effect of coherent precipitation on carbide composition.

(5) The incoherent state has a higher aspect ratio.

ACKNOWLEDGEMENTS

The authors would like to acknowledge NSF-MRL support for part of this work under the Steel Research Group program. Carpenter Technology Corporation graciously supplied the two

steels, and H.M. Lee of MIT provided some of the extraction replicas.

REFERENCES

1. G.R. Speich, D.S. Dabkowski and L.F. Porter, Met. Trans. 4 (1973) 303.

2. K. Kuo, JISI 171 (1953) 223.

3. S. Floreen and G.R. Speich, Trans. ASM 57 (1964) 714.

4. V.K. Chandhok, J.P. Hirth and E.J. Dulis, Trans. ASM 56 (1963) 677.

5. J.P. Hirth, E.J. Dulis and V.K. Chandhok in Strength of Metals and Alloys (ICSMA 6), R.C. Gifkins, ed., Pergamon Press, NY, NY (1982).

6. V.K. Chandhok, J.P. Hirth and E.J. Dulis, Trans. AIME 224 (1962) 858.

7. H.J. Goldschmidt, Interstitial Alloys Plenum Press NY, NY (1967).

8. Li Chang, G.D.W. Smith and G.B. Olson, J. de Physique Supplement to No. 3 47 (1986) 265.

9. J.A. Liddle, G.D.W. Smith and G.B. Olson, 33rd Int'l Field Emission Symposium Proceedings (1986)

10. G.B. Olson and M. Cohen, in Dislocations in Solids, F.R.N. Nabarro, ed., North-Holland, Amsterdam (1986).

11. J.S. Bowles and J.K. MacKenzie, Acta Met. 2 (1954) 129, 138, 224.

12. M.S. Wechsler et al., Trans AIME 197 (1953) 1503.

13. R Bullough and B.A. Bilby, Proc. Phys. Soc. B69 (1956) 1276.

14. K.A. Taylor, Aging Phenomena in Ferrous Martensites, Ph.D. Thesis, MIT Dept. Mat. Sci. and Eng'g. (1985).

15. K.H. Jack, JISI 169 (1951) 26.

16. S. Nagakura and S. Oketani, Trans. ISI Jap. 8 (1968) 265.

17. Powder Diffraction File, Joint Committee for Powder Diffraction Standards, Swarthmore, PA (1987).

18. M. Grujičić, these proceedings.

19. D. Raynor, J.A. Whiteman and R.W.K. Honeycombe, JISI 204 (1966) 349.

20. D. Raynor, J.A. Whiteman and R.W.K. Honeycombe, JISI 204 (1966) 1114.

21. D.J. Dyson et al., Acta Met. 14 (1966) 867.

22. W. Pitsch and A. Schrader, Arch. Eisen. 29 (1958) 715.

23. M. Tanino, T. Nishida and K. Aoki, JISI 205 (1967) 874.

24. H. Morikawa, H. Komatsu and M. Tanino, (Jap.) J. of EM 22 (1973) 99.

25. A.T. Davenport, Precipiation in Some Pure Secondary Hardening Steels, D.Phil. Thesis, University of Sheffield, Faculty of Metallurgy (1968).

26. I.M. Lifschitz and V.V. Slyozov, Phys. Chem. Solids 19 (1961) 35.

27. C. Wagner, Z. Elektrochem. 65 (1961) 581.

28. G.N. Haidemenopoulos, unpublished research (1986).

29. G.M. Carinci, unpublished research (1987).

AP/FIM STUDY OF MULTICOMPONENT M_2C PRECIPITATION

G.M. CARINCI[1], G.B. OLSON[1,3], J.A. LIDDLE[2], L. CHANG[2], G.D.W. SMITH[2]

(1) Department of Materials Science and Engineering, Massachusetts Institute of Technology, Cambridge, MA 02139; (2) Department of Metallurgy and Science of Materials, University of Oxford, Parks Road, GB-Oxford OX1 3PH, Great-Britain; (3) now with Department of Materials Science and Engineering, Northwestern University, Evanston, IL 60208.

INTRODUCTION

As the demand for ultrahigh-strength, high toughness materials increases, the value of the high performance Co-Ni secondary hardening steels has become more evident. The first of these alloys to be developed, HP 9-4-X [1], contained 9Ni, 4Co, 0.20-0.45C (wt%), and small amounts of the carbide-forming elements Cr, Mo, and V. These steels were followed by HY180 [2], which contains 10 Ni, 8 Co, 0.12 C (wt%), and small amounts of Mo and Cr. The exact role played by each of the individual alloying elements in Co-Ni steels was investigated by Speich et al. [2]. These workers attributed the excellent properties to the stability of the microstructure against dislocation

recovery. Little et al. [3] of General Dynamics also investigated steels with a range of C, Cr, Mo, and Co compositions while keeping the Ni composition constant at 10 wt%. In particular, they investigated the effects of Co at levels as high as 15.4 wt%. The outcome of this work was the development of AF1410 (Fe-14Co-10Ni-2Cr-1Mo-0.16 C - wt%), which produces an outstanding combination of strength and toughness.

Control of multicomponent carbide precipitation behavior is important to the design of higher-strength steels of this class. To elucidate the basis of the desirable precipitation behavior in AF1410, atom-probe/field-ion microscopy (AP/FIM) studies have been carried out. A preliminary investigation [4] showed that small rod-like M_2C carbide particles were present in the standard heat treated and overaged conditions. A more systematic investigation [5,6] described the evolution of the carbide particle morphology at the standard heat treatment temperature of 510^{o}C. The composition trajectory of these carbides during precipitation at the standard tempering temperature is the concern of the investigation reported here.

EXPERIMENTAL

The AF1410 used in this study was supplied by Carpenter Technology Corporation and had the composition Fe - 14.24Co - 10.21Ni - 2.10Cr - 1.03Mo - 0.163C (wt%). The as received material was first austenitized at 830^{o}C for 1.5 hours and oil quenched. Subsequent tempering treatments at 510^{o}C were carried out in a salt bath for times up to 15 minutes. Longer treatments were done in a furnace after sealing the samples under an argon atmosphere in silica tubes.

FIM and atom probe examination of AF1410 after these various tempering treatments were conducted using a Vacuum Generators FIM 100 with a 226cm curved flight tube with a Poschenrieder type energy compensator [7]. Atom probe analysis was performed at a specimen temperature of approximately 80 K and at a pressure of $2x10^{-6}$ mbar using neon imaging gas. FIM specimens were prepared by electropolishing specimen blanks (0.5mm x 0.5mm x 20mm) using a standard two stage electropolishing technique. The first stage polishing was performed at 20V using a 25% perchloric-75% acetic acid electrolyte, while the second stage polish was performed at 18V using a solution of 2% perchloric acid in 2-butoxyethanol.

RESULTS

Hardness Measurements

The hardness as a function of tempering time at 510°C (as previously reported in ref. 6) shows a rapid initial increase in hardness from 530HV to 550HV (Fig.1). This rapid increase is then followed by a slower rise to peak hardness of 574HV after 15 minutes. The hardness decreases only slightly until 5 hours, after which the hardness drops more rapidly between 5 and 16 hours.

Field-Ion Microscopy

Our previous FIM study [6] of AF1410 examined the morphology of the carbide particles in the as received condition and after tempering at 510°C for 1, 5, 15, and 30 minutes and 1, 3, 5, 8, and 16 hours (Fig.2). In these photos Mo atoms appear as bright spots while the remainder of the atoms are not readily seen. Such contrast occurs because Mo has a high evaporation field and it tends to draw the neon imaging gas from the surroundings and renders the surrounding matrix barely visible. This phenomenon is most evident in the as

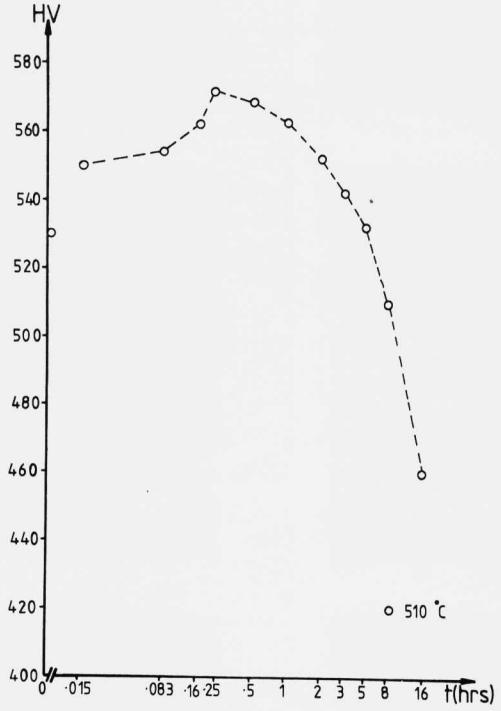

Figure 1. The hardness curve (HV) obtained by tempering AF1410 at 510° C (20kg load) [6].

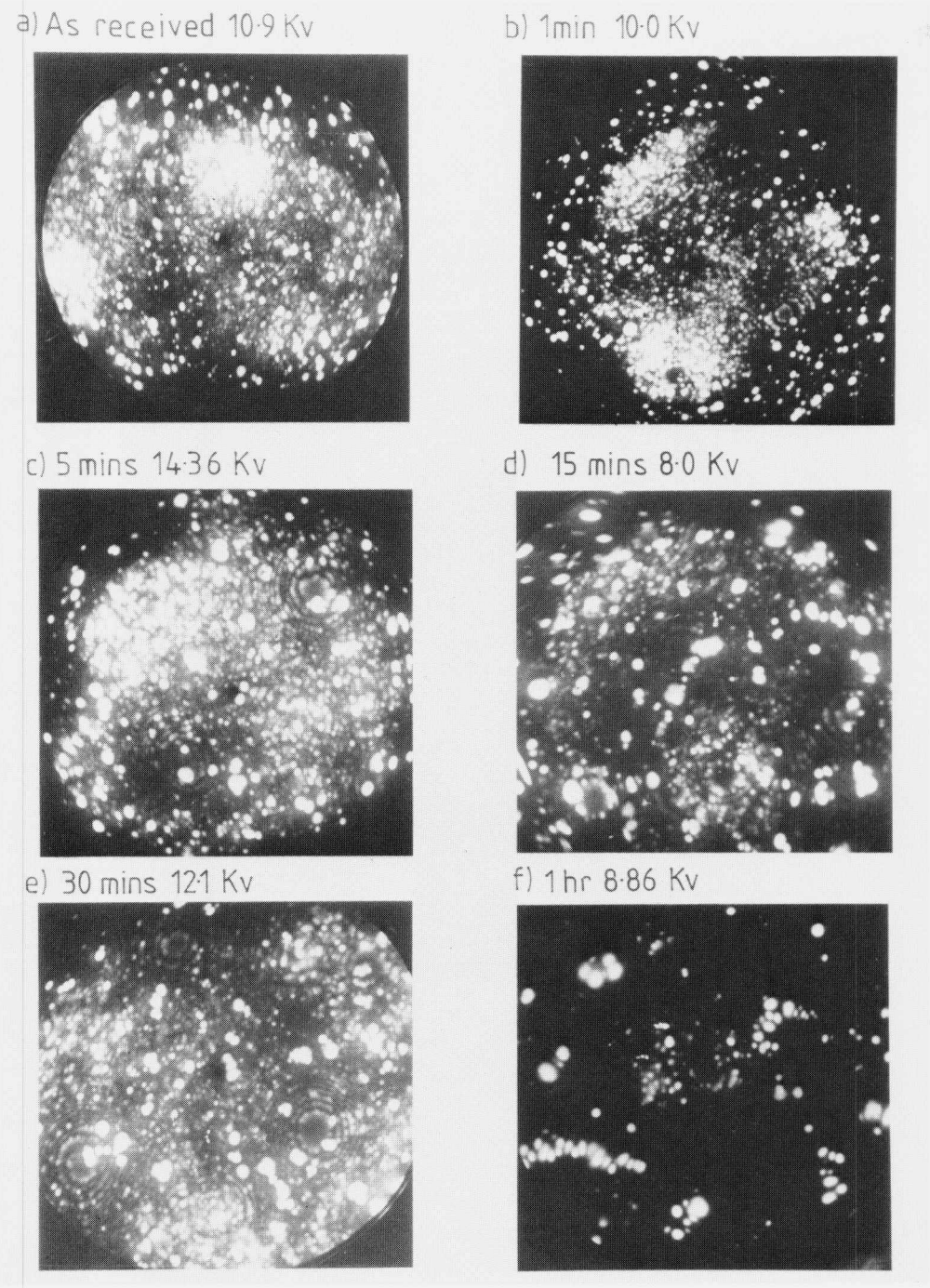

Figure 2. The development of carbide particles as a function of tempering time at 510° C. All FIM images were produced using neon image gas [6].

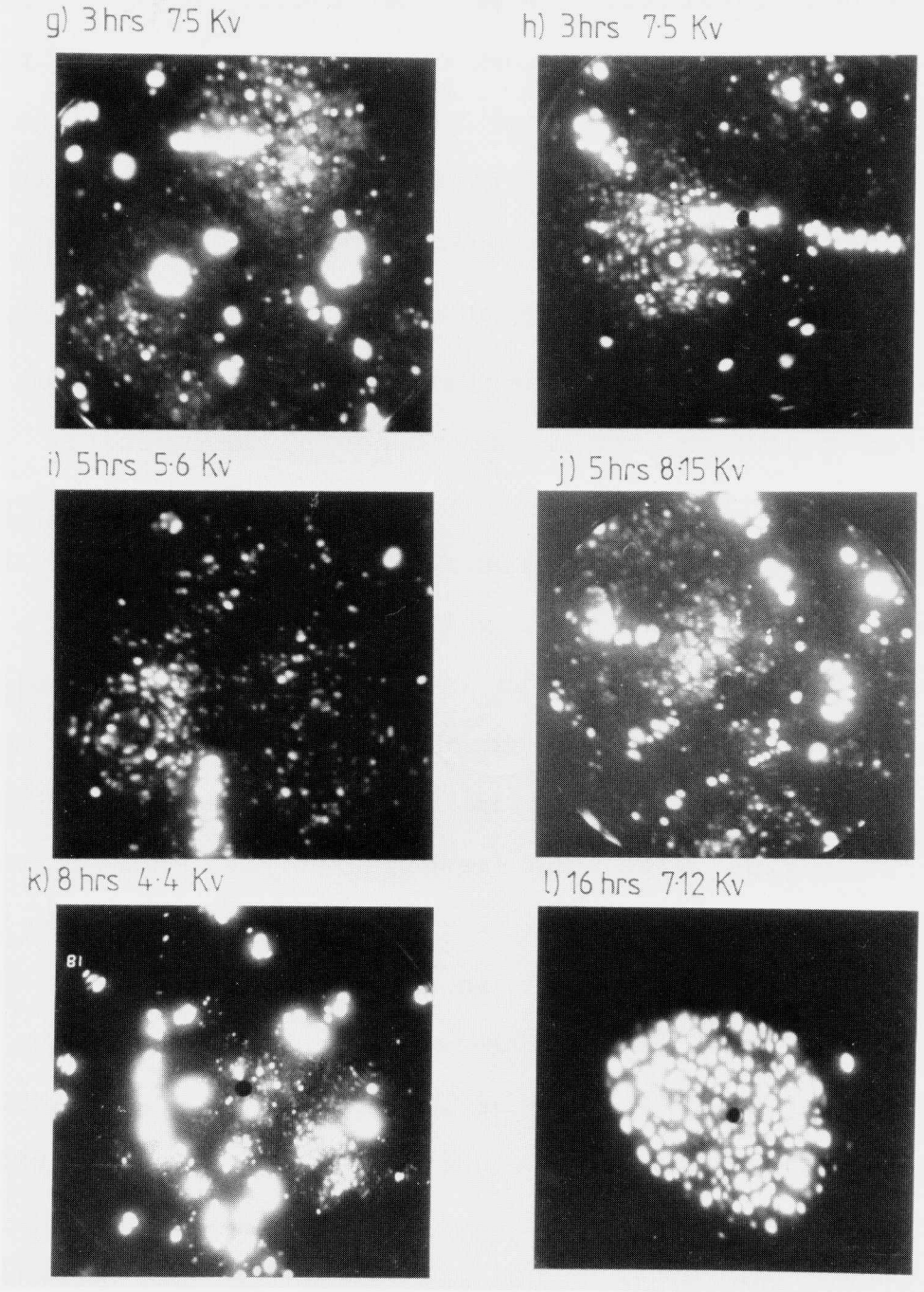

Figure 2 (cont.)

received material, where the small, bright spots correspond to the position of Mo atoms in the matrix. Small clusters of Mo atoms result after tempering for 1 and 5 minutes, while after 15 minutes much larger clusters develop. A rod-like morphology, which is expected of these secondary hardening M_2C type carbides, develops after tempering for 30 minutes. After tempering for 1 and 3 hours the carbides are larger and the rod-like morphology is clearly defined. Tempering for 5 hours (standard treatment) results in a thickening of the rods, while tempering for 8 and 16 hours caused not only an enlargement of the carbides but also a change in morphology from rods to more equiaxed structures. It is interesting to compare the morphologies with the results on hardness versus tempering time. The initial cluster formation corresponds to a rise in the hardness, while the further development of the rod-like carbides results in only a slight decrease in the hardness. Subsequently, the hardness drops much quicker after 5 hours, which corresponds to the morphology change from rods to coarser spheroids. The evolution of the particle morphology as a function of aging time is summarized in

Figure 3. Although the morphology has been well characterized, the size of these carbides is difficult to estimate from FIM observations because they protrude from the surface and are magnified more than the adjacent matrix [8]. Apparent particle size (using the largest dimension) as a function of tempering time is presented in Figure 4 [6]. Initially, the particle size remains constant, but as aging continues there is a rather smooth increase. At 5 hours a small discontinuity seems to exist. At times greater than 5 hours, the apparent size increases again with the increase in tempering time. A line of best overall fit calculated for the data for 15 minutes and onward is:

$$\ln(r) = 4.28 + 0.428 \times \ln(t)$$

where r is in Å and t is in hours.

Boundaries, such as lath boundaries, were easily recognized in samples tempered for 5 and 8 hours, since they were decorated with brightly imaging Mo atoms (Fig.5). Atom probe analysis of these boundaries indicated segregation of not only Mo but also Cr and C. Quantitative interpretation was made difficult because of boundary-matrix overlap of the probe hole. The (Fig.6)

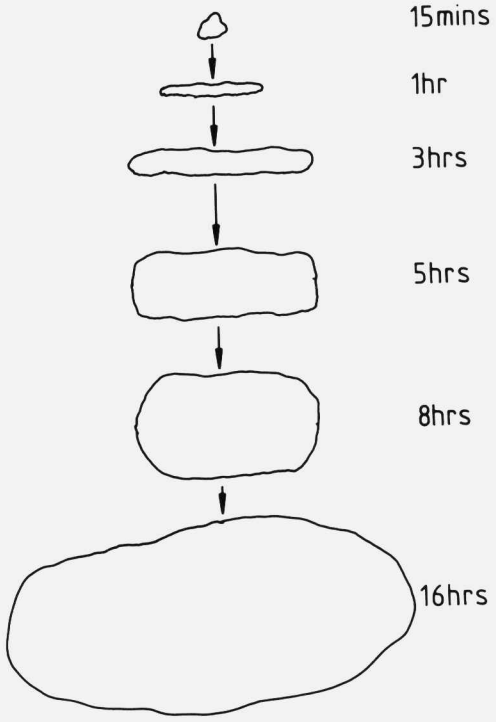

Figure 3. A schematic of the carbide-morphology development as a function of the tempering time [6].

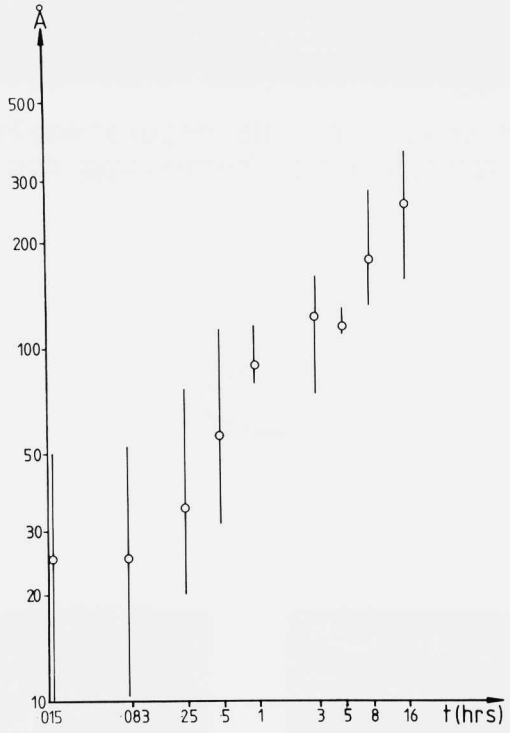

Figure 4. The apparent carbide size as a function of the tempering time [6].

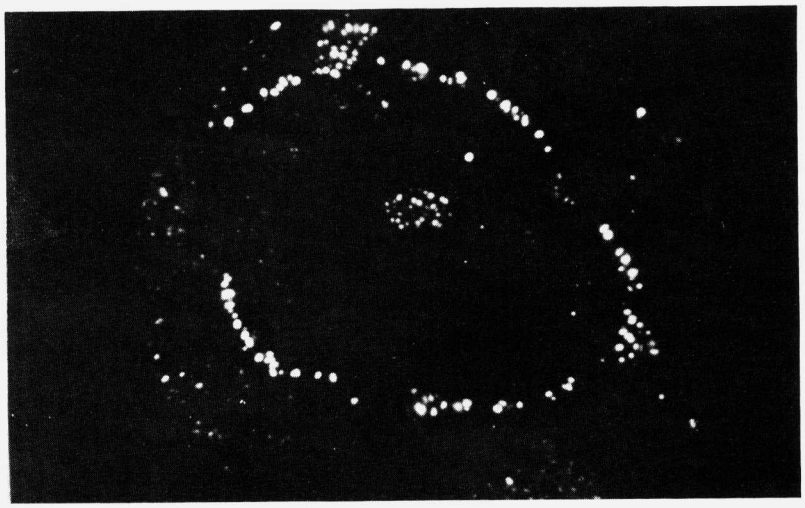

Figure 5. FIM image of a Mo decorated lath boundary in AF1410 after tempering for 8h at 510° C.

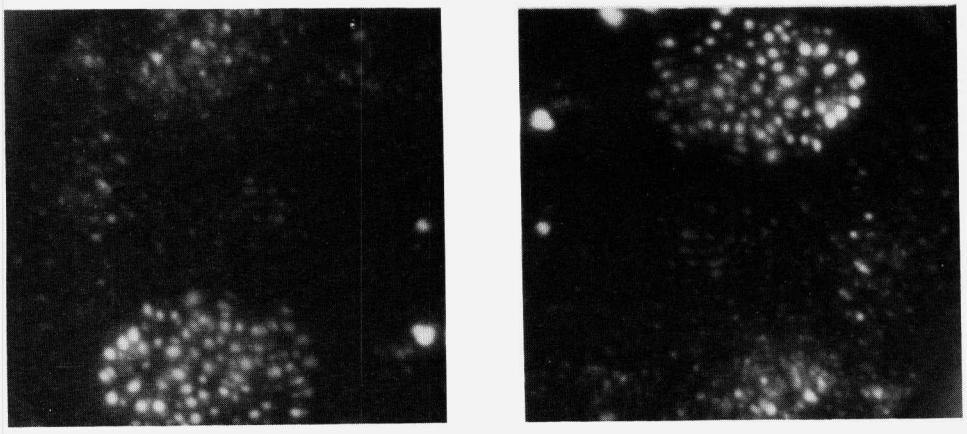

Figure 6. FIM images of anomalously large carbides in AF1410 after tempering for 8h at 510° C.

features of interest in the microstructure were occasional anomalously large carbide particles (Fig.6). Such carbides were much larger than those normally dispersed throughout the material, and were probably particles which had remained undissolved during the austenitization treatment.

Although carbide analysis was the main thrust of this work, analysis of austenite was conducted when it was observed (Fig.7). Austenite films appeared dark when imaged and possessed a significant Ni enrichment (Table 1) of approximately 30 at%.

Atom Probe Analysis of Carbides

Pulse fraction studies were performed to determine the effect of the pulse voltage on the analysis of alloying elements. The pulse fraction is the evaporation pulse voltage expressed as a fraction of the standing d.c. voltage. In general, the field dependence of the evaporation rate of the components of an alloy is strongest at the lowest sample temperatures, and under these conditions relatively low pulse fractions can be used (10-15%). At higher sample temperatures, relatively high pulse fractions must be used to suppress slow d.c. field evaporation in the

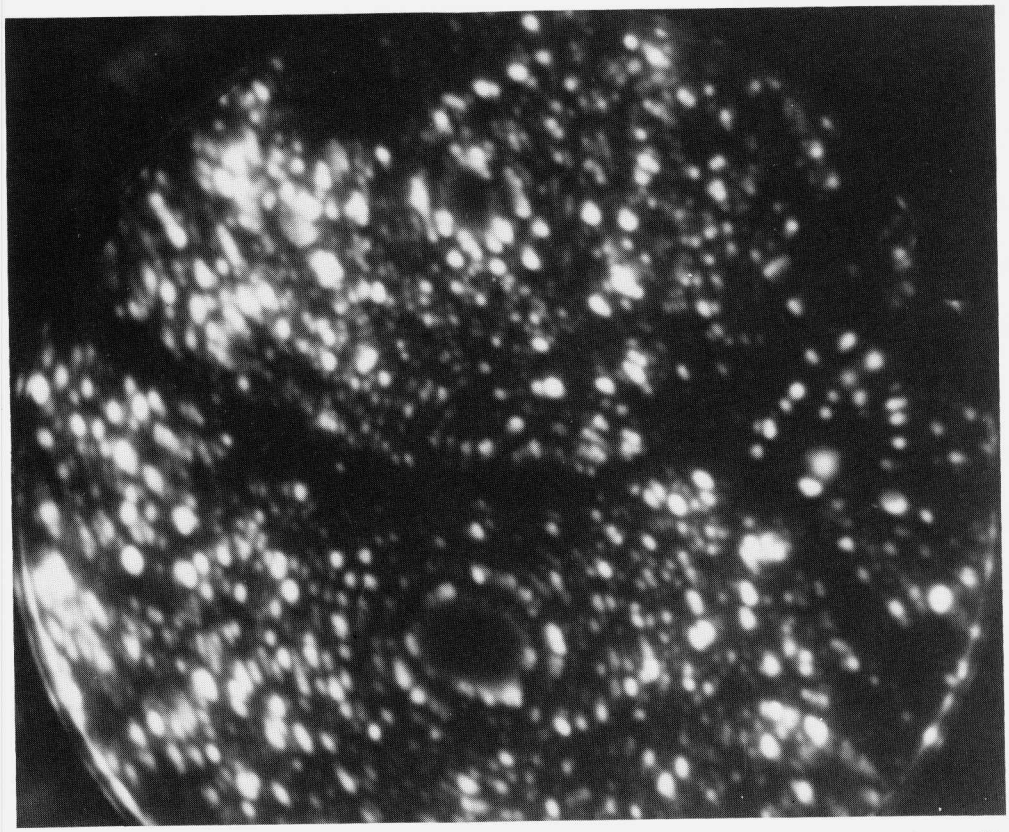

Figure 7. FIM image of an austenite film (dark band) in AF1410 after tempering for 8h at 510° C.

Table 1. Retained austenite composition in AF1410 tempered for 8 h at 510°C.

Composition (a%)	352 ions
C	1.4
Mo	1.1
Cr	3.4
Ni	28.4
Co	9.1
Fe	56.6

time intervals between successive voltage pulses. Consequently, pulse fractions as high as 0.20 were used in this analysis, since the sample temperature used (80 K) was relatively high. Operating at lower temperatures readily promoted specimen failure or 'flashing'. Concentrating the pulse fraction studies on AF1410 tempered 8 hours at 510^{o}C, the detected C composition was found to rise with the increase in pulse fraction (Table 2). The indicated error limits of these compositions are based upon ± two standard deviations of the statistical counting errors. In determining these compositions, it was assumed that the M_2C carbides would be devoid of Co and Ni. To correct for the overlap of carbide and matrix over the probe hole, the appropriate number of matrix Fe ions were subtracted from the analysis by implementing the relation [%Fe/(%Co+%Ni) = 3], based on the matrix composition separately determined by atom probe analysis (Table 3).

The reason for C loss at the lower pulse fractions is not clear, but the image gas impact on the specimen surface may transfer some momentum to the light C atoms and thereby promote activation and desorption. Also, image gas scattering of C ions could well be a

Table 2. Average chemical formula of M_2C carbides in AF1410, tempered at 510°C for 8 h, using different pulse fractions.

Pulse Fraction	Formula
0.15	$(Cr_{0.55\pm0.03}Mo_{0.38\pm0.02}Fe_{0.07\pm0.01})_2C_{0.78\pm0.02}$
0.18	$(Cr_{0.58\pm0.04}Mo_{0.36\pm0.03}Fe_{0.06\pm0.02})_2C_{0.86\pm0.04}$
0.20	$(Cr_{0.65\pm0.01}Mo_{0.30\pm0.01}Fe_{0.05\pm0.01})_2C_{0.89\pm0.01}$

Table 3. Average chemical formula for M_2C carbides in AF1410 at different times during tempering at 510°C.

Aging Time	Formula
5 h	$(Cr_{0.58\pm0.03}Mo_{0.36\pm0.03}Fe_{0.06\pm0.03})_2C_{0.81\pm0.03}$
8 h	$(Cr_{0.64\pm0.01}Mo_{0.30\pm0.01}Fe_{0.06\pm0.01})_2C_{0.89\pm0.01}$

significant factor at 10^{-6} mbar pressures. Unlike C, the apparent Mo level of the carbide was seen to decrease with increasing pulse fraction (Table 2), while the apparent Cr ion detection increased with increasing pulse fraction (Table 2). The apparent site fraction occupancy of M_2C type carbides versus pulse fraction (Fig.8) indicates that a pulse fraction of at least 0.20 is needed to correctly analyze the carbide composition. Studies using higher pulse fractions are currently in progress.

As the first step of an investigation of the carbide composition trajectory during precipitation, an in-depth study of the carbide composition has been conducted on AF1410 after tempering for 5 hours (standard treatment) and 8 hours at 510°C. After both these treatments the carbide size was quite inhomogeneous. The microstructure seemed to consist of small rod-like carbides as well as larger more-equiaxed carbides. Discrepancies in the carbide size from specimen to specimen may be the result of compositional banding, which is prevalent in many conventionally processed steels. Data were accumulated from five carbides after tempering for 5 hours, and the overall

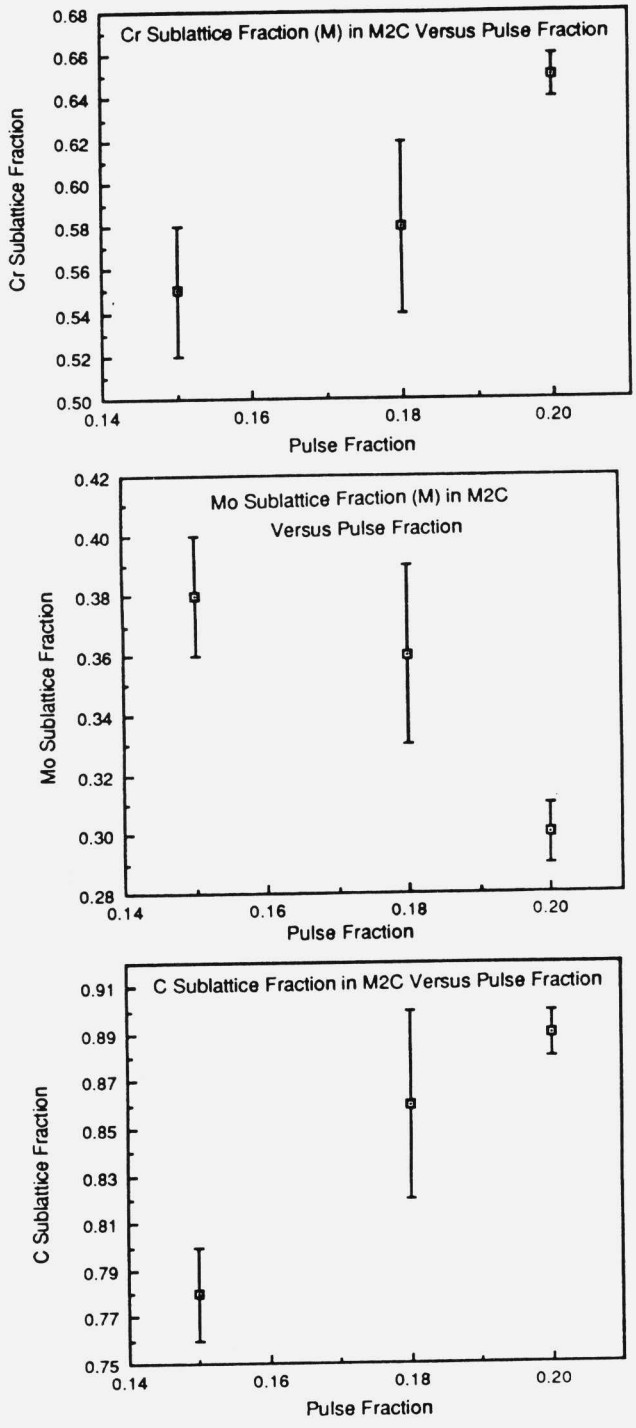

Figure 8. The (a) chromium, (b) molybdenum, and (c) carbon stoichiometry of the M_2C carbides as a function of the pulse fraction.

carbide composition was determined. Unlike the 5 hour tempered material, the 8 hour tempered material was much less prone to fracturing or 'flashing' during analysis and more samples could be successfully analyzed. Data were accumulated from eight carbides after tempering for 8hrs. and the overall composition determined (Table 4).

In addition, atom probe investigations were conducted on the matrix of these alloys. The horizontal axis of this spectrum (Fig.9) represents the mass-to-charge ratio (m/n), which is plotted in atomic mass units. The vertical axis shows the number of ions detected at any mass-to-charge ratio. In addition to the as-received material, matrix probing was conducted on material tempered for 5 and 8 hours. The analysis showed that Mo and C were very strongly partioned to the carbide phase and were only present in the matrix below the 0.1 at% level.

Ordering

In the design of AF1410, Co was added primarily to improve the dislocation recovery resistance; however, this Co addition could lead to short range ordering and be partly responsible for the high strength.

Table 4. The apparent bulk composition of the as received AF1410 [6].

Composition (a%)		3858 ions
C	0.4	
Mo	1.5	
Cr	1.6	
Ni	13.1	
Co	12.5	
Fe	70.9	

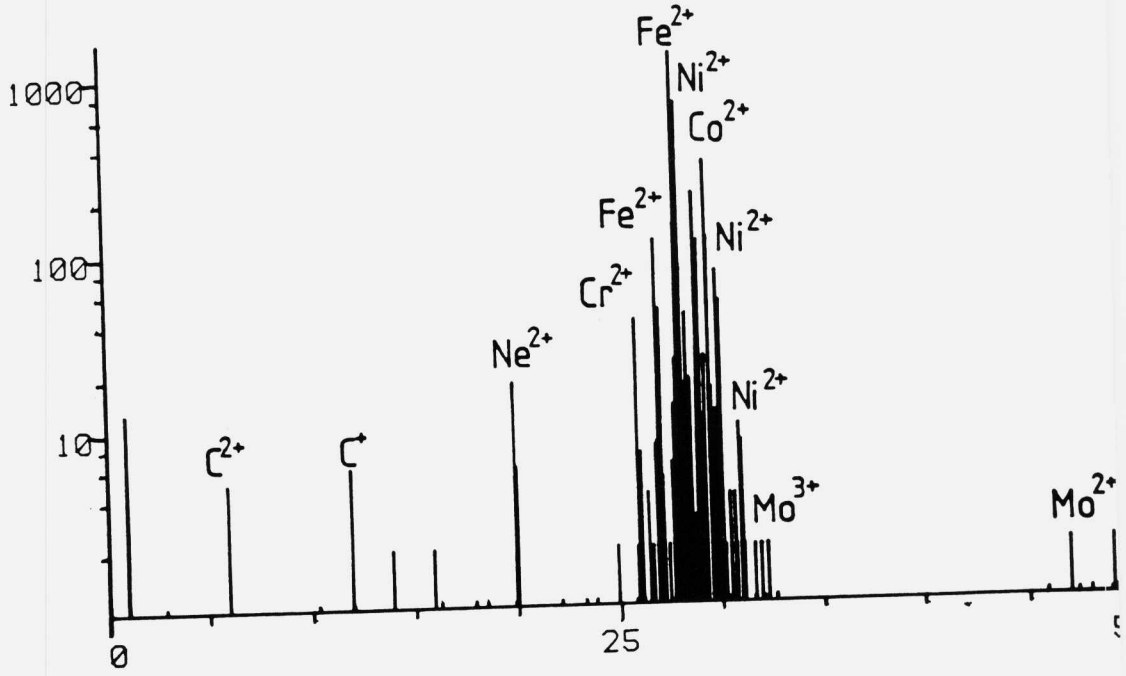

Figure 9. A high-resolution, atom-probe spectrum of AF1410 prior to tempering.

Substantial evidence exists for ordering in Fe-Ni-Co based alloys [9], and evidence of ordering has indeed been found in the matrix of AF1410. Chang et al. [5] found that 'ring doubling' (Fig.10), which is an indication of short range ordering, was evident in these alloys. Such ordering is expected since an investigation by Yedneral et al. [9] showed that ordering was enhanced by increasing the Co content up to 20%. Above this level, a large reduction in ductility and other deleterious effects on the properties result because of long range ordering. Also, it was noted in that study that ordering occurred at lower temperatures when the Ni levels were higher. However, no mention of the C content of the alloys was made in the Yedneral et al. [9] work, and further work is needed if the ordering phenomenon in these alloys is to be fully understood.

DISCUSSION

The precipitation sequence in AF1410 involves the transformation of alloy carbides from clusters to rods to spheroids and then to larger particles [6]. However, after the 5 and 8 hour tempering treatments, the

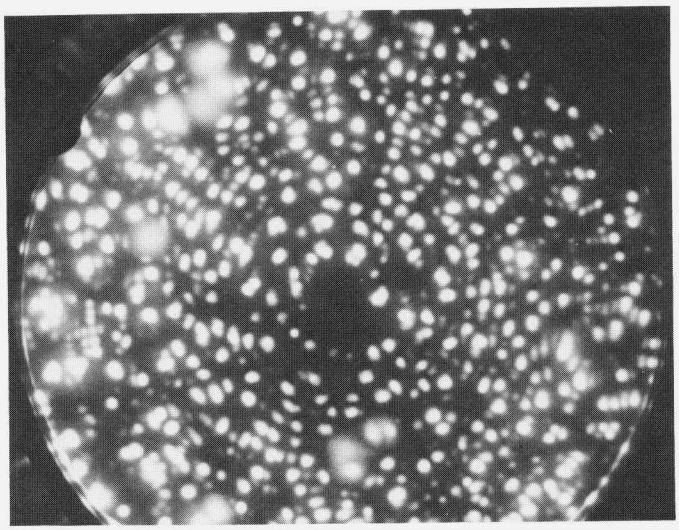

Figure 10. FIM image showing ring doubling, which is indicative of short range ordering.

present work has shown that a variation exists in the exact morphology of the particles. Not only are rod-like carbides encountered during the atom probe analysis but also larger, more equiaxed carbides are also found in addition to the occasional, undissolved carbides discussed earlier. Considering this phenomenon, the precipitate shape at equilibrium is determined by three factors, which are not independent; (a) composition, (b) surface energy, (c) strain energy [10]. There can be several reasons for such a mixture of shapes:

- the composition of the small precipitates may not be the same as for the larger ones

- the surface to volume ratio increases with decreasing size, and therefore surface energy affects the precipitate shape more at smaller sizes

- the rate of change of size of a precipitate during coarsening influences how close the precipitate is to equilibrium; the rate of

growth of the large precipitates in the distribution is small when compared with the rate of dissolution of the small ones, and so the large precipitates may be nearer to equilibrium.

Such an anomaly in the particle morphology could explain the discrepancy at 5 hours in the apparent size versus tempering time plot (Fig.4). It is interesting to compare this plot with data obtained by Davies and Ralph [10], who studied a 3.5 Mo-0.2 C steel. Such a comparison shows that the kinetics of growth and coarsening are much slower in the 3.5 Mo-0.2 C alloy. Also, the plot shows r is proportional to $t^{0.43}$ for AF1410, while for the simpler 3.5 Mo-0.2 C steel, r is proportional to $t^{0.33}$. The alloy carbide dispersion studied is much finer in AF1410, due to the higher dislocation density imparted by the Co addition. In addition to the accelerated nucleation behavior, pipe diffusion of solute atoms along dislocations may modify coarsening behavior. Consistent with the broader AP/FIM investigations of secondary hardening steels by Stiller et al. [11], secondary hardening is accelerated by the

addition of Cr, which reduces the lattice misfit between matrix and carbide and should thus lower the activation barrier for nucleation.

The experimental AP/FIM results of the carbide compositions agree rather well with the thermochemical calculations obtained by Grujicic et al. [12] using a modification of the ThermoCalc database to quantitatively treat the role of the composition-dependent lattice misfit. The calculations are based on a coherent equilibrium state, where the effect of stresses associated with the presence of coherent M_2C carbides as well of capillarity are included. Both ferrite and M_2C carbides are assumed to be compositionally homogeneous and the M_2C is taken to be spherical in shape. It is also assumed that the elastic strain energy due to coherency is a function of the composition of the M_2C-carbide phase only. Table 5 shows the results of these calculations and the expected sequence of coherent nucleation, coherent equilibrium, and final incoherent equilibrium. For comparison, the AP/FIM results are also included. For the Cr, Mo, and Fe contents, there is reasonable agreement between the calculated coherent nucleus composition and the 1 hour experimental data from the

Table 5. ThermoCalc predictions and experimental chemical formula for M_2C carbides in AF1410 after tempering at 510°C.

Description	Formula	Reference
coherent M_2C nucleation (calculated)	$(Cr_{0.49}Mo_{0.39}Fe_{0.12})_2C_{0.79}$	Grujicic et al. [12]
coherent M_2C equilibrium (calculated)	$(Cr_{0.63}Mo_{0.32}Fe_{0.05})_2C_{0.82}$	Grujicic et al. [12]
incoherent M_2C equilibrium (calculated)	$(Cr_{0.64}Mo_{0.36}Fe_{0.00})_2C_{0.99}$	Grujicic et al. [12]
AP/FIM experiment 1 h temper	$(Cr_{0.39\pm0.06}Mo_{0.47\pm0.06}Fe_{0.14\pm0.04})_2C_{0.32\pm0.05}$	Liddle et al. [6]
AP/FIM experiment 5 h temper	$(Cr_{0.58\pm0.03}Mo_{0.36\pm0.03}Fe_{0.06\pm0.03})_2C_{0.81\pm0.03}$	This Work
AP/FIM experiment 8 h temper	$(Cr_{0.64\pm0.01}Mo_{0.30\pm0.01}Fe_{0.06\pm0.01})_2C_{0.89\pm0.01}$	This Work

earlier study [6]. A significant difference exists in the C stoichiometry in this case, but this is undoubtedly due to the fact that the latter study used a high image gas pressure (10^{-5} mbar), together with a pulse fraction of 0.15, which would be too low to avoid C loss during the atom probe analysis.

The study by Speich et al.[2] demonstrated that optimum properties are achieved in this class of steel at completion of M_2C precipitation so that the transient cementite phase is fully dissolved. Hence, the standard tempering time range of 5 to 8 hours for AF1410 should represent complete M_2C precipitation. In addition, TEM study [13] indicates the carbides are fully coherent in the 5 to 8 hour temper condition, and should thus represent a state of coherent equilibrium. Observed carbide compositions at 5 and 8 hours bracket the prediction for coherent equilibrium, demonstrating excellent agreement between theory and experiment. This includes the deviation from carbide stoichiometry.

The nature of the observed changes of carbide composition with tempering time are also in excellent agreement with predictions (increasing C and Cr, decreasing Fe) although a measurement for the incoherent state is not yet available. TEM observations

[13] suggest the fully incoherent state is reached after tempering for 100 hours. The resulting carbide dispersion is then too coarse for convenient AP/FIM study. Further studies will include STEM microanalysis of the incoherent state and further AP/FIM investigation of earlier stages of coherent precipitation to more precisely define the complete carbide composition trajectory.

Conclusions

Pulse-fraction studies indicate that reliable AP/FIM microanalysis of M_2C carbides in AF1410 steel can be achieved using a 0.20 pulse fraction at 80 K. Lower pulse fractions give reduced apparent C and Cr contents. Observed $(Cr,Mo,Fe)_2C_x$ compositions in AF1410 tempered at 510^0C for 5 to 8 hours are in excellent agreement with theoretical predictions for coherent equilibrium. The observed direction of carbide composition change during precipitation is also in good agreement with prediction.

REFERENCES

1. A. Magnee, J.M. Drapier, J. Dumont, D. Coutsouradis, and L.H. Habraken, Cobalt Containing Alloys, Centre d'Information du Cobalt, Brussels (1974)

2. G.R. Speich, D.S. Dabkowski and L.F. Porter, Met. Trans. 4 (1973) 303

3. C.D. Little and P.M. Machmeier, General Dynamics, Development of a Weldable High Strength Steel, Report No. AFML-TR-75-148

4. L. Chang, G.D.W. Smith and G.B. Olson, J. De Physique, supplement au no.3, Tome 47, mars 1986

5. J.A. Liddle, G.D.W. Smith and G.B. Olson, J. De Physique, supplement au no.11, Tome 47, novembre 1986

6. J.A. Liddle, Part II Thesis, Oxford (1986)

7. A. Cerezo, G.D.W. Smith and A.R. Waugh, J. De Physique, Supplement to No.12, 45, (1984) 329

8. D.J. Rose, J. Appl. Phys. 27 (1956) 215

9. A.F. Yedneral, O.P. Zhukov, M.A. Kablukovskaya, B.M. Mogutnov and M.D. Perkas, Fiz. Metal. Metalloved. 36 No.4 (1974) 727

10. D.M. Davies and B. Ralph, J. Iron and Steel Inst. 210 (1972) 262

11. K. Stiller, L-E. Svensson, P.R. Howell, Wang Rong, H-O. Andren and G.L. Dunlop, Acta Met., 32 (1984) 1457

12. M. Grujicic and G.B. Olson, these proceedings

13. J.S. Montgomery and G.B. Olson, these proceedings

SOLID STATE PRECIPITATION AT HIGH SUPERSATURATIONS

RICHARD WAGNER AND REINHARD KAMPMANN
Institut für Werkstofforschung, GKSS Forschungszentrum
Geesthacht GmbH, D 2054 Geesthacht, F.R. Germany

INTRODUCTION

In this paper, it is intended

i) to discuss a kinetic model which allows us to predict the evolution of the precipitate radii and their number density with aging time (t) at a given aging temperature T.

ii) The precipitation kinetics predicted by this model will be compared with experimental kinetic data from isothermally aged Cu-1.9 at%Ti and Fe-1.38 at%Cu before we

iii) address ourselves to some still open questions with respect to the kinetics and morphologies, particularly in heavily supersaturated alloys.

Let us consider a binary alloy composed of A (solvent) and B (solute) atoms and a phase diagram which is schematically shown in Fig. 1.

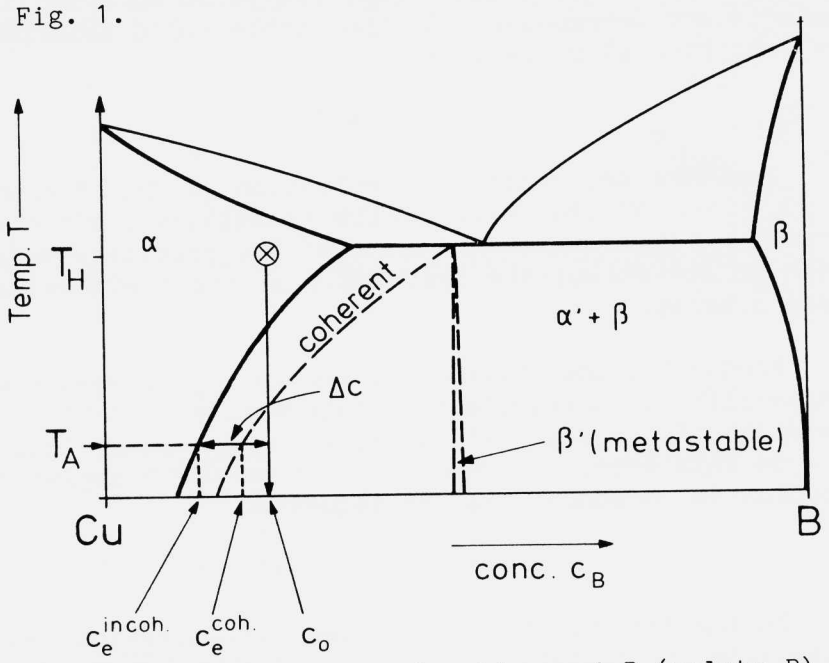

Fig. 1: Schematic phase diagram for binary A-B (solute B) alloys. The dashed lines show the phase fields for metastable (coherent) phases. T_A: aging temperature; T_H: homogenization temperature.

In order to initiate a precipitation reaction, the Cu-alloy with a solute concentration c_0 is first homogenized in the single-phase region at T_H and then a) either cooled down slowly into the two-phase region or b) quenched into brine prior to isothermal aging at a temperature T within the two-phase region (fig. 1). In both cases, thermodynamic equilibrium is reached if the supersaturation Δc, defined as

$$\Delta c = \frac{c_0 - c_e(T)}{c_e(T)} \qquad (1.1)$$

becomes zero.

Procedure b) which is frequently used for studies of decomposition kinetics under conditions which can be somewhat better controlled and theoretically handled ($T = T_A$ = const.; diffusion constant $D \approx$ const.) than for case a), leads to precipitate microstructures the volume fraction and particle dispersion of which depends on $\Delta c(T)$ and the aging time t (this case will be treated in more detail in sections 2 and 3).

Within the miscibility gap, the solid solution α becomes unstable and decomposes into the stable solid solution α' and the precipitated phase β, i.e.

$$\alpha \rightarrow \alpha' + \beta \qquad (1.2)$$

The terminal solute concentration of the A-rich matrix α' is given by the equilibrium solubility limit $c_e(T)$; the terminal solute concentration c_p of the precipitated phase is given by the solubility limit at T at the B-rich side of the phase diagram.

Frequently the interfacial energy $\sigma_{\alpha\beta}$ between the matrix and equilibrium precipitate is rather large, in particular if the width of the miscibility gap is rather large (see section 3) . In this case, the decomposition of the homogeneous solid solution (α) proceeds via the sequence.

$$\alpha \rightarrow \alpha'' + \beta' \rightarrow \alpha' + \beta \qquad (1.3)$$

During the first step of the precipitation sequence a <u>metastable</u> precipitate (β') is formed with (frequently) large associated coherency strains and a small interfacial energy $\sigma_{\alpha\beta}$. Often the metastable phase β' is an intermetallic compound. Because of the large coherency strains, the metastable ('coherent') solvus line (dashed line in fig. 1) is shifted